UTS UNIVERSITY OF TECHNOLOGY SYDNEY

UCNP-based Sandwich Immunoassay for Protein Detection

by Ziwei Wu

Thesis submitted in fulfilment of the requirements for the degree of

Doctor of Philosophy

under the supervision of Prof. Jiajia Zhou, Prof. Dayong Jin

University of Technology Sydney
Faculty of Science

21/07/2025

Certificate Of Original Authorship

I, Ziwei Wu, declare that this thesis is submitted in fulfilment of the requirements for the award of Doctor of Philosophy in the School of Mathematical and Physical Sciences, Faculty of Science, at the University of Technology Sydney.

This thesis is wholly my own work unless otherwise referenced or acknowledged. In addition, I certify that all information sources and literature used are indicated in the thesis.

This document has not been submitted for qualifications at any other academic institution.

This research was supported by the Australian Government Research Training Program (RTP) Scholarship doi.org/10.82133/C42F-K220.

Signature: Production Note:
Signature removed prior to publication.

Date: 21/07/2025

Acknowledgements

First and foremost, I would like to express my sincere appreciation to my supervisors, Professor Jiajia Zhou and Professor Dayong Jin, for their invaluable guidance and support throughout my PhD journey. Their mentorship has greatly influenced the way I approach research, encouraging me to think more strategically and work more efficiently. I am deeply grateful for their insightful advice, expertise, and continuous encouragement, all of which have played a vital role in shaping the direction and progress of my work.

I would also like to acknowledge my colleagues and collaborators who contributed to my research. I am especially grateful to my IBMD colleagues, Dr. Guochen Bao and Dr. Jiayan Liao, for teaching me experimental skills when I joined the lab at start. I also thank Dr. Mahnaz Maddahfar for providing the polymers that supported all my projects, Ms. Yitong Zhao for assisting with the strip tests and optical system setup, and Dr. Yangjian Cai for his guidance in nanoparticle synthesis. Special thanks to Dr. Brad Walsh from IProteome Pty Ltd for his valuable advice and support throughout the project.

I would like to extend my heartfelt thanks to all my colleagues, Mr. Maoxin Zhang, Ms. Dan Li, Ms. Fei Su, Ms Dan Shao, Dr. Zhichao Yang, Mr. Ming Lu, Mr. Sitong Wu, Mr. Zelv Chen, Mrs. Mengyuan Yi. Our shared meals and chats brought a lot of fun and comfort during this journey.

I would like to express my deepest gratitude to my friends and parents. Whenever I faced difficulties or setbacks, they were always the first to comfort and support me.

Finally, I would like to acknowledge UTS, Australian Research Council and Centre of Excellence on Quantum Biotechnology for their generous support through tuition funding, scholarships, and research expenses.

List of Publications

[1] Ziwei Wu, Yitong Zhao, Mahnaz Maddahfar, Tesfaye Asrat, Bradley J Walsh, Dayong Jin, Jiajia Zhou*, “Upconversion lateral flow test for A1 beta-casein proteins in milk and infant formulas”, *Not submitted*

[2] Ziwei Wu, Yangjian Cai, Yitong Zhao, Mahnaz Maddahfar, Martin Sadraeian, Dayong Jin, Jiajia Zhou*, “Beads-on-a-Tip testing for ultrasensitive antigen detection across a large dynamic range”, ***Smart Molecules***, published

Structure of Thesis

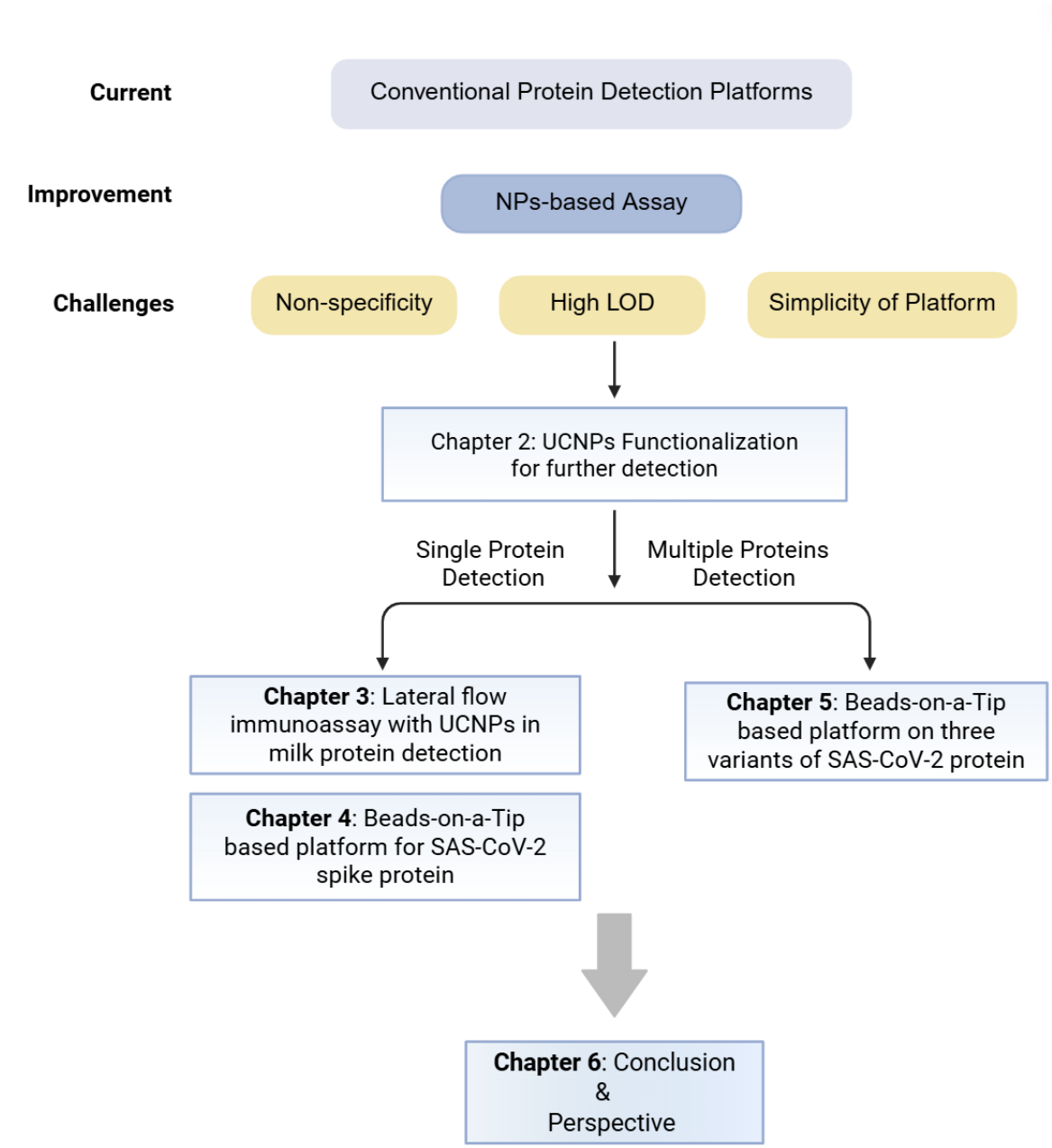

This flow chart outlines the structure of the thesis, aimed at addressing the limitations of conventional detection platforms. It highlights NP-based assays as an improvement and identifies key challenges. Chapter 2 focuses on the surface functionalization of upconversion nanoparticles (UCNPs) to improve assay performance. Chapters 3 to 5 focus on addressing these challenges by applying functionalized UCNPs across different diagnostic platforms, including lateral flow assays, Beads-on-a-Tip formats for both single and multiple protein detection. Finally, the thesis concludes with overall findings and future perspectives in Chapter 6.

Table of Contents

Abstract

Proteins serve as vital biomarkers across a wide range of applications, including cancer diagnostics, treatment monitoring, infectious disease surveillance, and food quality control. Sensitive and specific detection of low-abundance proteins, especially in early-stage disease or complex matrices, is critical not only for clinical decision-making and public health protection, but also for ensuring food safety and enabling large-scale biosurveillance. However, conventional detection methods such as enzyme-linked immunosorbent assay (ELISA) and polymerase chain reaction (PCR) are often constrained by limited sensitivity, lengthy protocols, and reliance on bulky laboratory instrumentation, making them unsuitable for rapid and decentralized testing.

To address these challenges, this thesis presents two point-of-care testing (POCT) platforms based on a sandwich immunoassay format employing upconversion nanoparticles (UCNPs) as optical reporters. UCNPs offer several advantages, including minimized autofluorescence, low background noise, and exceptional photostability, which enable high sensitivity for detecting trace levels of protein biomarkers. As a foundational step, we functionalized the UCNPs to make them water-dispersible and enable covalent antibody conjugation, ensuring their compatibility with immunoassay systems. As a foundational step, we functionalized the UCNPs with the innovated polymer to make them water-dispersible and amenable to covalent antibody conjugation, ensuring their compatibility with aqueous immunoassay systems. We first developed a lateral flow immunoassay (LFIA) employing polyclonal–polyclonal antibody pairs for the rapid and quantitative detection of A1 β-casein in milk and infant formula, using a portable reader. This platform demonstrates strong industrial potential for quality control in the dairy industry, and its sensitivity was validated against LC-MS analysis. Then, we extended the assay's applicability to a Beads-on-a-Tip platform that integrates magnetic beads (MBs)-based sandwich immunoassay with UCNPs as luminescent reporters for detecting the SARS-CoV-2 spike (S) protein. The immunocomplexes were formed in a microcentrifuge tube, enabling active washing to effectively remove unbound and non-specifically bound components, enabling active washing to effectively remove unbound and non-specifically bound components. Subsequent localized enrichment within the tip facilitates signal amplification and significantly improves detection sensitivity. Furthermore, to validate the practical

applicability of the Beads-on-a-Tip platform for multiplexing detection, we demonstrated a strategy employing spectrally distinct UCNP dopants, enabling the simultaneous quantification of multiple analytes within a single assay. These capabilities significantly expand the utility of the platforms for comprehensive biomarker analysis in both clinical diagnostics and food safety applications.

Key Words: point-of-care, upconversion nanoparticle, lateral flow immunoassay, magnetic beads, Beads-on-a-Tip, multiplexing

Chapter 1. Introduction

1.1 The Significance of Protein detection

Proteins are essential macromolecules that perform a vast array of functions in biological systems. As structural support, enzymes, transporters, and signalling molecules, proteins play a central role in maintaining cellular function and organismal health[1,2]. Their expression levels and structural modifications often reflect physiological or pathological changes, making them valuable biomarkers in numerous scientific research, clinical diagnostics and industrial applications[3,4].

Protein detection serves as a fundamental analytical tool for monitoring physiological states, diagnosing pathological conditions, verifying food safety standards, and evaluating environmental quality. Highly Sensitive and specific detection methods enable early intervention, quality control, and informed decision-making across a wide range of applications (As shown in Figure 1), including:

1.1.1 Biomedical Science

Protein biomarkers play a pivotal role in disease diagnosis, enabling the detection of infections[5], cancer[6], and metabolic disorders[7]. Biomarkers are not only used to determine the type of disease, in fact, once a diagnosis is established, biomarkers can provide valuable insights into the potential progression of the disease, including the likelihood of recurrence and expected treatment outcomes. In addition, protein biomarkers facilitate drug development, enabling the evaluation of therapeutic efficacy, toxicity, and target engagement in preclinical and clinical studies. During anticancer drug development, biomarkers are used as discovery tools in compound selection, as pharmacodynamic markers of drug mechanism or efficacy in early-phase trials, or as predictive indices of patient response in late-phase trials[8].

1.1.2 Food Industry

Protein detection in the food industry is critical for identifying harmful proteins, including allergens[9], toxins[10], and foodborne pathogens[11]. Allergenic proteins, such as those from nuts, milk, or shellfish, can trigger severe reactions in sensitive individuals even at low levels. Concurrently, monitoring protein-based toxins and pathogenic proteins is essential to prevent foodborne illnesses. Rigorous protein detection

ensures compliance with food safety regulations, minimizes public health risks, and maintains quality control throughout the supply chain.

1.1.3 Agriculture

In agriculture, protein detection supports both crop health management and livestock farming. Specific protein-based biomarkers can indicate various physiological states, such as stress responses triggered by drought, pests, or environmental toxins, as well as nutrient deficiencies like nitrogen or phosphorus shortage[12,13]. Similarly, in livestock farming, monitoring protein expression in animals provides crucial insights into their health status and metabolic conditions[14] because it could be influenced by the environment, climate change and transportation stress[15]. Furthermore, protein markers can be used to monitor growth performance and reproductive health, optimizing feeding strategies and breeding programs for better productivity and sustainability.

1.1.4 Environmental Science

Environmental monitoring frequently involves identifying proteins of microbial or biochemical origin to evaluate water quality[16] or conduct soil and sediment analysis[17]. Protein detection in these settings helps assess ecosystem health, detect pollution, and guide environmental protection measures. For example, certain microbial proteins can serve as biomarkers for contamination by heavy metals or organic pollutants, while enzymatic activity in soil samples can indicate microbial biodiversity and soil fertility[18]. By tracking these protein indicators, researchers can monitor changes in environmental conditions and support informed conservation and remediation efforts.

Across these fields, protein detection represents an indispensable approach for diagnostics, monitoring, and quality assurance. Advances in detection technologies can significantly enhance sensitivity, specificity, and usability. These innovations enable broader, more precise, and impactful applications in healthcare, agriculture, food safety, and environmental monitoring.

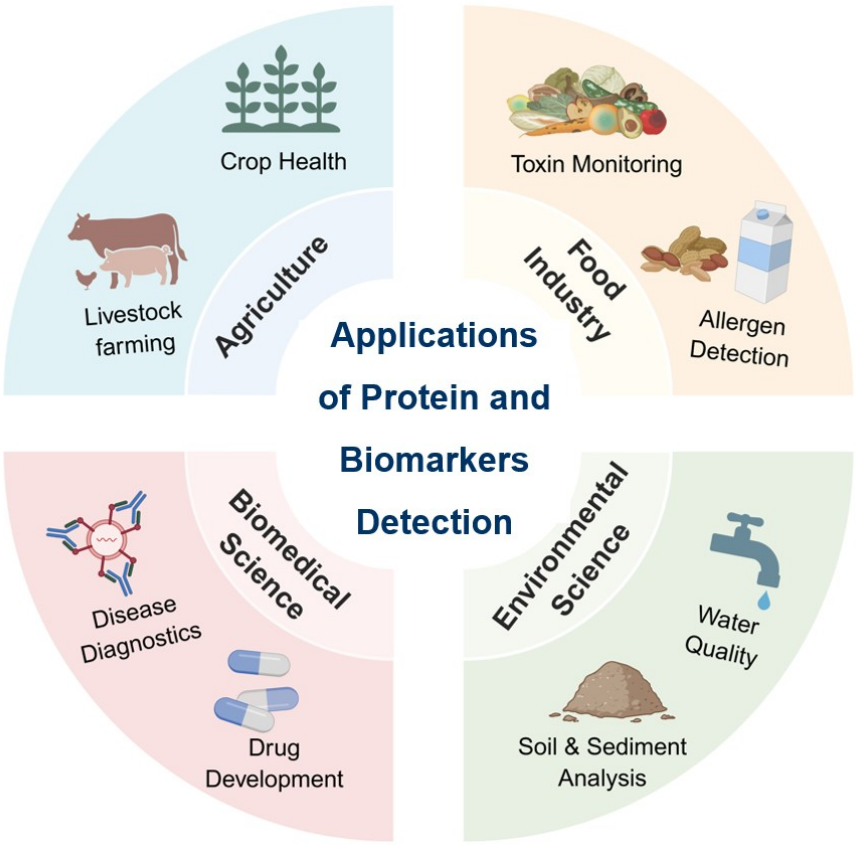

Figure 1. Representative application fields of protein and biomarkers detection across multiple sectors

1.2 The Traditional protein detection methods

The detection and quantification of proteins are fundamental to biological and biomedical research, clinical diagnostics, and industrial applications. Traditional protein detection methods encompass a broad range of biochemical, immunological, and electrophoretic techniques developed to characterize protein presence, abundance, size, and structure. While more advanced and miniaturized techniques have emerged in recent decades, these classical approaches remain foundational, serving as the basis for many modern analytical platforms (Table 1). It should be noted that many traditional protein analysis techniques rely on a combination of molecular recognition or physical separation, together with downstream signal transduction and detection modules (e.g., absorbance, fluorescence, or mass spectrometry) for quantitative readout.

Table 1. Overview of the traditional protein detection methods

Category	Method	Principle
Colorimetric	Bradford	Protein-reagent interactions that induce measurable color changes for concentration estimation via absorbance
	BCA	
	Lowry	
	Coomassie Blue (CB) G-250 dye-binding	
Densitometry	SDS-PAGE	Optical density measurement of protein bands following electrophoretic separation and staining or immunodetection.
	Western blot	
Immunoassay	ELISA	Specific antigen–antibody recognition with protein quantification achieved through enzyme-catalyzed optical signal readout (e.g., absorbance or chemiluminescence)
Mass Spectrometry	LC-MS/MS	Ionize protein or peptide fragments and measures their mass-to-charge ratio
Chromatographic	HPLC	Protein separation based on differential interactions with stationary and mobile phases, with detection enabled by coupled detectors such as UV absorbance or mass spectrometry.

1.2.1 Colorimetric analysis

One of the earliest and most widely used methods is colorimetric protein quantification, including the Bradford, Bicinchoninic Acid (BCA), and Lowry assay.[19] These methods rely on the colour change of specific reagents upon binding to protein molecules. These assays are relatively simple, inexpensive, and compatible with microplate readers, making them ideal for total protein estimation in purified samples or cell lysates. However, they are generally non-specific and are susceptible to interference from detergents and buffer components. Besides, it needs additional sample

pretreatment steps to minimize the impact of interfering substances before performing the measurement.[20]

1.2.2 Densitometry analysis

Densitometry is a quantitative analysis method that measures the optical density (intensity) of bands or spots on electrophoretic gels or membranes. Sodium dodecyl sulfate–polyacrylamide gel electrophoresis (SDS-PAGE) is a basic tool for separating proteins based on molecular weight. When combined with Western blotting, it enables both separation and specific detection of target proteins using antibodies.[21,22] In Western blotting, proteins separated by SDS-PAGE are transferred to a membrane and probed with a primary antibody specific to the target protein, followed by a labeled secondary antibody for visualization. This technique provides qualitative and semi-quantitative data, and it is invaluable for assessing protein size and expression levels in complex mixtures. However, western blotting is time-consuming, semi-quantitative at best, and dependent on antibody specificity.

1.2.3 Immunoassay

A major category of traditional method is immunoassays, and enzyme-linked immunosorbent assay (ELISA) has become the most prominent example. ELISA can be categorized by direct, indirect, or sandwich formats, depending on the target and antibody availability.[23] In particular, the sandwich ELISA offers high specificity and sensitivity and has become a gold standard for protein detection in some research and clinical diagnostics. The assay typically employs two antibodies, one for capturing the target protein and the other is detection antibody, which often linked to enzymes such as horseradish peroxidase (HRP). The enzyme catalyzes a reaction that generates a detectable signal, which is usually colorimetric or chemiluminescent.[24] Despite its advantages, ELISA requires well-characterized antibodies and often involves multiple washing and incubation steps.

1.2.4 Mass spectrometry

Mass spectrometry is a highly sensitive and specific analytical technique used for protein identification, quantification, and characterization. In proteomic applications, it often involves LC-MS/MS, where liquid chromatography (LC) separates the peptides, and tandem mass spectrometry (MS) analyses their mass-to-charge ratios.[25, 26] This method enables the detection of proteins in complex mixtures, identification of post-

translational modifications, and comparative quantification of protein abundance across samples. While it offers high-throughput and label-free analysis, the technique can be limited by its high cost, need for skilled operation, and susceptibility to sample complexity and ion suppression effects, which may impact reproducibility and quantitative accuracy in some settings.

1.2.5 Chromatographic analysis

High-Performance Liquid Chromatography (HPLC) is an analytical technique for separating, identifying, and quantifying components in complex mixtures, including proteins and peptides[27]. It operates by passing a liquid sample through a column packed with a stationary phase under high pressure, where analytes are separated based on their differential interactions with the stationary and mobile phases. HPLC is valued for its high resolution, reproducibility, and compatibility with a wide range of detection systems, most commonly UV absorbance and mass spectrometry. However, it often requires extensive sample preparation and careful method optimization, and it may exhibit limited sensitivity for low-abundance proteins without prior enrichment or coupling to highly sensitive detectors. Importantly, HPLC itself serves primarily as a separation technique, while protein detection and quantification are achieved through the integration of appropriate downstream detectors.

Traditional methods for protein analysis have provided a reliable foundation, offering performance in sensitivity, specificity, and throughput. However, each technique has inherent limitations, particularly in handling complex biological samples and in operational requirements. However, each technique has inherent limitations, particularly in handling complex biological samples and in operational requirements, as they often demand fully equipped facilities, lengthy protocols, skilled personnel, and costly instruments, despite these methods remain indispensable in laboratory settings and serve as benchmarks for new technologies. These limitations show the significant challenges when timely decision-making is required, such as isolated areas, settings with limited infrastructure or infectious disease outbreaks. Consequently, there is an increasing demand for portable, rapid and user-friendly alternatives that maintain analytical reliability while enabling on-site applications. This has driven the

development and widespread adoption of point-of-care testing technologies, which bring diagnostic capabilities directly to the patient or field setting.

1.3 Point-of-care testing (POCT)

Point-of-care testing (POCT) refers to diagnostic testing performed at or near the site of patient care, enabling rapid clinical decisions without the need for centralized laboratory infrastructure.[28] It aligns with the World Health Organization's ASSURED criteria (Affordable, Sensitive, Specific, User-friendly, Rapid and robust, Equipment-free, and Deliverable to end users).[29] POCT is designed to deliver immediate results, often within minutes. This capability significantly enhances patient management, particularly in time-sensitive situations such as emergency care, infectious disease outbreaks, and rural or resource-limited environments.

POCT is applicable to a wide range of user groups, from clinical professionals in hospital, trained but non-professional healthcare workers in community or even to unskilled individuals performing self-testing at home (Figure 2). The complexity of the technology typically decreases as the range of users broadens. For example, hospital-based systems often involve sophisticated instruments and require the involvement of trained professionals, whereas self-testing kits are designed to be as simple and user-friendly as possible. This wide applicability significantly extends the scope of POCT, making it a powerful tool in medical diagnostics.

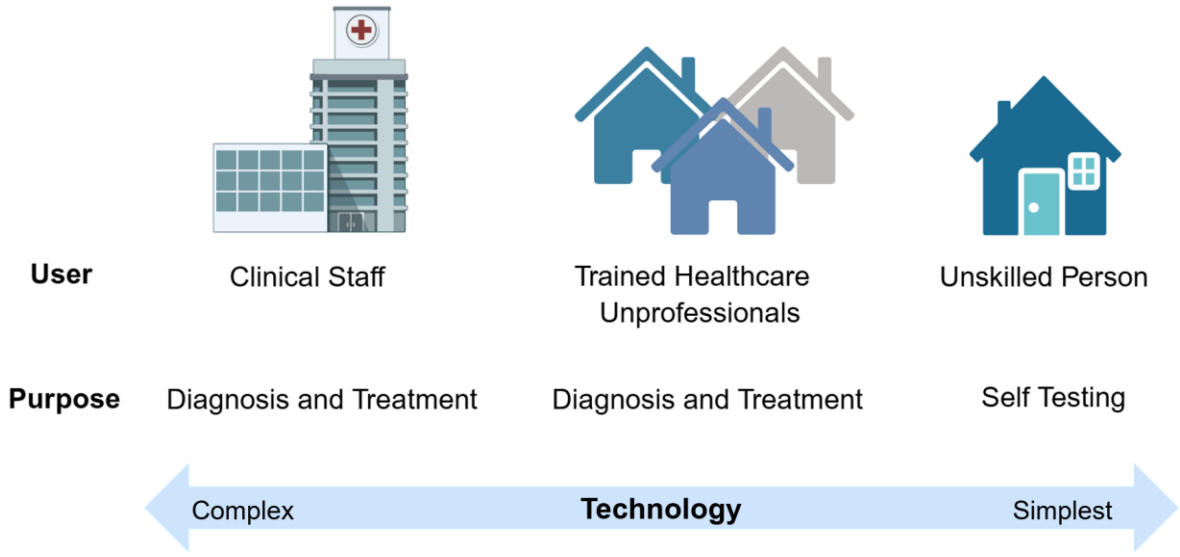

Figure 2. POCT platform: From skilled clinical staff to untrained person

1.3.1 POCT biosensors

Point-of-care testing (POCT) biosensors can be systematically classified based on the materials employed in their fabrication. The properties of these materials play a critical role in determining the device's performance, manufacturing cost, flexibility, and suitability for application in various environments. Depending on their format, they can be categorized as chip-based, paper-based, or film-based platforms. To provide a concise overview, Table 2 summarizes representative POCT biosensors based on device format and working principles.

Table 2. Overview of POCT biosensors platforms and their corresponding working principles.

Category	Method	Working principle
Chip-based	Microfluidic chip-based biosensors	Target proteins are detected through specific biomolecular recognition with signal transduction via electrochemical or optical readouts
Film-based	Film-based biosensors	Target binding on functionalized thin-film substrates is converted into measurable optical or electrical signals
Paper-based	Lateral flow immunoassay (LFIA)	Capillary-driven antigen–antibody interactions generate visible or fluorescent signals on porous membranes

1.3.1.1 Chip-based biosensors

Chip-based biosensors typically integrate microfluidic technology, miniaturized electronics, and bioanalytical elements onto a small substrate, which is commonly

fabricated from materials such as glass, silicon, polymers, hydrogel, paper[30]. These platforms allow precise manipulation of small amount of fluid, enabling the development of highly automated and multiplexed detection systems[31]. The primary advantages of chip-based biosensors include automated operation, reduced reagent consumption, minimized human error, and significantly enhanced analytical throughput. The integration of microvalves, mixers, and reaction chambers facilitates complex workflows such as sample preparation, incubation, washing, and detection in a fully enclosed, contamination-free environment.[32] Various signal transduction mechanisms have been implemented in chip-based biosensors for protein detection, including electrochemical, fluorescent, chemiluminescent, and surface plasmon resonance (SPR)-based readouts.[33] For example, digital microfluidics has been employed in platforms such as Simoa (single molecule array), which achieves ultra-sensitive detection of protein biomarkers like interleukins or cardiac troponins at femtomolar or even attomolar levels.[34] Similarly, droplet-based microfluidics can encapsulate single immunoreactions in picoliter droplets, significantly enhancing sensitivity and reaction speed, as demonstrated in rapid assays for C-reactive protein (CRP).[35]

1.3.1.2 Film-based biosensors

Film-based biosensors utilize thin films composed of functionalized polymers or nanomaterials as platforms for the selective detection of proteins. These films serve as solid-phase substrates that can be easily modified with biological recognition elements such as antibodies, aptamers[36], or molecularly imprinted polymers (MIPs)[37]. For example, transparent polyester films have been used as substrates in film-based biosensors for Zika viral pathogen detection, owing to their ability to endure thermal cycling and amplification conditions required during the assay process.[38] The simplicity of their structure and compatibility with various signal transduction methods make film-based biosensors highly versatile for diagnostic applications.

1.3.1.3 Paper-based biosensors

Paper-based biosensors are widely used due to their low cost, portability, and user-friendly design, making them ideal for on-site and self-testing applications, particularly in resource-limited settings.[39] Most notably represented by lateral flow immunoassays (LFIAs), these sensors utilize porous materials such as filter paper or nitrocellulose membranes, which facilitate sample transport through capillary action without the need

for external pumps or power sources. Their simplicity allows for rapid, qualitative results often visible to the naked eye, and increasingly, smartphones can be used to capture and quantify signals for semi-quantitative or quantitative analysis. Paper-based biosensors are widely employed in infectious disease screening (e.g., COVID-19 and influenza), clinical diagnostics (e.g., pregnancy testing), and food safety monitoring (e.g., allergen detection), particularly in resource-limited or at-home settings.[40,41]

Among the aforementioned biosensor platforms, paper-based LFIA has become a tool for protein analysis and attracted increasing attention.[42, 43, 44] Compared with the detection methods mentioned above, LFIA has the advantage of achieving convenient, rapid, low-cost analysis without the requirement for skilled personnel or professional training.[45, 46] One of the most widely used and effective formats is the sandwich immunoassay, which provides high sensitivity and specificity for protein detection across various point-of-care applications.

1.4 Lateral Flow Immunoassay (LFIA) Process via Sandwich Format

In a LFIA, the sample is first applied to the sample pad, from which it flows forward driven by capillary force. There, it encounters detection probes that specifically bind to the target analyte (Figure 3). These nanoparticles act as visible or fluorescent signal reporters, including gold (Au)[47], silver (Ag)[48], lanthanide-doped nanoparticles[49,50] and quantum dots (QDs)[51,52]. These probes bind specifically to the target analyte, forming the immunocomplexes. The resulting complexes then migrate toward the test line, which is coated with capture antibodies that recognize a different epitope on the same analyte. This interaction forms a sandwich structure, where the analyte is bound between the detection and capture antibodies. Subsequently, excess reporter-antibody conjugates, regardless of whether they are bound to the target analyte, continue to migrate to the control line[53]. The control line is coated with secondary antibodies (e.g., anti-species antibodies) that recognize the detection antibodies, thereby capturing the labeled probes and generating a signal to confirm proper fluid flow and assay validity. The remaining fluid is finally absorbed by the absorption pad.

This sandwich format significantly enhances assay specificity by utilizing dual-antibody recognition of the analyte, effectively minimizing non-specific binding.

Furthermore, the integration of nanoparticle-based detection probes enables signal amplification, thereby enhancing sensitivity and lowering the limit of detection (LOD).

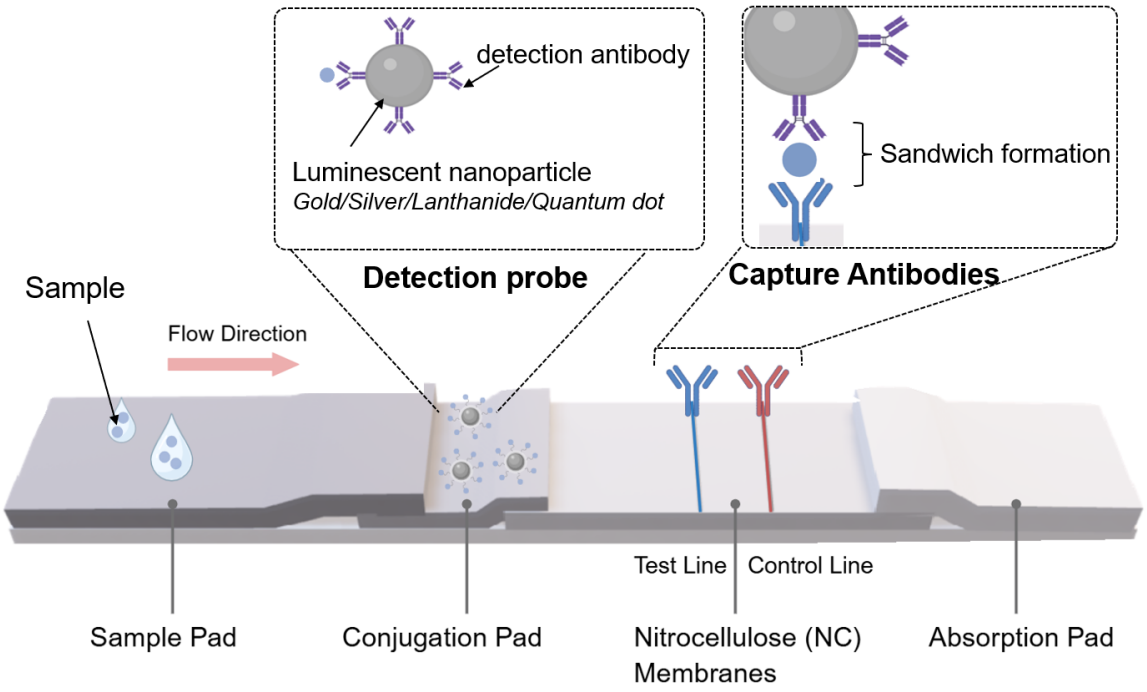

Figure 3. Schematic illustration of LFIA principle and sandwich format formation

1.5 The probes for sandwich format in LFIA

To provide a representative overview of the analytical performance of LFIAs across different diagnostic scenarios, two model protein biomarkers are selected: prostate-specific antigen (PSA) for clinical diagnostics and SARS-CoV-2 antigens for infectious disease testing. These two biomarkers represent distinct but complementary application contexts, that are low-abundance cancer biomarkers and rapidly emerging infectious disease targets, therefore widely used to benchmark the performance of LFIA-based detection strategies in the literature.

1.5.1 PSA detection

Prostate-specific antigen (PSA) is a glycoprotein secreted by epithelial cells of the prostate gland, which recognized as a clinically relevant biomarker for prostate cancer screening, diagnosis, and monitoring. PSA levels in blood can reflect both benign and malignant conditions, but elevated PSA concentrations, especially above 4 ng/mL are commonly associated with early-stage prostate cancer.[54] Due to its well-characterized

clinical relevance, ease of measurement, and established diagnostic thresholds, PSA becomes one of the most routinely studied protein biomarkers in clinical practice.

PSA is widely recognized as a model biomarker for assessing the analytical performance of sandwich-format lateral flow immunoassays (LFIAs), owing to its clinical relevance and inherently low physiological concentration. In healthy individuals, PSA levels are typically below 1 ng/mL, particularly in the early stages of disease progression. This low abundance poses a considerable analytical challenge, thereby rendering the LOD a key metric for evaluating the sensitivity of LFIA-based diagnostic platforms. Table 3 provides a comparative overview of representative nanomaterial-based probes and detection strategies employed in sandwich-format LFIAs for PSA detection. A variety of nanoparticle systems, including gold nanoparticles (AuNPs), silver nanoparticles (AgNPs), quantum dots (QDs), and core-shell structures such as Au@Ag, have been integrated with diverse readout modalities, ranging from conventional colorimetric detection to smartphone-assisted platforms. These assays exhibit varied analytical performance, with reported LODs ranging from approximately 0.1 ng/mL to 1.1 ng/mL and linear dynamic ranges typically spanning from 0.1 to 100 ng/mL.

Table 3. The Probes for sandwich format LFIA in PSA detection

	Probe	**Detector**	**LOD (ng/mL)**	**Linear range (ng/mL)**	**Ref**
AuNPs	SiO_2@Au	Colorimetric detector	0.12	-	[55]
	AuNPs	Portable reader	0.17	1-128	[56]
	AuNPs	Electrochemical detector	0.15	0.011-20	[57]

AgNPs	Silica NPs@Ag	Visual	1.1	0.1-100	[58]
QDs	Silica NPs@QDs	Smartphone-based reader	0.138	0.1-100	[59]
	QD@SiO_2	Portable fluorescence reader	1.0754	-	[60]
Dual Detection	Au@Ag	Commercialized reader	0.1	0.1-100	[61]

1.5.2 SARS-CoV-2 antigen detection

Beyond PSA, LFIAs have been widely developed for the detection of SARS-CoV-2 antigens. Key viral proteins, particularly the nucleocapsid (N) and spike (S) proteins, serve as optimal diagnostic targets owing to their high expression levels and strong immunogenicity during the early stages of infection. As summarized in Table 4, a wide range of nanoparticle-based probes have been integrated with diverse signal readout platforms to enhance assay sensitivity and usability. Nevertheless, the LODs reported by many current LFIA systems, typically in the range of 0.1 to 1 ng/mL, remain inadequate for the reliable identification of low viral load specimens, particularly in asymptomatic or early-stage cases.

Table 4. The Probes for sandwich format LFIA in SARS-CoV-2 protein detection

	Probe	**Target**	**Detector**	**LOD (ng/mL)**	**Linear range (ng/mL)**	**Ref**
AuNPs	AuNPs	N protein	Colorimetric detector	0.038	0.03-1000	[62]

		S1 protein	Smartphone-based reader	0.63	0.05-200	[63]
Dual Detection	Ag@Au	N protein	808 nm laser and a thermal camera	1	0.05-100	[64]
	Ag^{MBA}@Au	S protein	Portable Raman spectrometer	1	0.001-10	[65]
QDs	QD nanobeads	N protein	Portable fluorescent strip reader	0.01	0.005-100	[66]

Despite significant improvements in assay design and signal amplification strategies, the current LODs achieved by many nanoparticle-enhanced LFIA systems remain relatively high when benchmarked against the ultra-low concentrations of biomarkers typically present during the early stages of disease. For instance, while LODs in the range of 0.01-1 ng/mL may be sufficient for mid-to-late-stage detection, they often fall short of the picogram per millilitre sensitivity required for reliable early diagnosis, especially in asymptomatic or low viral load COVID-19 cases and in the initial onset of prostate cancer. This limitation can be attributed to several factors, most notably elevated background noise arising from the intrinsic optical properties of the above NPs themselves. Moreover, many conventional LFIA platforms rely on visual readout, which inherently limits sensitivity due to the relatively high detection threshold of the human eye and the inability to distinguish subtle signal differences at low analyte concentrations. This limitation underscores the pressing need for further optimization in multiple aspects of assay design, including the sensitivity of nanoparticle probes, the efficiency of signal transduction mechanisms, and the suppression of nonspecific background signals, to achieve the ultra-low LODs necessary for accurate and reliable early-stage diagnostics in clinical settings.

1.6 Lanthanide-doped upconversion nanoparticle (UCNP)

To overcome the sensitivity limitations inherent in conventional fluorescence assays and address the increasing need for detecting low-abundance biomarkers, UCNPs have been introduced as novel signal reporters. UCNPs are lanthanide-doped crystalline nanomaterials capable of converting near-infrared (NIR) excitation photons into higher-energy visible emissions via a nonlinear optical process known as the anti-Stokes shift (Figure 4)[67,68]. This unique upconversion mechanism is mediated through energy transfer between sensitizer ions (commonly Yb^{3+}) and activator ions (such as Er^{3+} or Tm^{3+}) embedded within a low-phonon host matrix, typically $NaYF_4$. The activators undergo stepwise excitation to higher electronic states (e.g., $^4I_{11/2}$, $^4F_{9/2}$, $^4S_{3/2}$, $^2H_{11/2}$) followed by radiative relaxation, emitting photons in the visible range (green or red, depending on the activator). Lanthanide ions possess multiple metastable energy states, making them highly suitable for photon upconversion processes. Originally developed for applications in solid-state lasers and photonics, the unique ability of UCNPs to convert deeply penetrating NIR excitation into visible light has spurred their adaptation for biomedical applications, especially in vitro diagnostics (IVD) [69] . Their excitation in the NIR window circumvents interference from endogenous biological fluorophores, substantially reducing background autofluorescence and nonspecific signals, thereby improving assay sensitivity and specificity.[70, 71]

To function reliably as luminescent probes in immunoassays, UCNPs must not only exhibit favorable optical properties but also possess well-defined structural features and stable colloidal behaviour in aqueous environments. Accordingly, characterization techniques such as transmission electron microscopy (TEM) and dynamic light scattering (DLS) are employed in this work to assess nanoparticle morphology, size distribution, and dispersion stability, providing essential validation of UCNP synthesis and surface modification prior to their application in biosensing systems.

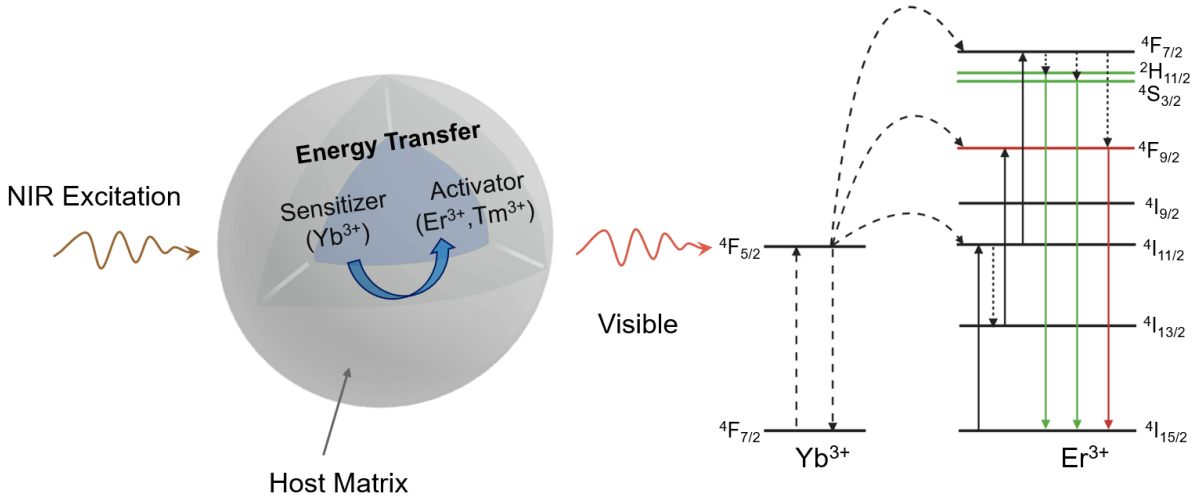

Figure 4. The structure and energy transfer of UCNPs

UCNPs offer several additional benefits that make them ideal fluorescent probes for bioanalytical applications. These include outstanding photostability, chemical resistance, and thermal robustness. Unlike conventional organic dyes, which are prone to rapid photobleaching, UCNPs maintain fluorescence over prolonged storage and extended illumination periods.[72] Moreover, unlike quantum dots, UCNPs do not exhibit photo-blinking behaviour, which can otherwise lead to intermittent signal loss during imaging or detection. The emission properties of UCNPs can also be precisely tuned by modifying the host crystal lattice, selecting appropriate lanthanide dopants, and adjusting their concentrations. This enables the generation of multiple discrete emission wavelengths from a single excitation source (Figure 5). Multicolour UCNPs can therefore be applied in multiplexed detection assays, where multiple analytes are simultaneously identified by encoding each target with a uniquely emissive nanoparticle.[73] Such capabilities underscore the strong potential of UCNPs in advanced bioassays and point-of-care diagnostics that demand high sensitivity, excellent stability, and robust multiplexing performance.

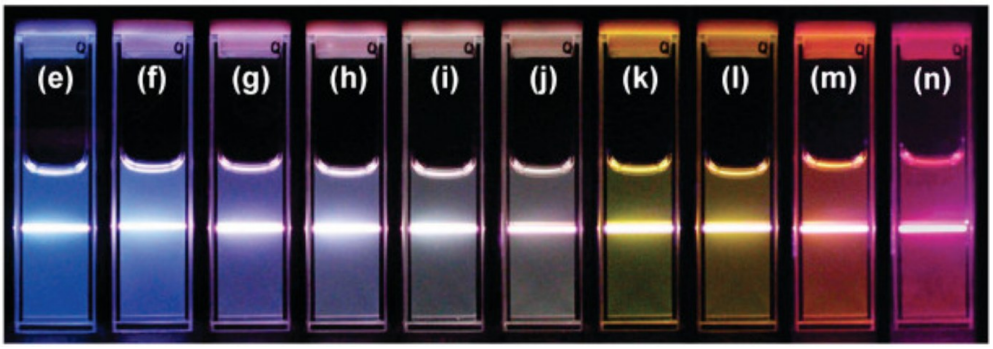

Figure 5. UCNPs doped with different concentrations of Yb^{3+}, Er^{3+}, and Tm^{3+} showing multicolour emissions. Reproduced from ref.[73].

1.6.1 Low doping UCNP

In typical UCNPs systems, the doping concentrations of lanthanide ions are intentionally kept at relatively low levels to mitigate luminescence quenching effects. Specifically, sensitizer ions such as Yb^{3+} are generally introduced at concentrations below 20 mol%, while activator ions (e.g., Er^{3+}, Tm^{3+}, Ho^{3+}) are doped at levels typically below 2 mol%. This conservative doping approach is primarily driven by the phenomenon of concentration quenching; wherein excessive dopant concentrations promote non-radiative energy losses through intensified cross-relaxation and inter-ionic interactions. These effects result in a substantial reduction in upconversion luminescence efficiency.

The challenge posed by concentration quenching is particularly pronounced in nanoscale luminescent materials (Figure 6a). As illustrated in Figures 7b and 7c, high doping concentrations reduce the spatial distance between dopant ions, significantly increasing the likelihood of energy transfer events. This facilitates two major quenching pathways: (i) energy migration within the sensitizer-sensitizer network that funnels excitation energy to the nanoparticle surface, where a high density of surface quenching sites exists (Figure 6b), and (ii) cross-relaxation between activator ions, which causes stepwise emission loss during radiative transitions (Figure 6c). The combined effects of these pathways lead to a marked decrease in luminescent output.

To minimize parasitic interactions such as non-radiative energy transfer and concentration quenching, doping concentrations in UCNPs are limited to maintain sufficient spatial separation between lanthanide ions. This strategy effectively

suppresses non-radiative decay pathways and preserves emission efficiency. The critical inter-ionic distance, commonly characterized by the Förster critical radius, is typically estimated to fall within the range of 2 to 6 nm. Correspondingly, optimal dopant concentrations are generally maintained below ~10^{-3} M for organic dye-doped silica systems and around ~10^{-2} M for UCNPs. Correspondingly, optimal dopant concentrations are generally maintained below ~10^{-3} M for organic dye-doped silica systems and around ~10^{-2} M for UCNPs. Specifically, β-phase alkaline rare-earth fluorides (β-$NaREF_4$), which serve as efficient host lattices for upconversion, commonly incorporate sensitizers (e.g., Yb^{3+}) at approximately 20 mol% and activators (e.g., Er^{3+}, Tm^{3+}) at concentrations below 2 mol%.

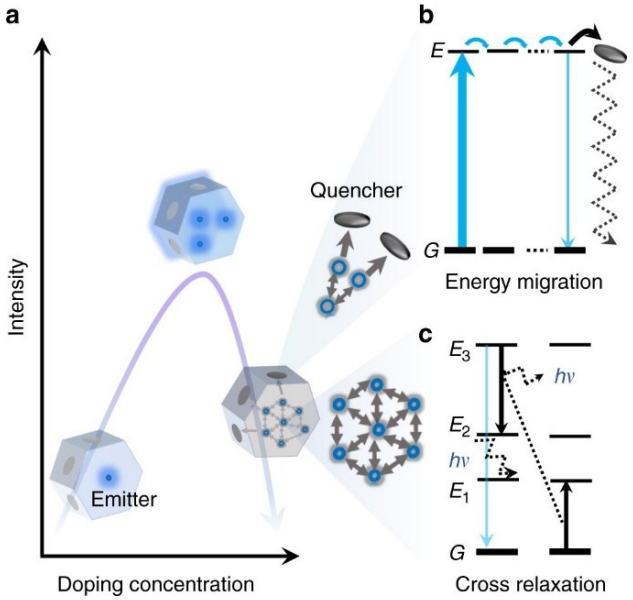

Figure 6. Concentration quenching in UCNPs. a, Increasing lanthanide doping raises sensitizer and emitter numbers and shortens their distance, enhancing emission brightness. However, exceeding an optimal doping level leads to concentration quenching, which reduces energy transfer efficiency. This quenching mainly arises from (b) non-radiative energy migration to surface quenchers and (c) cross-relaxation non-radiative losses. Reproduced from ref.[74].

Table 5. Application of low-doping UCNPs in sandwich-format LFIAs for the detection of various biomarkers

Doping	Target	Detector	LOD (ng/mL)	Ref
18% Yb, 2% Er	PSA	Commercialized strip reader	0.24	[75]
20%Yb, 2%Er	Dexamethasone	Optical density scanner	0.1	[76]
18% Yb, 2% Er	Tumorigenicity 2	Smartphone-based reader	1	[77]
25% Yb, 2% Er	Zearalenone	Commercialized spectrometer	0.1	[78]
20%Yb, 2%Er	C-reactive protein	Portable fluorescence sensor	0.05	[79]

Although low doping concentrations are traditionally employed to suppress concentration quenching and maintain upconversion efficiency, this strategy inherently limits the number of active dopant ions, thereby reducing the overall absorption cross-section and photon emission. Consequently, the achievable signal strength is compromised, restricting the assay's detection sensitivity. As summarized in Table 5, reported LODs for existing UCNP-based assays generally fall within the hundreds of picograms to nanograms range, indicating that doping concentration critically affects upconversion emission efficiency and overall luminescence intensity. Therefore, further optimization of doping levels is necessary to enhance signal output and meet the requirements for ultrasensitive detection, especially for early-stage disease biomarkers.

1.6.2 Highly doped UCNPs

One of the promising strategies to overcome the traditional limitations of concentration quenching is to increase the excitation power density. Recent studies have demonstrated that under sufficiently high excitation conditions, the luminescence efficiency of heavily doped UCNPs can be significantly enhanced, challenging the conventional view that high dopant concentrations inevitably result in emission suppression. Figure 7a illustrates the relationship between Tm^{3+} doping concentration and the integrated upconversion luminescence intensity of UCNPs under varying excitation power densities.[80] Three doping levels, 0.5%, 4%, and 8% Tm^{3+}, were compared across an excitation irradiance range from 1.6×10^4 to 2.5×10^6 $W \cdot cm^{-2}$. At low excitation intensities, all three samples exhibit relatively weak emission with minimal differences in output. However, as the excitation power increases, a distinct divergence in luminescence enhancement could be observed. While the 0.5% Tm^{3+}-doped UCNPs show only a moderate 5.6-fold increase in luminescence, the 4% and 8% Tm^{3+} samples exhibit markedly higher enhancement factors of 71 and 1105, respectively. The high brightness of these Tm^{3+}-doped UCNPs allows the tracking of single nanoparticles in living cells through an optical microscope.

A similar trend is observed in single-particle measurements (Figure 7b), where the luminescence intensity of individual UCNPs dramatically increases as the laser intensity is raised from 10^4 to 10^6 $W \cdot cm^{-2}$.[81] At low laser power densities (10^4-10^5 $W \cdot cm^{-2}$), the luminescence difference between the two doping levels is minimal, with the 2% Er^{3+} sample even slightly outperforming the 20% Er^{3+}. This is consistent with the conventional understanding that high dopant concentrations can lead to quenching effects at low excitation power. However, as the excitation intensity increases beyond 10^5 $W \cdot cm^{-2}$ to 10^6 $W \cdot cm^{-2}$, the emission intensity of the 20% Er^{3+}-doped UCNPs exhibits a dramatic exponential increase, far surpassing that of the 2% Er^{3+} sample. This shift indicates that under high excitation conditions, energy transfer efficiency and photon absorption become dominant over quenching mechanisms, effectively overcoming concentration quenching. The right optical images also support this observation; they show a progressive enhancement in particle brightness with increasing laser power. These results collectively suggest that the threshold for concentration quenching can be shifted by modifying excitation parameters.

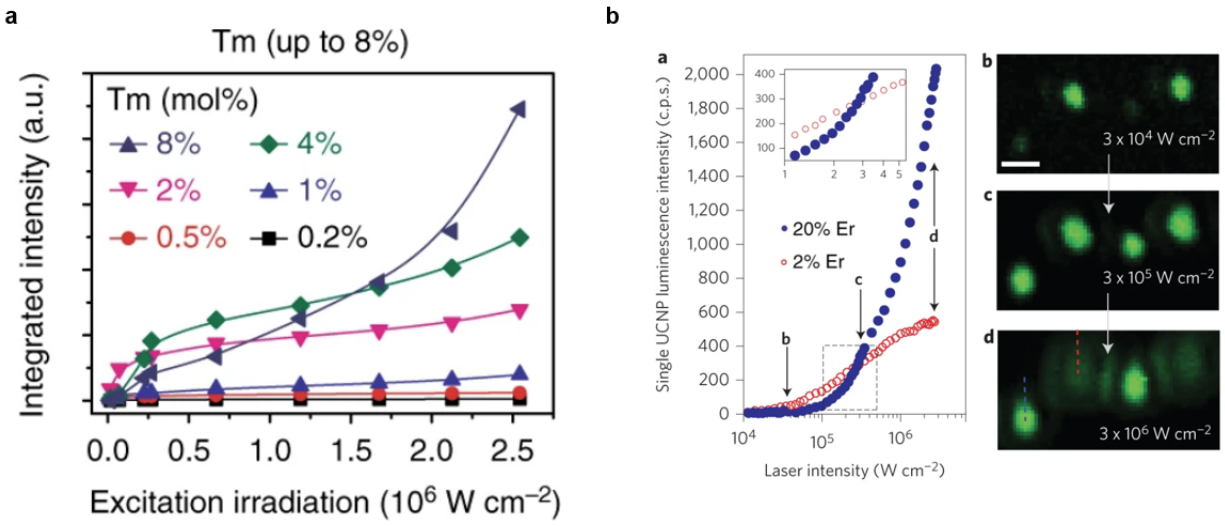

Figure 7. Strategy for overcoming concentration quenching in upconversion nanocrystals. a, Integrated UCL intensity of Tm^{3+}-doped (0.2-8%) nanocrystals under increasing excitation irradiance. Reproduced from ref. [80]; b, Upconversion luminescence intensity of single 8 nm UCNPs doped with 20% Yb^{3+} and either 2% or 20% Er^{3+}. Reproduced from ref. [81].

It should be noted that, for the majority of bioanalytical applications involving protein detection, moderate excitation power densities are generally sufficient to achieve reliable upconversion signal generation. Under such conditions, highly doped UCNPs primarily serve to ensure adequate brightness and signal robustness, rather than to exploit saturation effects that typically arise only under high-power excitation or imaging scenarios. Nevertheless, the power-dependent activation behavior of highly doped UCNPs offers a valuable strategy for enhancing signal output in optical biosensing systems. When operated at elevated excitation intensities, these nanoparticles can exhibit substantially increased emission intensity, which is particularly advantageous for applications requiring high photon flux or imaging-based readout. Importantly, even under moderate excitation power densities commonly employed in practical bioanalytical platforms, the enhanced brightness associated with higher dopant concentrations enables improved signal-to-noise ratios and more reliable quantitative detection.

Table 6. Application of highly doped UCNPs in sandwich-format LFIAs for the detection of various biomarkers

Doping	Target	Detector	LOD (ng/mL)	Ref
40%Yb, 4%Er	N protein	Customized strip reader	0.01	[82]
60% Yb, 8% Er	PSA	Smartphone-based reader	0.089	[42]
40%Yb, 4%Er	CD44	Customized strip reader	0.015	[83]
	FKBPL		0.01	

Consistent with this observation, a growing number of recent studies have demonstrated that UCNPs with elevated dopant concentrations, such as 40–60% Yb^{3+} and 4-8% Er^{3+}, can achieve remarkably low limits of detection in sandwich-format lateral flow immunoassays, often reaching the picogram-per-millilitre level, without requiring high-power excitation. As summarized in Table 6, these high-brightness UCNPs enable sensitive signal readout even when paired with compact detection platforms, including customized strip readers and smartphone-based systems. This enhanced luminescence output translates directly into improved assay sensitivity, facilitating the detection of low-abundance biomarkers such as viral nucleocapsid proteins[82] and cancer-associated targets including PSA[42], CD44, and FKBPL[83].

Taken together, these findings indicate that highly doped UCNPs provide a versatile signal amplification strategy across a broad range of excitation regimes. When combined with the inherent advantages of sandwich immunoassay formats, such as high specificity, compatibility with multiplexing, and operational simplicity. This approach offers a promising pathway toward ultrasensitive point-of-care diagnostic platforms that remain compatible with low-power, portable instrumentation.

In addition to considerations regarding dopant concentration and doping strategies, water-induced quenching is another critical factor that limits the performance of UCNPs in bioanalytical applications. In aqueous environment, the high-energy vibrational overtones of O-H bonds can strongly couple with the excited states of lanthanide ions, promoting non-radiative relaxation pathways and leading to a substantial reduction in upconversion luminescence intensity, particularly for surface-exposed activator ions[84, 85]. This effect is especially pronounced in biological and clinical samples, where UCNPs are inevitably operated in water-rich media, thereby posing a significant challenge for sensitive and reliable signal readout. To address this limitation, extensive efforts have been devoted to rational nanoparticle design and surface engineering, including the introduction of inert shell layers and polymer-based surface modification[88, 86], which effectively suppress non-radiative energy dissipation and enhance luminescence stability in aqueous environment. These strategies form the basis for the UCNP conjugation and surface functionalization approaches described in the following chapter.

1.7 Surface Functionalization of UCNPs

UCNPs have attracted significant interest in bioanalytical applications owing to their unique optical properties. However, their direct use in biological environments is hindered by hydrophobic surface ligands introduced during synthesis, necessitating subsequent surface functionalization to achieve biocompatibility. A variety of synthetic strategies have been developed for the preparation of UCNPs, including coprecipitation, thermal decomposition, solvothermal synthesis, high-temperature coprecipitation, hydrothermal methods, and sol–gel processes. In particular, high-boiling-point organic solvents are commonly employed to achieve precise control over crystal growth, enabling the synthesis of highly monodisperse UCNPs with uniform size and morphology. For instance, oleic acid is frequently used both as a reaction medium and as a surface-capping ligand, coordinating to the nanoparticle surface to form a stable hydrophobic organic layer. While this hydrophobic surface is beneficial for controlling nanoparticle growth, it significantly limits the dispersibility and practical usability of UCNPs in aqueous and biological environments.

To address these limitations, extensive efforts have been devoted to developing surface modification strategies that convert hydrophobic UCNPs into hydrophilic, water-dispersible, and biocompatible nanoprobes. Beyond improving colloidal stability in aqueous media, surface functionalization also enables the introduction of reactive functional groups, such as carboxyl or amino moieties, which facilitate subsequent bioconjugation with biomolecules including antibodies, enzymes, and nucleic acids. As reported in the literature, the construction of UCNP-based bioprobes typically involves two sequential steps: surface functionalization and biomolecular conjugation (Figures 8 and 9). These steps are critical for ensuring stable attachment of biomolecules while preserving their biological activity and target-binding capability, thereby enabling specific molecular recognition and sensitive detection in complex biological matrices.

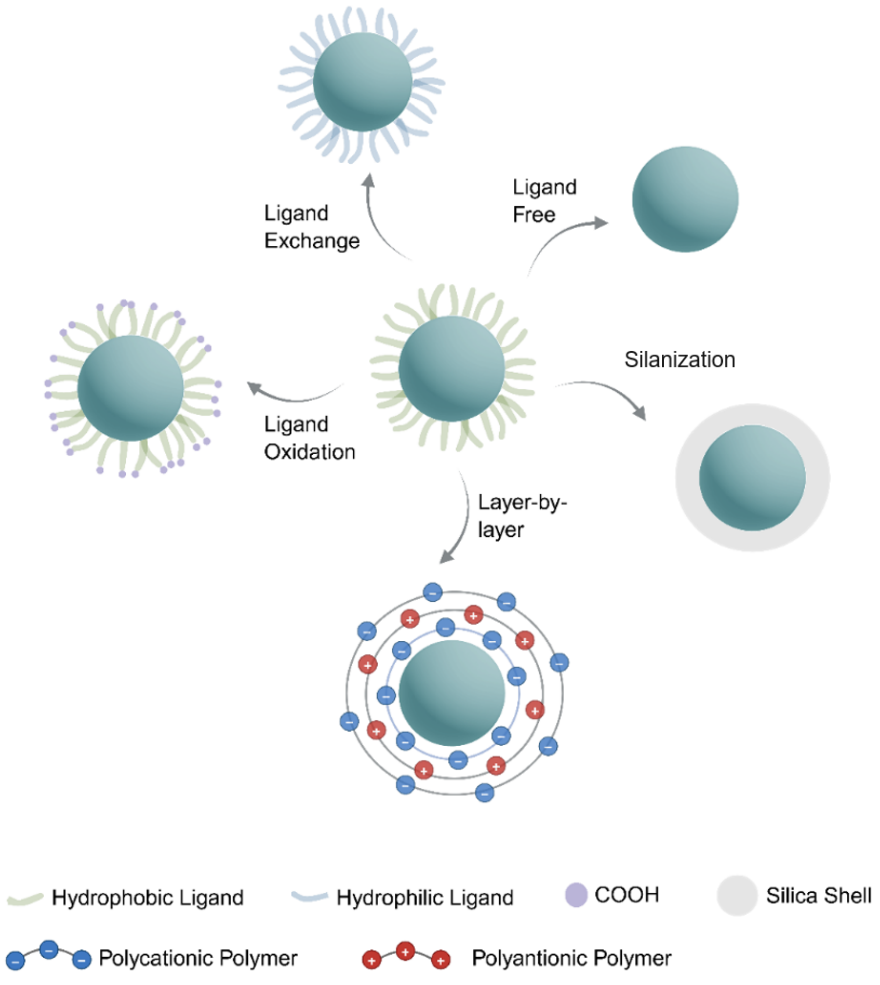

Figure 8. Schematic overview of common surface modification strategies for UCNPs to enable aqueous dispersibility and biofunctionalization. Hydrophobic UCNPs synthesized in organic solvents can be rendered water-dispersible and functionally active through ligand oxidation, layer-by-layer, silanization, ligand free and ligand exchange.

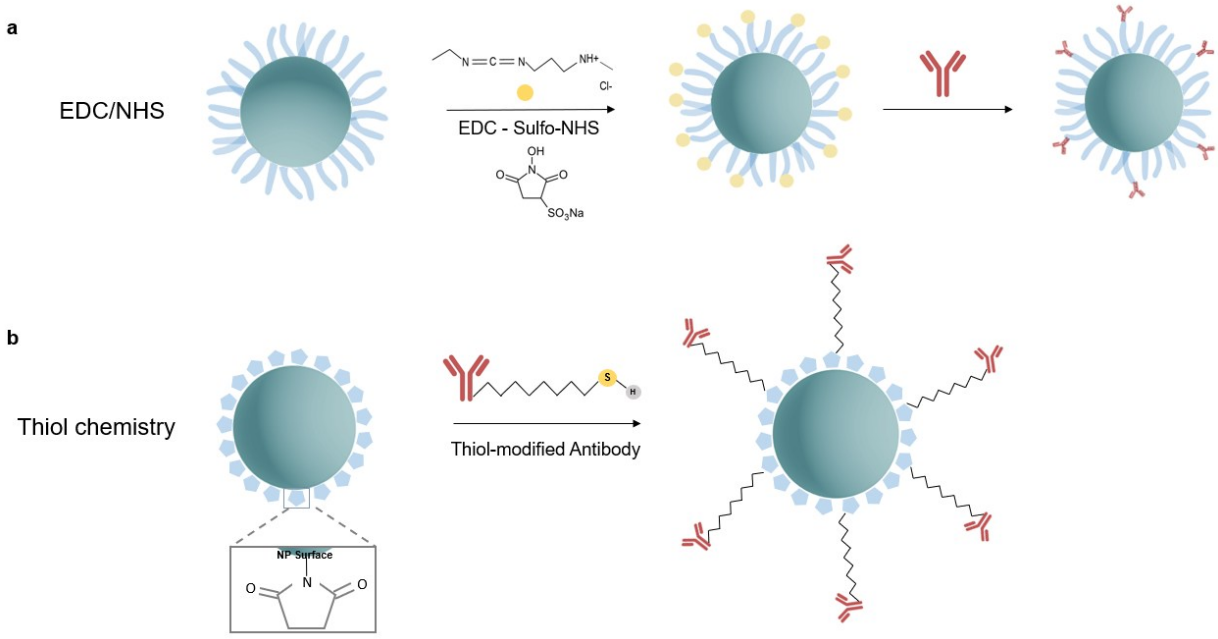

Figure 9. Schematic illustration of two common covalent conjugation strategies for antibody-nanoparticle bioconjugates. a, EDC/NHS coupling chemistry: carboxyl groups on the nanoparticle surface are activated by EDC and sulfo-NHS to form NHS-esters, which then react with primary amines on the antibody to form stable amide bonds. b, Thiol- maleimide chemistry: thiol groups on site-selectively reduced antibodies react with maleimide-functionalized nanoparticles to form stable thioether bonds, allowing for oriented and efficient conjugation. Regenerated from[87].

1.7.1 Surface modification Method

1.7.1.1 Ligand Oxidation

A direct strategy for rendering hydrophobic nanoparticles hydrophilic involves the oxidative transformation of surface ligands. This method has been primarily applied to OA and oleylamine (OM), where unsaturated carbon–carbon double bonds are

oxidized to generate polar functional groups such as carboxyl or epoxy moieties. Common oxidizing agents include the Lemieux–von Rudloff reagent[88], ozone[89], and 3-chloroperoxybenzoic acid.[90] The Lemieux–von Rudloff reagent, commonly employed for oxidative cleavage of double bonds, consists of catalytic amounts of permanganate (MnO_4^-) and stoichiometric amounts of periodate (IO_4^-). In this reaction, MnO_4^- initially oxidizes the carbon-carbon double bond and is subsequently regenerated by IO_4^-[91]. After the oxidation, the azelaic acid-functionalized nanoparticles exhibit enhanced hydrophilicity and offer reactive sites for subsequent bioconjugation.[92] However, it is only applicable to surface ligands that contain unsaturated carbon–carbon bonds, restricting its generalizability. Secondly, the formation of manganese dioxide (MnO_2) as a by-product in Lemieux–von Rudloff oxidation poses a challenge, as MnO_2 is difficult to remove and can adhere to the nanoparticle surface, leading to decreased luminescence intensity.[93]

Alternatively, azelaic acid-modified nanoparticles can also be prepared through ozonolysis[84], wherein ozone reacts with the double bond of the oleate ligand, initially forming epoxide intermediates[94]. In contrast to Lemieux–von Rudloff oxidation, this method yields aldehyde groups instead of carboxylic acids. These aldehydes can subsequently be functionalized with amine-containing molecules, enabling further surface modification.[92,95] It is important to note that this oxidative strategy is only applicable to ligands containing unsaturated carbon–carbon double bonds. However, the relatively short chain length of azelaic acid may limit its ability to fully shield the nanoparticle surface from water-induced luminescence quenching.[96] Besides, although the ozonolysis effectively in avoiding MnO_2 formation, involves more complex processing steps and requires precise control of reaction conditions, which may limit its scalability and reproducibility in large-scale applications.

1.7.1.2 Ligand Free

The ligand-free UCNPs can be prepared by removing hydrophobic surface ligands through acid treatment and excess ethanol. The nanoparticles were exposed to HCl at pH 4, leading to protonation of the surface-bound oleate ligands and subsequent detachment of oleic acid from the nanoparticle surface.[97] The treatment of OA-UCNPs with FA makes the ligand-free UCNPs dispersible in water and positively charged bare UCNPs generate, favouring the attachment of water-soluble capping molecules by sequential surface functionalization, such as poly(acrylic acid) (PAA),

polyvinylpyrrolidone (PVP), and polyethylenimine (PEI).[98] The resulting cationized nanoparticles exhibited excellent aqueous dispersibility and strong upconversion luminescence. However, this acid-mediated ligand removal method yields a relatively low surface modification efficiency, typically ranging between 30% and 35%.[99] In contrast, Jurga et al. reported that the highly water-stable colloidal dispersions with reaction yields can reach up to 96% depending on different concentrations of hydrochloric acid and varying reaction times.[100] The resulting exposed lanthanide ions exhibited strong coordination capabilities, allowing for efficient conjugation with biocompatible molecules in aqueous environments. However, the long exposure to acidic conditions can lead to partial nanoparticle dissolution and precipitation of rare earth components.

1.7.1.3 Silanization

Silica is one the most widely used materials for coating the surface of UCNPs. The presence of a silica shell has minimal or negligible impact on the luminescence properties of UCNPs[101,102]. A slight decrease in emission intensity is typically attributed to light scattering effects of both excitation and emission signals by the silica layer.[103] This transparent, biocompatible, and non-toxic properties of silica makes it particularly advantageous for optical bioanalytical applications and has led to its extensive use in modifying the surfaces of nanomaterials.

UCNPs with hydrophilic surfaces are typically coated with a silica shell using a modified Stöber method, whereas hydrophobic UCNPs are more commonly coated via a reverse microemulsion technique. The original Stöber process, which involves the hydrolysis and condensation of tetraalkyl orthosilicates in alcoholic solvents in the presence of ammonia to produce monodisperse silica particles, can be adapted to facilitate uniform silica shell growth on the surface of UCNPs.[104,105] In contrast, hydrophobic UCNPs are more commonly coated using a reverse microemulsion technique, which allows precise control over silica shell thickness and morphology. The reverse micelles function as nanoscale reactors, enabling the hydrolysis and condensation of tetraalkyl orthosilicates, such as tetraethyl orthosilicate (TEOS), to form a silica shell[106,107]. A surfactant is used to form reverse micelles in a nonpolar solvent such as cyclohexane, which creating small aqueous compartments. The addition of ammonia initiates the hydrolysis and condensation of the silica precursor, leading to the formation of a silica shell around the UCNPs. The morphology of the

micelles is influenced by the concentration of surfactant; lower amounts typically produce spherical micelles, while higher concentrations can result in rod-like structures, which may encapsulate multiple UCNPs within a single silica shell.[108] Silanization can be carried out either simultaneously with the silica shell formation or as a subsequent step following shell growth. However, it is difficult to precisely control the uniformity of the silica coating, and in some cases, multiple nanoparticles may become encapsulated within a single silica shell, leading to the formation of oversized composite particles[108, 109]. In addition, bare silica surfaces are prone to non-specific protein adsorption, which can increase background signals and compromise assay specificity in bioanalytical applications unless further surface passivation or functionalization is applied.

1.7.1.4 Layer-by-layer

Layer-by-layer (LbL) assembly is based on the sequential adsorption of oppositely charged species onto the surface of UCNPs. Electrostatic interactions between oppositely charged layers represent one of the most robust and stable non-covalent forces in nature.[110] Tailoring the LbL modification can be particularly beneficial for specific bio-applications of UCNPs, as it allows for precise control over surface functionality and interfacial properties. He et al. reported he Gd-doped UCNPs were functionalized with a dual-polymer system comprising polyethylene glycol (PEG) and two sequential layers of polyethylenimine (PEI).[111] The result suggested that compared with one-layer modification, two layers exhibited minimal cytotoxicity. Another group employed a layer-by-layer assembly strategy to sequentially deposit oppositely charged poly (allylamine hydrochloride) (PAH), poly (styrene sulfonate) (PSS), and a final layer of PAH on UCNPs to create hydrophilic PAH/PSS/PAH nanoparticles with amino-rich shells.[112] The LbL assembly process typically requires a long period to complete, as each reaction step involves relatively long reaction times and the success of the overall modification critically depends on the efficiency of each individual assembly step since any failure in one layer often necessitates restarting the entire procedure. In addition, the final particle size can increase significantly due to multilayer assembly, which may compromise flow rate in paper-based biosensors and limit their applicability in lateral flow or capillary-driven systems.

1.7.1.5 Ligand Exchange

Ligand exchange refers to the replacement of native hydrophobic ligands on the nanoparticle surface with hydrophilic ligands. This strategy enhances nanoparticle dispersibility in aqueous media and introduces reactive functional groups that facilitate subsequent bioconjugation with biomolecules, while generally preserving the chemical composition and optical properties of UCNPs. Common hydrophilic ligands used for ligand exchange include polyallylamine (PAH)[113], polyethylene glycol (PEG)[96], citrate (CIT)[114], and N,N-bis(phosphonomethyl)glycine (PG)[115]. Effective ligand exchange typically requires optimization of several parameters, including the the ratio of ligands and UCNPs and the selection of a suitable solvent[116]. The choice of solvent is determined by the solubility compatibility between the hydrophobic nanoparticles and the new hydrophilic ligand. The ligand's number and type of coordination sites play a crucial role in governing the efficiency of the ligand exchange process. This likely explains why multidentate ligands, which can form multiple coordination bonds simultaneously, are generally favoured over monodentate ligands in nanoparticle surface modification. Compared with using two separate polar solvents to dissolve the original surfactant and the new ligand, a single bipolar solvent such as tetrahydrofuran (THF) is often preferred due to its ability to promote high ligand exchange yields by enabling homogeneous mixing[117]. Dispersing nanoparticles and ligands in the same solvent promotes uniform interaction, leading to improved ligand exchange efficiency.

1.8 Bioconjugation

The previously discussed surface modifications of UCNPs have primarily focused on improving their dispersibility and stability in aqueous media through surface nanochemistry. However, for advanced applications, including tumor-targeted imaging, imaging, biosensing, and biomarker detection, the further bioconjugation with specific functional biomolecules is typically required to provide targeting ability and biological functionality.

1.8.1 Bioconjugation method

1.8.1.1 Non-covalent coupling

Non-covalent coupling is a straightforward and commonly used approach for the bioconjugation UCNPs, relying on weak intermolecular forces such as electrostatic interactions, hydrogen bonding, van der Waals forces, or hydrophobic effects to attach

biomolecules to the nanoparticle surface.[118] One of the main advantages of non-covalent strategies is their simplicity and minimal requirement for chemical modification, making them suitable for preserving the native structure and activity of sensitive biomolecules such as antibodies, enzymes, or nucleic acids. In particular, electrostatic adsorption is frequently employed by taking advantage of charge complementarity between the nanoparticle surface (e.g., positively charged polyallylamine-coated UCNPs) and negatively charged biomolecules.[119] However, the major limitation of non-covalent coupling lies in its relatively poor stability under physiological conditions, where changes in ionic strength, pH, or the presence of competing biomolecules can lead to desorption and loss of functionality.[120]

1.8.1.2 Covalent coupling

A more approach for nanoparticle–biomolecule conjugation involves the formation of a covalent coupling, which results from a chemical reaction between a reactive group on the nanoparticle surface and a complementary group present on the biomolecule. During the phase transfer process of UCNPs from organic solvents to aqueous environments, a range of functional groups, such as carboxyl (–COOH), amine ($–NH_2$), and maleimide (–MA), are typically introduced onto the nanoparticle surface.

1.8.1.2.1 EDC coupling

A widely adopted method for covalent bioconjugation is based on EDC (1-ethyl-3-(3-dimethylaminopropyl) carbodiimide) coupling chemistry, which enables the formation of stable amide bonds between carboxyl groups on the nanoparticle surface and primary amine groups on biomolecules such as antibodies (Figure 2a). In this process, carboxylic acid (–COOH) groups are first activated by EDC in the presence of N-hydroxysulfosuccinimide (sulfo-NHS) in an aqueous buffer, resulting in the formation of a reactive O-acylisourea intermediate[121, 122]. This intermediate subsequently reacts with the amine ($–NH_2$) groups of biomolecules to form a covalent amide linkage. While this technique is straightforward and broadly applicable, it does have certain limitations. Although EDC-mediated coupling may yield a heterogeneous population of nanoparticle, biomolecule conjugates with random orientations, which increase the non-specific binding. In addition, the activated O-acylisourea intermediate is susceptible to rapid hydrolysis in aqueous environments, which can reduce coupling efficiency and necessitate careful control of reaction conditions or the use of stabilizing agents such as sulfo-NHS[123]. EDC remains one of the most widely used reagents for

carboxyl, amine conjugation due to its efficiency and compatibility with aqueous conditions.

1.8.1.2.2 Thiol chemistry

Another widely used covalent bioconjugation strategy involves the reaction between thiol (-SH) groups on biomolecules and maleimide-functionalized surfaces, leading to the formation of stable thioether bonds under physiological conditions (Figure 2b). In this approach, thiol groups are generated by reducing native disulfide bonds in the antibody. Under carefully controlled and mild reduction conditions, disulfide bonds located in the hinge region of the Fc domain are preferentially reduced due to their higher accessibility and lower structural constraint compared to those in the variable regions, without introducing additional thiol-containing linker molecules. The schematic illustration in Figure 2b is intended to conceptually represent thiol-maleimide coupling and does not imply the presence of an extended aliphatic spacer between the antibody and the nanoparticle surface. This precision improves the orientation of the antibody on the nanoparticle surface, thereby enhancing its functional performance in various bioanalytical and diagnostic applications[124,125]. However, careful control of the oxidation state is necessary, as the presence of cysteine residues in the variable regions can affect conjugation specificity[126]. To address this limitation, disulfide rebridging chemistry has been developed, which achieves improved site specificity by selectively reconnecting the two cysteine residues originating from the same native disulfide bond, rather than reacting with freely generated thiols. In this strategy, the native disulfide bonds are intentionally cleaved and subsequently reconstituted into stable linkages, thereby preserving the original disulfide topology of the antibody and minimizing off-site modification[127, 128]. As a result, antibody structural integrity is maintained while conjugate homogeneity and orientation control are significantly improved.

1.9 Aim

While UCNPs have been reported as signal reporters in sandwich-LFIAs for protein detection, the present thesis does not aim to replicate existing UCNP-LFIA designs. Instead, it focuses on extending UCNP-enabled immunoassay strategies through application-driven assay development and assay-format-level innovation.

The first aim of this thesis is to develop a UCNP-based LFIA for the quantitative detection of A1 β-casein in milk and infant formula. This work establishes a practical application of UCNP-enhanced LFIA in food quality control, where high assay specificity and robustness are required to distinguish structurally similar proteins within a complex sample matrix.

The second aim is to improve detection sensitivity beyond the inherent limitations of conventional capillary-driven LFIA formats by introducing a magnetic bead (MB)-based Beads-on-a-Tip sandwich immunoassay. By enabling target enrichment and active washing prior to signal readout, this platform addresses sensitivity and background-related constraints at the assay format level.

Reference

(1) Morris, R.; Black, Katrina A.; Stollar, Elliott J. Uncovering protein function: from classification to complexes. *Essays in Biochemistry* **2022**, *66* (3), 255–285. DOI: 10.1042/ebc20200108 (accessed 6/10/2025).
(2) Kulkarni, P.; Porter, L.; Chou, T.-F.; Chong, S.; Chiti, F.; Schafer, J. W.; Mohanty, A.; Ramisetty, S.; Onuchic, J. N.; Tuite, M.; et al. Evolving concepts of the protein universe. *iScience* **2025**, *28* (3), 112012. DOI: https://doi.org/10.1016/j.isci.2025.112012.
(3) Rifai, N.; Gillette, M. A.; Carr, S. A. Protein biomarker discovery and validation: the long and uncertain path to clinical utility. *Nature Biotechnology* **2006**, *24* (8), 971–983. DOI: 10.1038/nbt1235.
(4) Anderson, N. L.; Anderson, N. G. The human plasma proteome: history, character, and diagnostic prospects. *Mol Cell Proteomics* **2002**, *1* (11), 845–867. DOI: 10.1074/mcp.r200007-mcp200 From NLM.
(5) Sproston, N. R.; Ashworth, J. J. Role of C-Reactive Protein at Sites of Inflammation and Infection. *Front Immunol* **2018**, *9*, 754. DOI: 10.3389/fimmu.2018.00754 From NLM.
(6) Passaro, A.; Al Bakir, M.; Hamilton, E. G.; Diehn, M.; André, F.; Roy-Chowdhuri, S.; Mountzios, G.; Wistuba, II; Swanton, C.; Peters, S. Cancer biomarkers: Emerging trends and clinical implications for personalized treatment. *Cell* **2024**, *187* (7), 1617–1635. DOI: 10.1016/j.cell.2024.02.041 From NLM.
(7) Gerszten, R. E.; Wang, T. J. The search for new cardiovascular biomarkers. *Nature* **2008**, *451* (7181), 949–952. DOI: 10.1038/nature06802.
(8) Cummings, J.; Ward, T. H.; Dive, C. Fit-for-purpose biomarker method validation in anticancer drug development. *Drug Discovery Today* **2010**, *15* (19), 816–825. DOI: https://doi.org/10.1016/j.drudis.2010.07.006.
(9) Yu, W.; Freeland, D. M. H.; Nadeau, K. C. Food allergy: immune mechanisms, diagnosis and immunotherapy. *Nat Rev Immunol* **2016**, *16* (12), 751–765. DOI: 10.1038/nri.2016.111 From NLM.

(10) Alshannaq, A.; Yu, J. H. Occurrence, Toxicity, and Analysis of Major Mycotoxins in Food. *Int J Environ Res Public Health* **2017**, *14* (6). DOI: 10.3390/ijerph14060632 From NLM.
(11) Jadhav, S. R.; Shah, R. M.; Karpe, A. V.; Morrison, P. D.; Kouremenos, K.; Beale, D. J.; Palombo, E. A. Detection of Foodborne Pathogens Using Proteomics and Metabolomics-Based Approaches. *Frontiers in Microbiology* **2018**, *Volume 9 - 2018*, Original Research. DOI: 10.3389/fmicb.2018.03132.
(12) Hafiz, A. H.; Jun, Z.; Yu-shuang, G. U. O.; Mei-xu, G. A. O.; Wei, G. U. O. Proteomic analysis of pathogen-responsive proteins from maize stem apoplast triggered by Fusarium verticillioides. *Journal of Integrative Agriculture* **2022**, *21* (2), 446–459. DOI: https://doi.org/10.1016/S2095-3119(21)63657-2.
(13) Roberta, A.; Massimo, L.; Pietro, F.; Candida, V.; Milena, M.; Ulisse, C.; Marcella, B.; Sergio, S.; Sandra, C. Thiol-peptide level and proteomic changes in response to cadmium toxicity in Oryza sativa L. roots. *Environmental and Experimental Botany* **2007**, *59* (3), 381–392. DOI: https://doi.org/10.1016/j.envexpbot.2006.04.010.
(14) Zulfqar ul, H.; Afnan, S.; Azmat Alam, K.; Mashooq Ahmad, D.; Abdul Majeed, G.; Yasir Afzal, B.; Heena, H.; Syed Mudasir, A. Nutrigenomics in livestock sector and its human-animal interface-a review. *Veterinary and Animal Science* **2022**, *17*, 100262. DOI: https://doi.org/10.1016/j.vas.2022.100262.
(15) Papakonstantinou, G. I.; Voulgarakis, N.; Terzidou, G.; Fotos, L.; Giamouri, E.; Papatsiros, V. G. Precision Livestock Farming Technology: Applications and Challenges of Animal Welfare and Climate Change. *Agriculture* **2024**, *14* (4), 620.
(16) Luhur Akbar, D.; Mohan, A.; Luyao, W.; Takehito, I.; Daisuke, S. Identification of protein biomarkers in wastewater linked to the incidence of COVID-19. *Science of The Total Environment* **2024**, *951*, 175649. DOI: https://doi.org/10.1016/j.scitotenv.2024.175649.
(17) Daunoras, J.; Kačergius, A.; Gudiukaitė, R. Role of Soil Microbiota Enzymes in Soil Health and Activity Changes Depending on Climate Change and the Type of Soil Ecosystem. *Biology* **2024**, *13* (2), 85.
(18) Richard, G. B.; Jared, L. D.; Jürgen, M.; Robert, L. S.; Mary, E. S.; Matthew, D. W.; Michael, N. W.; Annamaria, Z. Soil enzymes in a changing environment: Current knowledge and future directions. *Soil Biology and Biochemistry* **2013**, *58*, 216–234. DOI: https://doi.org/10.1016/j.soilbio.2012.11.009.
(19) Sapan, C. V.; Lundblad, R. L.; Price, N. C. Colorimetric protein assay techniques. *Biotechnology and Applied Biochemistry* **1999**, *29* (2), 99–108. DOI: https://doi.org/10.1111/j.1470-8744.1999.tb00538.x.
(20) Chutipongtanate, S.; Watcharatanyatip, K.; Homvises, T.; Jaturongkakul, K.; Thongboonkerd, V. Systematic comparisons of various spectrophotometric and colorimetric methods to measure concentrations of protein, peptide and amino acid: Detectable limits, linear dynamic ranges, interferences, practicality and unit costs. *Talanta* **2012**, *98*, 123–129. DOI: https://doi.org/10.1016/j.talanta.2012.06.058.
(21) *SDS-PAGE and Western Blotting: Basic Principles and Protocol , bookTitle= Protocols for the Diagnosis of Pig Viral Diseases*; Springer US, 2022. DOI: 10.1007/978-1-0716-2043-4_23.
(22) Alonso Villela, S. M.; Kraïem, H.; Bouhaouala-Zahar, B.; Bideaux, C.; Aceves Lara, C. A.; Fillaudeau, L. A protocol for recombinant protein quantification by densitometry. *Microbiologyopen* **2020**, *9* (6), 1175–1182. DOI: 10.1002/mbo3.1027 From NLM.
(23) Aydin, S.; Emre, E.; Ugur, K.; Aydin, M. A.; Sahin, İ.; Cinar, V.; Akbulut, T. An overview of ELISA: a review and update on best laboratory practices for quantifying

peptides and proteins in biological fluids. *Journal of International Medical Research* **2025**, *53* (2), 03000605251315913. DOI: 10.1177/03000605251315913.
(24) Hayrapetyan, H.; Tran, T.; Tellez-Corrales, E.; Madiraju, C. Enzyme-Linked Immunosorbent Assay: Types and Applications. *Methods Mol Biol* **2023**, *2612*, 1–17. DOI: 10.1007/978-1-0716-2903-1_1 From NLM.
(25) Shuken, S. R. An Introduction to Mass Spectrometry-Based Proteomics. *Journal of Proteome Research* **2023**, *22* (7), 2151–2171. DOI: 10.1021/acs.jproteome.2c00838.
(26) Han, X.; Aslanian, A.; Yates, J. R., 3rd. Mass spectrometry for proteomics. *Curr Opin Chem Biol* **2008**, *12* (5), 483–490. DOI: 10.1016/j.cbpa.2008.07.024 From NLM.
(27) Ahmed, R. High-Performance Liquid Chromatography (HPLC): Principles, Applications, Versatality, Efficiency, Innovation and Comparative Analysis in Modern Analytical Chemistry and In Pharmaceutical Sciences. **2024**.
(28) Aborode, A. T.; Adesola, R. O.; Scott, G. Y.; Arthur-Hayford, E.; Otorkpa, O. J.; Kwaku, S. D.; Elebesunu, E. E.; Nibokun, E. O.; Aruorivwooghene, I. J.; Bakre, A. A.; et al. Bringing lab to the field: Exploring innovations in point-of-care diagnostics for the rapid detection and management of tropical diseases in resource-limited settings. *Advances in Biomarker Sciences and Technology* **2025**, *7*, 28–43. DOI: https://doi.org/10.1016/j.abst.2025.01.001.
(29) Organization, W. H. *Laboratory and point-of-care diagnostic testing for sexually transmitted infections, including HIV*. 2023. (accessed).
(30) Qin, D.; Xia, Y.; Rogers, J. A.; Jackman, R. J.; Zhao, X.-M.; Whitesides, G. M. Microfabrication, Microstructures and Microsystems. In *Microsystem Technology in Chemistry and Life Science*, Manz, A., Becker, H. Eds.; Springer Berlin Heidelberg, 1998; pp 1–20.
(31) Siavashy, S.; Soltani, M.; Rahimi, S.; Hosseinali, M.; Guilandokht, Z.; Raahemifar, K. Recent advancements in microfluidic-based biosensors for detection of genes and proteins: Applications and techniques. *Biosensors and Bioelectronics: X* **2024**, *19*, 100489. DOI: https://doi.org/10.1016/j.biosx.2024.100489.
(32) Panda, S.; Pyarajan, S. Lab-on-Chip Devices for Protein Analysis. In *Encyclopedia of Microfluidics and Nanofluidics*, Li, D. Ed.; Springer US, 2008; pp 940–947.
(33) Zhang, H.; Zhao, L.; Brodský, J.; Migliaccio, L.; Gablech, I.; Neužil, P.; You, M. Proteomics-on-a-Chip – Microfluidics meets proteomics. *Biosensors and Bioelectronics* **2025**, *273*, 117122. DOI: https://doi.org/10.1016/j.bios.2024.117122.
(34) Cohen, L.; Keegan, A.; Walt, D. R. Single-Molecule Arrays for Ultrasensitive Detection of Blood-Based Biomarkers for Immunotherapy. *Methods Mol Biol* **2020**, *2055*, 399–412. DOI: 10.1007/978-1-4939-9773-2_18 From NLM.
(35) Tang, M. Y. H.; Shum, H. C. One-step immunoassay of C-reactive protein using droplet microfluidics. *Lab on a Chip* **2016**, *16* (22), 4359–4365, 10.1039/C6LC01121G. DOI: 10.1039/C6LC01121G.
(36) Jarić, S.; Schobesberger, S.; Velicki, L.; Milovančev, A.; Nikolić, S.; Ertl, P.; Bobrinetskiy, I.; Knežević, N. Ž. Direct electrochemical reduction of graphene oxide thin film for aptamer-based selective and highly sensitive detection of matrix metalloproteinase 2. *Talanta* **2024**, *274*, 126079. DOI: https://doi.org/10.1016/j.talanta.2024.126079.
(37) Akgönüllü, S.; Kılıç, S.; Esen, C.; Denizli, A. Molecularly Imprinted Polymer-Based Sensors for Protein Detection. *Polymers* **2023**, *15* (3), 629.
(38) Afsahi, S.; Lerner, M. B.; Goldstein, J. M.; Lee, J.; Tang, X.; Bagarozzi, D. A.; Pan, D.; Locascio, L.; Walker, A.; Barron, F.; et al. Novel graphene-based biosensor for

early detection of Zika virus infection. *Biosensors and Bioelectronics* **2018**, *100*, 85–88. DOI: https://doi.org/10.1016/j.bios.2017.08.051.
(39) Yetisen, A. K.; Akram, M. S.; Lowe, C. R. Paper-based microfluidic point-of-care diagnostic devices. *Lab on a Chip* **2013**, *13* (12), 2210–2251, 10.1039/C3LC50169H. DOI: 10.1039/C3LC50169H.
(40) Parolo, C.; Merkoçi, A. Paper-based nanobiosensors for diagnostics. *Chemical Society Reviews* **2013**, *42* (2), 450–457, 10.1039/C2CS35255A. DOI: 10.1039/C2CS35255A.
(41) Pilecky, M.; Harm, S.; Bauer, C.; Zottl, J.; Emprechtinger, R.; Eichhorn, T.; Schildböck, C.; Ecker, M.; Willheim, M.; Weber, V.; et al. Performance of lateral flow assays for SARS-CoV-2 compared to RT-qPCR. *J Infect* **2022**, *84* (4), 579–613. DOI: 10.1016/j.jinf.2022.01.013 From NLM.
(42) He, H.; Liu, B.; Wen, S.; Liao, J.; Lin, G.; Zhou, J.; Jin, D. Quantitative Lateral Flow Strip Sensor Using Highly Doped Upconversion Nanoparticles. *Analytical Chemistry* **2018**, *90* (21), 12356–12360. DOI: 10.1021/acs.analchem.8b04330.
(43) Jiao, X.; Peng, T.; Liang, Z.; Hu, Y.; Meng, B.; Zhao, Y.; Xie, J.; Gong, X.; Jiang, Y.; Fang, X.; et al. Lateral Flow Immunoassay Based on Time-Resolved Fluorescence Microspheres for Rapid and Quantitative Screening CA199 in Human Serum. *International Journal of Molecular Sciences* **2022**, *23* (17), 9991.
(44) Salminen, T.; Mehdi, F.; Rohila, D.; Kumar, M.; Talha, S. M.; Prakash, J. A. J.; Khanna, N.; Pettersson, K.; Batra, G. Ultrasensitive and Robust Point-of-Care Immunoassay for the Detection of Plasmodium falciparum Malaria. *Analytical Chemistry* **2020**, *92* (24), 15766–15772. DOI: 10.1021/acs.analchem.0c02748.
(45) Tsai, T. T.; Huang, T. H.; Ho, N. Y.; Chen, Y. P.; Chen, C. A.; Chen, C. F. Development of a multiplex and sensitive lateral flow immunoassay for the diagnosis of periprosthetic joint infection. *Sci Rep* **2019**, *9* (1), 15679. DOI: 10.1038/s41598-019-52051-6 From NLM.
(46) Khelifa, L.; Hu, Y.; Jiang, N.; Yetisen, A. K. Lateral flow assays for hormone detection. *Lab on a Chip* **2022**, *22* (13), 2451–2475, 10.1039/D1LC00960E. DOI: 10.1039/D1LC00960E.
(47) Guliy, O. I.; Dykman, L. A. Gold nanoparticle–based lateral-flow immunochromatographic biosensing assays for the diagnosis of infections. *Biosensors and Bioelectronics: X* **2024**, *17*, 100457. DOI: https://doi.org/10.1016/j.biosx.2024.100457.
(48) Rodríguez, M.; Blanco-Covián, L.; Costa-García, A.; Blanco-López, M. C. Silver and Gold enhancement methods for lateral flow immunoassays. *Talanta* **2015**, *148*. DOI: 10.1016/j.talanta.2015.10.068.
(49) Li, Y.; Chen, C.; Liu, F.; Liu, J. Engineered lanthanide-doped upconversion nanoparticles for biosensing and bioimaging application. *Microchimica Acta* **2022**, *189* (3), 109. DOI: 10.1007/s00604-022-05180-1.
(50) Liu, Q.; Cheng, S.; Chen, R.; Ke, J.; Liu, Y.; Li, Y.; Feng, W.; Li, F. Near-Infrared Lanthanide-Doped Nanoparticles for a Low Interference Lateral Flow Immunoassay Test. *ACS Applied Materials & Interfaces* **2020**, *12* (4), 4358–4365. DOI: 10.1021/acsami.9b22449.
(51) Ahmad Najib, M.; Selvam, K.; Khalid, M. F.; Ozsoz, M.; Aziah, I. Quantum Dot-Based Lateral Flow Immunoassay as Point-of-Care Testing for Infectious Diseases: A Narrative Review of Its Principle and Performance. *Diagnostics (Basel)* **2022**, *12* (9). DOI: 10.3390/diagnostics12092158 From NLM.
(52) Fang, B.; Xiong, Q.; Duan, H.; Xiong, Y.; Lai, W. Tailored quantum dots for enhancing sensing performance of lateral flow immunoassay. *TrAC Trends in*

Analytical Chemistry **2022**, *157*, 116754. DOI: https://doi.org/10.1016/j.trac.2022.116754.
(53) Yang, M.; Xu, X.; Zhang, M.; Wang, J.; Wu, Y.; Wang, N.; Li, Z. Recent advances in lateral flow immunoassay based on sandwich format for whole-cell pathogen detection. *Coordination Chemistry Reviews* **2025**, *533*, 216538. DOI: https://doi.org/10.1016/j.ccr.2025.216538.
(54) Jin, Y.; Jung, J. H.; Han, W. K.; Hwang, E. C.; Nho, Y.; Lee, N.; Yun, J. E.; Lee, K. S.; Lee, S. H.; Lee, H.; et al. Diagnostic accuracy of prostate-specific antigen below 4 ng/mL as a cutoff for diagnosing prostate cancer in a hospital setting: A systematic review and meta-analysis. *Investig Clin Urol* **2022**, *63* (3), 251–261. DOI: 10.4111/icu.20210429 From NLM.
(55) Shin, M.; Kim, W.; Yoo, K.; Cho, H.-S.; Jang, S.; Bae, H.-J.; An, J.; Lee, J.-c.; Chang, H.; Kim, D.-E.; et al. Highly sensitive multiplexed colorimetric lateral flow immunoassay by plasmon-controlled metal–silica isoform nanocomposites: PINs. *Nano Convergence* **2024**, *11* (1), 42. DOI: 10.1186/s40580-024-00449-y.
(56) Cai, Y.; Zhang, S.; Dong, C.; Yang, J.; Ma, T.; Zhang, H.; Cui, Y.; Hui, W. Lateral flow immunoassay based on gold magnetic nanoparticles for the protein quantitative detection: Prostate-specific antigen. *Anal Biochem* **2021**, *627*, 114265. DOI: 10.1016/j.ab.2021.114265 From NLM.
(57) Miglione, A.; Di Nardo, F.; Cavalera, S.; Serra, T.; Baggiani, C.; Cinti, S.; Anfossi, L. Merging Lateral Flow Immunoassay with Electroanalysis as a Novel Sensing Platform: Prostate Specific Antigen Detection as Case of Study. *Analytical Chemistry* **2024**, *96* (6), 2297–2302. DOI: 10.1021/acs.analchem.3c04078.
(58) Kim, H.-M.; Kim, J.; Bock, S.; An, J.; Choi, Y.-S.; Pham, X.-H.; Cha, M. G.; Seong, B.; Kim, W.; Kim, Y.-H.; et al. Silver-Assembled Silica Nanoparticles in Lateral Flow Immunoassay for Visual Inspection of Prostate-Specific Antigen. *Sensors* **2021**, *21* (12), 4099.
(59) Bock, S.; Kim, H. M.; Kim, J.; An, J.; Choi, Y. S.; Pham, X. H.; Jo, A.; Ham, K. M.; Song, H.; Kim, J. W.; et al. Lateral Flow Immunoassay with Quantum-Dot-Embedded Silica Nanoparticles for Prostate-Specific Antigen Detection. *Nanomaterials (Basel)* **2021**, *12* (1). DOI: 10.3390/nano12010033 From NLM.
(60) Bock, S.; An, J.; Kim, H.-M.; Kim, J.; Jung, H.-s.; Pham, X.-H.; Rho, W.; Jun, B.-H. A Lateral Flow Immunoassay for Prostate‐Specific Antigen Detection Using Silica‐Coated CdSe@ZnS Quantum Dots. *Bulletin of the Korean Chemical Society* **2020**, *41*, 989. DOI: 10.1002/bkcs.12099.
(61) Rodríguez, M. O.; Covián, L. B.; García, A. C.; Blanco-López, M. C. Silver and gold enhancement methods for lateral flow immunoassays. *Talanta* **2016**, *148*, 272–278. DOI: https://doi.org/10.1016/j.talanta.2015.10.068.
(62) Oh, H. K.; Kim, K.; Park, J.; Im, H.; Maher, S.; Kim, M. G. Plasmon color-preserved gold nanoparticle clusters for high sensitivity detection of SARS-CoV-2 based on lateral flow immunoassay. *Biosens Bioelectron* **2022**, *205*, 114094. DOI: 10.1016/j.bios.2022.114094 From NLM.
(63) Lee, A. S.; Kim, S. M.; Kim, K. R.; Park, C.; Lee, D.-G.; Heo, H. R.; Cha, H. J.; Kim, C. S. A colorimetric lateral flow immunoassay based on oriented antibody immobilization for sensitive detection of SARS-CoV-2. *Sensors and Actuators B: Chemical* **2023**, *379*, 133245. DOI: https://doi.org/10.1016/j.snb.2022.133245.
(64) Wang, K.; Liu, X.; Liang, X.; Jiang, Y.; Wen, C.-Y.; Zeng, J. Near-Infrared Responsive Ag@Au Nanoplates with Exceptional Stability for Highly Sensitive Colorimetric and Photothermal Dual-Mode Lateral Flow Immunoassay. *Analytical Chemistry* **2024**, *96* (7), 3208–3216. DOI: 10.1021/acs.analchem.3c05787.

(65) Chen, Z.; Zhang, Z.; Zhai, X.; Li, Y.; Lin, L.; Zhao, H.; Bian, L.; Li, P.; Yu, L.; Wu, Y.; et al. Rapid and Sensitive Detection of anti-SARS-CoV-2 IgG, Using Lanthanide-Doped Nanoparticles-Based Lateral Flow Immunoassay. *Analytical Chemistry* **2020**, *92* (10), 7226–7231. DOI: 10.1021/acs.analchem.0c00784.
(66) Chen, W.; Chen, H.; Liu, Y.; Wei, H.; Wang, Y.; Rong, Z.; Liu, X. An integrated fluorescent lateral flow assay for multiplex point-of-care detection of four respiratory viruses. *Anal Biochem* **2022**, *659*, 114948. DOI: 10.1016/j.ab.2022.114948 From NLM.
(67) Li, H.; Liu, H.; Wong, K.-L.; All, A. H. Lanthanide-doped upconversion nanoparticles as nanoprobes for bioimaging. *Biomaterials Science* **2024**, *12* (18), 4650–4663, 10.1039/D4BM00774C. DOI: 10.1039/D4BM00774C.
(68) Luo, R.; Zhang, C.; Zhang, Z.; Ren, P.; Xu, Z.; Liu, Y. NIR-II upconversion nanomaterials for biomedical applications. *Nanoscale* **2025**, *17* (6), 2985–3002, 10.1039/D4NR04445B. DOI: 10.1039/D4NR04445B.
(69) Wang, F.; Banerjee, D.; Liu, Y.; Chen, X.; Liu, X. Upconversion nanoparticles in biological labeling, imaging, and therapy. *Analyst* **2010**, *135* (8), 1839–1854, 10.1039/C0AN00144A. DOI: 10.1039/C0AN00144A.
(70) Zhou, J.; Liu, Z.; Li, F. Upconversion nanophosphors for small-animal imaging. *Chemical Society Reviews* **2012**, *41* (3), 1323–1349, 10.1039/C1CS15187H. DOI: 10.1039/C1CS15187H.
(71) Chatterjee, D. K.; Gnanasammandhan, M. K.; Zhang, Y. Small Upconverting Fluorescent Nanoparticles for Biomedical Applications. *Small* **2010**, *6* (24), 2781–2795. DOI: https://doi.org/10.1002/smll.201000418.
(72) Lamon, S.; Yu, H.; Zhang, Q.; Gu, M. Lanthanide ion-doped upconversion nanoparticles for low-energy super-resolution applications. *Light: Science & Applications* **2024**, *13* (1), 252. DOI: 10.1038/s41377-024-01547-6.
(73) Wang, F.; Liu, X. Upconversion Multicolor Fine-Tuning: Visible to Near-Infrared Emission from Lanthanide-Doped NaYF4 Nanoparticles. *Journal of the American Chemical Society* **2008**, *130* (17), 5642–5643. DOI: 10.1021/ja800868a.
(74) Wen, S.; Zhou, J.; Zheng, K.; Bednarkiewicz, A.; Liu, X.; Jin, D. Advances in highly doped upconversion nanoparticles. *Nature Communications* **2018**, *9* (1), 2415. DOI: 10.1038/s41467-018-04813-5.
(75) Máčala, J.; Makhneva, E.; Hlaváček, A.; Kopecký, M.; Gorris, H. H.; Skládal, P.; Farka, Z. Upconversion Nanoparticle-Based Dot-Blot Immunoassay for Quantitative Biomarker Detection. *Analytical Chemistry* **2024**, *96* (25), 10237–10245. DOI: 10.1021/acs.analchem.4c00837.
(76) Zhang, S.; Sun, Y.; Sun, Y.; Wang, H.; Shen, Y. Semiquantitative immunochromatographic colorimetric biosensor for the detection of dexamethasone based on up-conversion fluorescent nanoparticles. *Microchimica Acta* **2020**, *187*. DOI: 10.1007/s00604-020-04418-0.
(77) You, M.; Lin, M.; Gong, Y.; Wang, S.; Li, A.; Ji, L.; Zhao, H.; Ling, K.; Wen, T.; Huang, Y.; et al. Household Fluorescent Lateral Flow Strip Platform for Sensitive and Quantitative Prognosis of Heart Failure Using Dual-Color Upconversion Nanoparticles. *ACS Nano* **2017**, *11* (6), 6261–6270. DOI: 10.1021/acsnano.7b02466.
(78) Chen, Y.; Shen, Y.; Wang, H.; Zhang, J.; Zhu, J. A novel dual-channel immunochromatographic strip using up-conversion nanoparticles for simultaneous detection of AFB1 and ZEN in maize. *Anal Bioanal Chem* **2023**, *415* (20), 4935–4947. DOI: 10.1007/s00216-023-04799-0 From NLM.
(79) Guo, J.; Chen, S.; Tian, S.; Liu, K.; Ma, X.; Guo, J. A sensitive and quantitative prognosis of C-reactive protein at picogram level using mesoporous silica

encapsulated core-shell up-conversion nanoparticle based lateral flow strip assay. *Talanta* **2021**, *230*, 122335. DOI: 10.1016/j.talanta.2021.122335 From NLM.
(80) Zhao, J.; Jin, D.; Schartner, E. P.; Lu, Y.; Liu, Y.; Zvyagin, A. V.; Zhang, L.; Dawes, J. M.; Xi, P.; Piper, J. A.; et al. Single-nanocrystal sensitivity achieved by enhanced upconversion luminescence. *Nature Nanotechnology* **2013**, *8* (10), 729–734. DOI: 10.1038/nnano.2013.171.
(81) Gargas, D. J.; Chan, E. M.; Ostrowski, A. D.; Aloni, S.; Altoe, M. V. P.; Barnard, E. S.; Sanii, B.; Urban, J. J.; Milliron, D. J.; Cohen, B. E.; et al. Engineering bright sub-10-nm upconverting nanocrystals for single-molecule imaging. *Nature Nanotechnology* **2014**, *9* (4), 300–305. DOI: 10.1038/nnano.2014.29.
(82) Zhang, L.; Wen, S.; Khan, J. U.; Liu, Y.; Maddahfar, M.; Zhou, J.; Jin, D. Ultrasensitive Rapid Antigen Test by Geometric Lateral Flow Assays and Highly Doped Upconversion Nanoparticles. *Anal Chem* **2024**, *96* (42), 16581–16589. DOI: 10.1021/acs.analchem.4c02379 From NLM.
(83) Masoumeh Ghorbanpour, S.; Wen, S.; Kaitu'u-Lino, T. J.; Hannan, N. J.; Jin, D.; McClements, L. Quantitative Point of Care Tests for Timely Diagnosis of Early-Onset Preeclampsia with High Sensitivity and Specificity. *Angew Chem Int Ed Engl* **2023**, *62* (26), e202301193. DOI: 10.1002/anie.202301193 From NLM.
(84) Chen, G.; Qiu, H.; Prasad, P. N.; Chen, X. Upconversion Nanoparticles: Design, Nanochemistry, and Applications in Theranostics. *Chemical Reviews* **2014**, *114* (10), 5161–5214. DOI: 10.1021/cr400425h.
(85) Haase, M.; Schäfer, H. Upconverting Nanoparticles. *Angewandte Chemie International Edition* **2011**, *50* (26), 5808–5829. DOI: https://doi.org/10.1002/anie.201005159.
(86) Lu, C.; Ouyang, J.; Zhang, J. Core–shell upconversion nanoparticles with suitable surface modification to overcome endothelial barrier. *Discover Nano* **2024**, *19* (1), 181. DOI: 10.1186/s11671-024-04139-w.
(87) Hoover, E. C.; Roy Chowdhury, C.; Ruggiero, O. M.; Day, E. S. Conjugation of Antibodies and siRNA Duplexes to Polymer Nanoparticles via Maleimide–Thiol Chemistry. *ACS Omega* **2024**, *9* (48), 47637–47646. DOI: 10.1021/acsomega.4c07025.
(88) Hossain, M. K.; Hasan, M. M.; Islam, M. S.; Mefford, O. T.; Ahmad, H.; Rahman, M. M. Polypyrrole Coating via Lemieux-von Rudloff Oxidation on Magnetite Nanoparticles for Highly Efficient Removal of Chromium(VI) from Wastewater. *ACS Omega* **2024**, *9* (17), 19077–19088. DOI: 10.1021/acsomega.3c09864.
(89) Skrotzki, E. A.; Vandavasi, J. K.; Newman, S. G. Ozone-Mediated Amine Oxidation and Beyond: A Solvent-Free, Flow-Chemistry Approach. *The Journal of Organic Chemistry* **2021**, *86* (20), 14169–14176. DOI: 10.1021/acs.joc.1c00768.
(90) Swinburne, A. N.; Langford Paden, M. H.; Chan, T. L.; Randall, S.; Ortu, F.; Kenwright, A. M.; Natrajan, L. S. Optical Properties of Heavily Fluorinated Lanthanide Tris β-Diketonate Phosphine Oxide Adducts. *Inorganics* **2016**, *4* (3), 27.
(91) Yuan, J.; Cen, Y.; Kong, X.-J.; Wu, S.; Liu, C.-L.; Yu, R.-Q.; Chu, X. MnO2-Nanosheet-Modified Upconversion Nanosystem for Sensitive Turn-On Fluorescence Detection of H2O2 and Glucose in Blood. *ACS Applied Materials & Interfaces* **2015**, *7* (19), 10548–10555. DOI: 10.1021/acsami.5b02188.
(92) Zhou, H.-P.; Xu, C.-H.; Sun, W.; Yan, C.-H. Clean and Flexible Modification Strategy for Carboxyl/Aldehyde-Functionalized Upconversion Nanoparticles and Their Optical Applications. *Advanced Functional Materials* **2009**, *19* (24), 3892–3900. DOI: https://doi.org/10.1002/adfm.200901458.

(93) Wu, Y.; Li, D.; Zhou, F.; Liang, H.; Liu, Y.; Hou, W.; Yuan, Q.; Zhang, X.; Tan, W. Versatile in situ synthesis of MnO2 nanolayers on upconversion nanoparticles and their application in activatable fluorescence and MRI imaging. *Chemical Science* **2018**, *9* (24), 5427–5434, 10.1039/C8SC00490K. DOI: 10.1039/C8SC00490K.
(94) Coffaro, B.; Weisel, C. P. Reactions and Products of Squalene and Ozone: A Review. *Environmental Science & Technology* **2022**, *56* (12), 7396–7411. DOI: 10.1021/acs.est.1c07611.
(95) Sun, C.; Gradzielski, M. Advances in fluorescence sensing enabled by lanthanide-doped upconversion nanophosphors. *Advances in Colloid and Interface Science* **2022**, *300*, 102579. DOI: https://doi.org/10.1016/j.cis.2021.102579.
(96) Wang, G.; Peng, Q.; Li, Y. Upconversion Luminescence of Monodisperse CaF2:Yb3+/Er3+ Nanocrystals. *Journal of the American Chemical Society* **2009**, *131* (40), 14200–14201. DOI: 10.1021/ja906732y.
(97) Bogdan, N.; Vetrone, F.; Ozin, G. A.; Capobianco, J. A. Synthesis of Ligand-Free Colloidally Stable Water Dispersible Brightly Luminescent Lanthanide-Doped Upconverting Nanoparticles. *Nano Letters* **2011**, *11* (2), 835–840. DOI: 10.1021/nl1041929.
(98) Kong, W.; Sun, T.; Chen, B.; Chen, X.; Ai, F.; Zhu, X.; Li, M.; Zhang, W.; Zhu, G.; Wang, F. A General Strategy for Ligand Exchange on Upconversion Nanoparticles. *Inorganic Chemistry* **2017**, *56* (2), 872–877. DOI: 10.1021/acs.inorgchem.6b02479.
(99) Himmelstoß, S. F.; Hirsch, T. Long-Term Colloidal and Chemical Stability in Aqueous Media of NaYF4-Type Upconversion Nanoparticles Modified by Ligand-Exchange. *Particle & Particle Systems Characterization* **2019**, *36* (10), 1900235. DOI: https://doi.org/10.1002/ppsc.201900235.
(100) Jurga, N.; Przybylska, D.; Kamiński, P.; Grzyb, T. Improvement of ligand-free modification strategy to obtain water-stable up-converting nanoparticles with bright emission and high reaction yield. *Scientific Reports* **2021**, *11* (1), 18846. DOI: 10.1038/s41598-021-98240-0.
(101) Alzahrani, Y. A.; Alessa, A. M.; Almosaind, M. K.; Alarifi, R. S.; Alromaeh, A.; Alkahtani, M. Preparation and Characterization of Uniform and Controlled Silica Encapsulating on Lithium Yttrium Fluoride-Based Upconversion Nanoparticles. *Nanomaterials* **2024**, *14* (8), 685.
(102) Chen, D.; Lei, L.; Yang, A.; Wang, Z.; Wang, Y. Ultra-broadband near-infrared excitable upconversion core/shell nanocrystals. *Chemical Communications* **2012**, *48* (47), 5898–5900, 10.1039/C2CC32102E. DOI: 10.1039/C2CC32102E.
(103) Kembuan, C.; Saleh, M.; Rühle, B.; Resch-Genger, U.; Graf, C. Coating of upconversion nanoparticles with silica nanoshells of 5-250 nm thickness. *Beilstein J Nanotechnol* **2019**, *10*, 2410–2421. DOI: 10.3762/bjnano.10.231 From NLM.
(104) Morel, A.-L.; Nikitenko, S. I.; Gionnet, K.; Wattiaux, A.; Lai-Kee-Him, J.; Labrugere, C.; Chevalier, B.; Deleris, G.; Petibois, C.; Brisson, A.; et al. Sonochemical Approach to the Synthesis of Fe3O4@SiO2 Core−Shell Nanoparticles with Tunable Properties. *ACS Nano* **2008**, *2* (5), 847–856. DOI: 10.1021/nn800091q.
(105) Stöber, W.; Fink, A.; Bohn, E. Controlled growth of monodisperse silica spheres in the micron size range. *Journal of Colloid and Interface Science* **1968**, *26* (1), 62–69. DOI: https://doi.org/10.1016/0021-9797(68)90272-5.
(106) Ureña-Horno, E.; Kyriazi, M.-E.; Kanaras, A. G. A method for the growth of uniform silica shells on different size and morphology upconversion nanoparticles. *Nanoscale Advances* **2021**, *3* (12), 3522–3529, 10.1039/D0NA00858C. DOI: 10.1039/D0NA00858C.

(107) Uskoković, V.; Drofenik, M. Reverse micelles: Inert nano-reactors or physico-chemically active guides of the capped reactions. *Advances in Colloid and Interface Science* **2007**, *133* (1), 23–34. DOI: https://doi.org/10.1016/j.cis.2007.02.002.
(108) Darbandi, M.; Nann, T. One-pot synthesis of YF3@silica core/shell nanoparticles. *Chemical communications (Cambridge, England)* **2006**, 776–778. DOI: 10.1039/b516171a.
(109) Hlaváček, A.; Mickert, M. J.; Soukka, T.; Lahtinen, S.; Tallgren, T.; Pizúrová, N.; Król, A.; Gorris, H. H. Large-Scale Purification of Photon-Upconversion Nanoparticles by Gel Electrophoresis for Analogue and Digital Bioassays. *Analytical Chemistry* **2019**, *91* (2), 1241–1246. DOI: 10.1021/acs.analchem.8b04488.
(110) Sukhorukov, G. B.; Donath, E.; Lichtenfeld, H.; Knippel, E.; Knippel, M.; Budde, A.; Möhwald, H. Layer-by-layer self assembly of polyelectrolytes on colloidal particles. *Colloids and Surfaces A: Physicochemical and Engineering Aspects* **1998**, *137* (1), 253–266. DOI: https://doi.org/10.1016/S0927-7757(98)00213-1.
(111) He, L.; Feng, L.; Cheng, L.; Liu, Y.; Li, Z.; Peng, R.; Li, Y.; Guo, L.; Liu, Z. Multilayer Dual-Polymer-Coated Upconversion Nanoparticles for Multimodal Imaging and Serum-Enhanced Gene Delivery. *ACS Applied Materials & Interfaces* **2013**, *5* (20), 10381–10388. DOI: 10.1021/am403554x.
(112) Wang, L.; Yan, R.; Huo, Z.; Wang, L.; Zeng, J.; Bao, J.; Wang, X.; Peng, Q.; Li, Y. Fluorescence Resonant Energy Transfer Biosensor Based on Upconversion-Luminescent Nanoparticles. *Angewandte Chemie International Edition* **2005**, *44* (37), 6054–6057. DOI: https://doi.org/10.1002/anie.200501907.
(113) Juan, J.; Cheng, L.; Shi, M.; Liu, Z.; Mao, X. Poly-(allylamine hydrochloride)-coated but not poly(acrylic acid)-coated upconversion nanoparticles induce autophagy and apoptosis in human blood cancer cells. *Journal of Materials Chemistry B* **2015**, *3* (28), 5769–5776, 10.1039/C5TB00646E. DOI: 10.1039/C5TB00646E.
(114) Saleh, M. I.; Rühle, B.; Wang, S.; Radnik, J.; You, Y.; Resch-Genger, U. Assessing the protective effects of different surface coatings on NaYF4:Yb3+, Er3+ upconverting nanoparticles in buffer and DMEM. *Scientific Reports* **2020**, *10* (1), 19318. DOI: 10.1038/s41598-020-76116-z.
(115) Bastos, V.; Oskoei, P.; Andresen, E.; Saleh, M. I.; Rühle, B.; Resch-Genger, U.; Oliveira, H. Stability, dissolution, and cytotoxicity of NaYF(4)-upconversion nanoparticles with different coatings. *Sci Rep* **2022**, *12* (1), 3770. DOI: 10.1038/s41598-022-07630-5 From NLM.
(116) Zhang, Q.; Song, K.; Zhao, J.; Kong, X.; Sun, Y.; Liu, X.; Zhang, Y.; Zeng, Q.; Zhang, H. Hexanedioic acid mediated surface–ligand-exchange process for transferring NaYF4:Yb/Er (or Yb/Tm) up-converting nanoparticles from hydrophobic to hydrophilic. *Journal of Colloid and Interface Science* **2009**, *336* (1), 171–175. DOI: https://doi.org/10.1016/j.jcis.2009.04.024.
(117) Duong, H. T. T.; Chen, Y.; Tawfik, S. A.; Wen, S.; Parviz, M.; Shimoni, O.; Jin, D. Systematic investigation of functional ligands for colloidal stable upconversion nanoparticles. *RSC Advances* **2018**, *8* (9), 4842–4849, 10.1039/C7RA13765F. DOI: 10.1039/C7RA13765F.
(118) Zhang, H.; Wang, X.; Jin, R.; Su, Q. Preparation and applications of polymer-modified lanthanide-doped upconversion nanoparticles. *Giant* **2022**, *12*, 100130. DOI: https://doi.org/10.1016/j.giant.2022.100130.
(119) Zhang, H.; Li, Y.; Ivanov, I. A.; Qu, Y.; Huang, Y.; Duan, X. Plasmonic modulation of the upconversion fluorescence in NaYF4 :Yb/Tm hexaplate nanocrystals using gold nanoparticles or nanoshells. *Angew Chem Int Ed Engl* **2010**, *49* (16), 2865–2868. DOI: 10.1002/anie.200905805 From NLM.

(120) Adhikari, A.; Chen, I. A. Antibody-Nanoparticle Conjugates in Therapy: Combining the Best of Two Worlds. *Small* **2025**, *21* (15), 2409635. DOI: https://doi.org/10.1002/smll.202409635.
(121) Yan, Q.; Zheng, H.-N.; Jiang, C.; Li, K.; Xiao, S.-J. EDC/NHS activation mechanism of polymethacrylic acid: anhydride versus NHS-ester. *RSC Advances* **2015**, *5* (86), 69939–69947, 10.1039/C5RA13844B. DOI: 10.1039/C5RA13844B.
(122) Totaro, K. A.; Liao, X.; Bhattacharya, K.; Finneman, J. I.; Sperry, J. B.; Massa, M. A.; Thorn, J.; Ho, S. V.; Pentelute, B. L. Systematic Investigation of EDC/sNHS-Mediated Bioconjugation Reactions for Carboxylated Peptide Substrates. *Bioconjugate Chemistry* **2016**, *27* (4), 994–1004. DOI: 10.1021/acs.bioconjchem.6b00043.
(123) Singh, R.; Srinivas, S. P.; Kumawat, M.; Daima, H. K. Ligand-based surface engineering of nanomaterials: Trends, challenges, and biomedical perspectives. *OpenNano* **2024**, *15*, 100194. DOI: https://doi.org/10.1016/j.onano.2023.100194.
(124) Arruebo, M.; Valladares, M.; González-Fernández, Á. Antibody-Conjugated Nanoparticles for Biomedical Applications. *Journal of Nanomaterials* **2009**, *2009* (1), 439389. DOI: https://doi.org/10.1155/2009/439389.
(125) Koehler, K. C.; Alge, D. L.; Anseth, K. S.; Bowman, C. N. Development of a Maleimide Amino Acid for Use as a Tool for Peptide Conjugation and Modification. *International Journal of Peptide Research and Therapeutics* **2013**, *19* (3), 265–274. DOI: 10.1007/s10989-013-9347-y.
(126) Lee, N. K.; Wang, C.-P. J.; Lim, J.; Park, W.; Kwon, H.-K.; Kim, S.-N.; Kim, T.-H.; Park, C. G. Impact of the conjugation of antibodies to the surfaces of polymer nanoparticles on the immune cell targeting abilities. *Nano Convergence* **2021**, *8* (1), 24. DOI: 10.1186/s40580-021-00274-7.
(127) Maruani, A.; Smith, M. E. B.; Miranda, E.; Chester, K. A.; Chudasama, V.; Caddick, S. A plug-and-play approach to antibody-based therapeutics via a chemoselective dual click strategy. *Nature Communications* **2015**, *6* (1), 6645. DOI: 10.1038/ncomms7645.
(128) Forte, N.; Chudasama, V.; Baker, J. R. Homogeneous antibody-drug conjugates via site-selective disulfide bridging. *Drug Discov Today Technol* **2018**, *30*, 11–20. DOI: 10.1016/j.ddtec.2018.09.004 From NLM.

Chapter 2. Conjugates Development

Functionalization and bioconjugation of UCNPs are essential for enabling specific protein recognition in bioanalytical applications. In this work, conjugate development begins with the synthesis of β-NaYF4:Yb3+, Er3+ core nanoparticles via a coprecipitation approach, followed by epitaxial growth of an inert NaYF4 shell to enhance luminescence stability. To enable aqueous dispersion and subsequent bioconjugation, UCNP surfaces were modified using amphiphilic diblock polymers synthesized via RAFT polymerization and transferred into water through ligand exchange. The polymer-functionalized UCNPs were subsequently conjugated with antibodies using carbodiimide coupling chemistry. This chapter describes the synthesis, surface modification, and bioconjugation procedures that form the experimental basis for the nanoparticle-based assays developed in subsequent chapters.

2.1 UCNPs synthesis developed in this work

2.1.1 Synthesis of $NaYF_4$: Yb, Er core nanoparticles

Following a coprecipitation protocol adapted from previous work[1], the core nanoparticles (beta-$NaYF_4$:40% Yb^{3+},4% Er^{3+}) were synthesized 1.12 mmoL $YCl_3 \cdot 6H_2O$, 0.8 mmoL $YbCl_3 \cdot 6H_2O$ and 0.08 mmoL $ErCl_3 \cdot 6H_2O$ in methanol solution together with 12 mL oleic acidand 30 mL 1-octadecene were added to a 100 mL three-neck round-bottom flask under vigorous stirring. The resulting mixture was heated at 150 °C for 40 mins. Then the solution was cooled down to room temperature. A 10 mL methanol solution with 5 mmol NaOH and 8 mmoL NH_4F was added and stirred for 30 mins, and then the mixture was slowly heated to 150 °C and kept for 40 mins under argon flow to remove methanol and residual water. The solution was quickly heated at 300 °C under an argon flow for 75 mins. The final $NaYF_4$: Yb, Er nanoparticles were dispersed in cyclohexane after washing with cyclohexane and ethanol several times.

2.1.2 Synthesis of $NaYF_4$: Yb, Tm core nanoparticles

The core doped nanoparticles (beta-$NaYF_4$:40% Yb^{3+},4% Tm^{3+}) were synthesized with $YCl_3 \cdot 6H_2O$ (0.56 mmoL), $YbCl_3 \cdot 6H_2O$ (0.4 mmoL) and $TmCl_3 \cdot 6H_2O$ (0.04 mmoL) were added into a 50 mL three-necked flask containing 6mL oleic acid and 15 mL 1-

octadecene. The mixture was first heated to 170 °C under argon for 30 min to form a transparent solution and remove residual water. The solution was cooled down to room temperature, and 10 mL of a methanol solution containing NaOH (2.5 mmoL) and NH_4F (4 mmoL) was slowly dropped into the flask and stirred for 30 mins. Then, the solution was heated to 70-80 °C and maintained for 30 mins to evaporate methanol. Subsequently, the solution was heated to 300 °C and maintained for 1.5 hs under argon atmosphere. After cooling down to room temperature, the resulting products were precipitated by ethanol and collected by centrifugation at 3380 g for 5 mins. The final $NaYF_4$:Yb, Tm nanoparticles were dispersed in cyclohexane after washing with cyclohexane and ethanol several times.

2.1.3 Synthesis methods of shell precursor for core-shell spherical nanoparticles

The shell precursor was prepared for the epitaxial growth of shell onto the core nanoparticles through hot-injection method. The synthesis of shell precursor was similar to that of the core as described above. For the shell precursor, the final step was to cool down the solution to RT after removing residual methanol and water. The spherical nanoparticles in this chapter were coated with inert shell, therefore, the starting material of Ln^{3+} ion was 1 mmoL of $YCl_3 \cdot 6H_2O$.

2.1.4 Synthesis of $NaYF_4$:40%Yb^{3+},4%Er^{3+}/Tm^{3+} @$NaYF_4$ core@shell nanoparticles

The core@$NaYF_4$ core-inert shell spherical nanoparticles were synthesized by epitaxial shell growth method. Firstly, 0.2 mmoL of the as-synthesized core nanoparticles dissolved in cyclohexane was added to the flask with 6 mL of OA and 6 mL of ODE. The solution was sealed and degassed by inert gases and then heated to 80 °C to remove cyclohexane, with magnetic stir rotating at 800 rpm. After the complete removal of bubbles, the solution was further heated to 300 °C. The shell precursor in the 3 mL syringe with minimum scale of 0.1 mL was injected into the solution at the rate of 0.2 mL/3 min, during which the temperature was always maintained at 300 °C. The total amount of shell precursor was based on the size of the core and the desired size of the final core-shell. Once finishing the hot-injection cycles, the solution was further kept at 300 °C for 10 mins for complete nucleation then

cooled down to RT. The following washing protocol was the same as that of the core nanoparticles.

2.2 Polymer-based surface modification of UCNPs

The polymer-based ligand exchange strategy described in this section was used consistently throughout this thesis (Chapters 3,4 and 5), and a ligand-free surface modification approach was employed exclusively in Chapter 3 for comparative purposes. A ligand-exchange strategy was selected for UCNP surface modification due to its procedural simplicity, robustness, and ability to preserve colloidal stability in aqueous environment. Since surface ligands critically influence both the dispersibility and biocompatibility of nanoparticles, we utilized a poly(oligo(ethylene glycol) methacrylate) (POEGMA)-based polymer for surface modification. This polymer was chosen for its strong hydrophilicity and antifouling properties. The ligand exchange process was driven by the strong coordination affinity between the phosphate functional groups on the polymer and the lanthanide (Ln^{3+}) ions on the UCNP surface, enabling effective displacement of the native oleic acid ligands and rendering the nanoparticles water-dispersible and suitable for subsequent bioconjugation.

2.2.1 Polymer synthesis

The synthesis of Poly(oligo(ethylene glycol) methacrylate) (POEGMEA) followed the method described in our previously published paper[2]. Briefly, OEGMEA (5 g), Reversible addition−fragmentation chain transfer (RAFT) agent (113 mg), and recrystallized 2,2′-azobis(isobutyronitrile) (AIBN) (7.77 mg) were combined in a round-bottom flask containing 20 mL of toluene. The flask was equipped with a magnetic stirrer bar and purged with argon for 30 minutes. The reaction mixture was then heated in a preheated oil bath at 70°C to initiate the decomposition of the AIBN. To synthesize POEGMEA macroRAFT with 13 OEGMEA units, the polymerization was terminated after 4.5 hs by placing the reaction mixture in an ice bath for 5 mins. The synthesized POEGMEA was purified by washing three times with n-hexane, followed by centrifugation at 7600 g for 5 mins. The final samples were stored at 4 °C for subsequent chain extension to produce diblock copolymer. Then, POEGMA (1.4 M), AIBN (0.4×10^{-2} M), and Monoacryloxy ethyl phosphate (MAEP) (1.43×10^{-1} M) were

mixed with 5 mL of acetonitrile in a one-necked round-bottom flask equipped with a magnetic stirrer. The flask was sealed with a rubber septum and purged with argon gas for 30 mins. The mixture was then placed in a preheated oil bath at 70 °C for 17 hs. Polymerization was quenched using an ice bath upon achieving 70% MAEP monomer conversion. The monomer conversion measurement was conducted with HNMR. The final polymer with 13 OEGMEA units were dialyzed against methanol for 48 hs using a 3 kDa molecular weight cut-off membrane. The presence of phosphoric group of ethylene glycol methacrylate phosphate (EGMP) (second block) was confirmed by ^{H}NMR and ^{P}NMR.

2.2.2 Polymer characterization

The structure of the polymer is shown in Figure 1a. Peak at 4.1 ppm in Figure 1b represents the signal of final polymer and the percentage of monomer conversion was also measured by HNMR spectra of the reaction mixture before and after polymerization by comparing the integral ration of the vinyl protons of monomer and unchanged methylene protons of the POEGEA adjacent to the ester bond at 4.1 ppm, and the peak at 0 ppm in Figure 1c indicates the presence of phosphate in the final polymer[2]. Fourier transform infrared spectroscopy (FTIR) was further confirmed the structure of the 13 PEG polymer (Figure 1d). The peaks at 850 and 949 cm^{-1} correspond to the P-O bond from the phosphate segment of the polymer and the C=S bond from the RAFT agent, respectively.

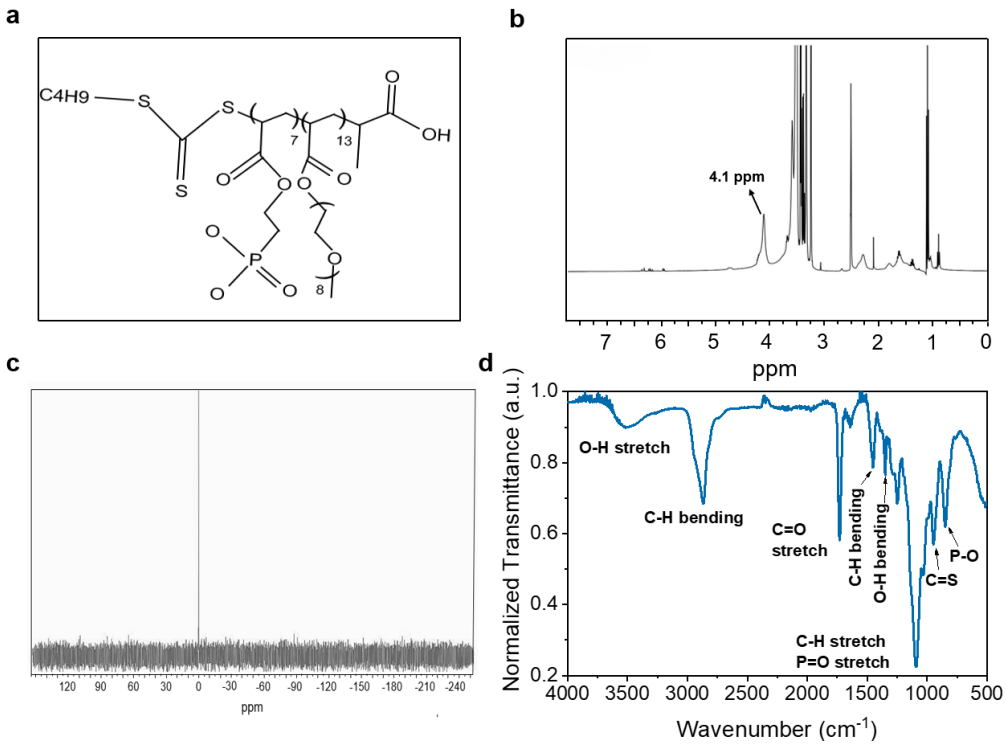

Figure 1. Polymer characterization. a, The structure of polymer; b, ^{1}HNMR spectrum of polymer; c, pNMR spectrum of polymer; d, FTIR spectra of polymer

2.2.3 Surface modification protocol and characterization via ligand exchange

To enable the use of UCNPs for the further protein detection, their transfer from an oil phase to an aqueous phase is essential. This was achieved using the ligand exchange method (Figure 2a), a versatile strategy relying on the high affinity of the new ligand for the nanoparticle surface. Initially, 0.5 mL of oleic acid-coated UCNPs (20 mg/mL) in cyclohexane were centrifuged at 20,240 g for 30 minutes and redispersed in 1 mL of tetrahydrofuran (THF). A solution of the diblock copolymer (10 mg) in 0.5 mL of THF was then added to the UCNP dispersion. The reaction mixture was sonicated for 1 minute and incubated on a shaker at room temperature for 14 hs. The polymer-coated UCNPs were purified by washing four times with varying THF/Milli-Q water ratios, followed by centrifugation at 20,240 g for 30 mins. Finally, the polymer-coated UCNPs were resuspended in 1 mL of Milli-Q water for further use. After ligand exchange, the appearance of the C=O stretches at 1731 cm^{-1}, and P=O stretches at 1100 cm^{-1} confirms the polymer grafting on the surface of UCNPs (Figure 2b). These

characterizations were used to verify successful ligand exchange before subsequent antibody conjugation.

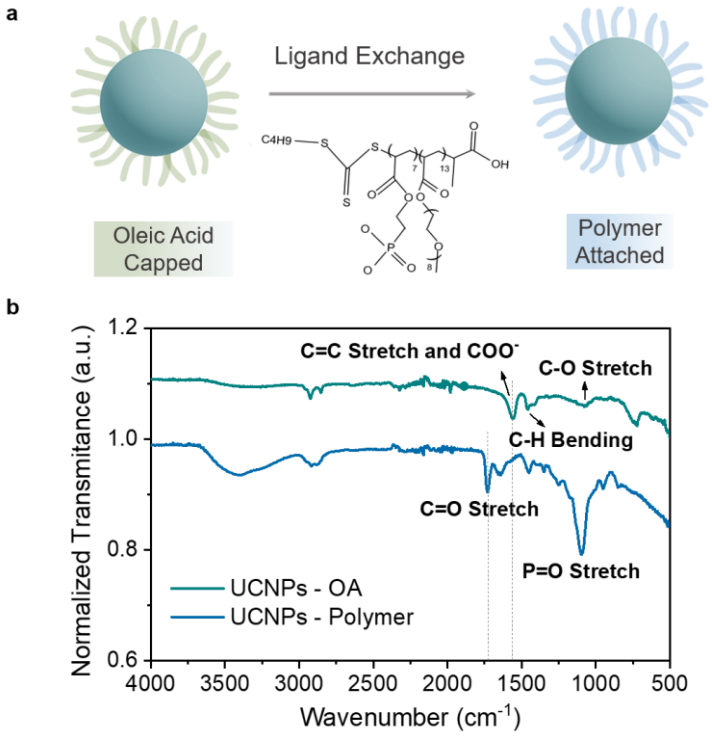

Figure 2. Characterization of the UCNPs after-modification. a, Schematic of the ligand exchange reaction of oleate-coated UCNPs with polymer. The hydrophobic oleate ligand is replaced by the hydrophilic polymer; b, FTIR spectra of UCNPs-OA (green line), UCNPs-polymer (blue line).

2.3 Surface modification protocol via ligand free

The carboxylic groups of polyacrylic acid (PAA, MW:18,000) also coordinate to the lanthanide ions on the UCNP surface resulting in a high dispersibility of the UCNPs in water. Firstly, UCNPs (in THF) were precipitated out by adding 0.6 mL of ethanol and then pelleted by centrifugation at 20,240 g for 6 mins. The centrifuged supernatant was replaced with a solution containing 0.5 mL of hydrochloric acid (2.0 M) and 1 mL of ethanol, the mixture was sonicated for 5 mins. Then the nanoparticles in dispersion were centrifuged at 20,240 g for 40 mins to obtain the ligand-free nanoparticles. The nanoparticles were further purified by washing three times in 0.5 mL ethanol and 0.5 mL H_2O. The ligand-free nanoparticles were dispersed in 0.5 ml H_2O, then measure the remaining amount of UCNPs. The dispersion was mixed with PAA (5:1 for PAA to

UCNPs) in 1.5 mL of water. Thereafter, 0.5 mL of 0.2 M NaOH was added dropwise while stirring with 1000 rpm for 4 hs at room temperature. After the reaction, the products were collected by centrifugation at 20,240 g for 20 mins and washed three times, finally re-dispersed in H_2O. In Chapter 3, PAA modification was additionally employed as a comparative surface modification approach to evaluate its performance relative to the polymer-based strategy.

2.4 Conjugation of UCNP and magnetic beads with antibodies

In the conjugation process, we employed both the EDC/NHS coupling strategy and a commercial bioconjugation kit. These two approaches were applied in different platforms: the EDC/NHS method was used in the lateral flow immunoassay for milk protein detection described in Chapter 3, while the commercial kit was utilized in the Beads-on-a-Tip assay for SARS-CoV-2 spike protein detection in Chapter 4.

2.4.1 Conjugation of Modified UCNPs-Polymer/PAA and Antibody

The modified UCNPs-polymer/UCNPs-PAA (0.1 mg) were first activated by 1-ethyl-3-(3 dimethylaminopropyl) carbodiimide (EDC) with 0.1 mg and 0.2 mg of N-hydroxysulfosuccinimide (sulfo-NHS). Then, the reaction mixture was incubated for 20 mins at 35 ^{o}C, rotated at 700 rpm. After that, the activated UCNPs were centrifuged for 12 mins at 20,240 g and dispersed with MES buffer (15 mM, pH 5.5), sonicated, and washed two more times. After the last centrifugation, 40 µl HEPES buffer (15 mM, pH 7.1) and 4 µL detection antibody (1 mg/mL) were added, making the final volume to 50 µL. The solution was then incubated for 3 hrs at 27 ^{o}C, rotated at 700 rpm. The conjugates were obtained by centrifugation for 12 mins at 20,240 g, and then dispersed in HEPES buffer, sonicated and washed two more times. After being washed, the conjugates were dispersed in the 0.1 mL storage buffer at 4 ^{o}C. The antibody was used as purchased without further purification. This method was used in Chapter 3.

2.4.2 Conjugation of antibody on the surface of UCNPs-polymer with the commercial kit

AnteoTech Nano Kit (A-PCKS) was used for bioconjugation of the UCNP-polymer with detection antibodies. In brief, 12 µL UCNP-polymer (10 mg/mL) were mixed with 100

µL activation buffer containing 25 mM sodium fluoride and incubated on a shaker (800 rpm) for 1 hour at room temperature. Then, the active nanoparticles were washed with particle washing solution (200 µL) once and then conjugation solution (200 µL) by centrifugation at 20,240 g for 1 hour at 4°C. Subsequently, 200 µL of conjugation Buffer were added. Then 100 µL active UCNP-polymer solution containing 25 mM sodium fluoride mixed with 4 µL of detection antibody (1 mg/mL). The mixture was incubated on a shaker (800 rpm) for 1 h at room temperature. Next, 10 µL of BSA solution (10% w/w) was added to the mixture, followed by another one-hour incubation. The delta spike antibody-UCNPs (UCNPs-Abs) were, then, centrifuged at 20,240 g for 1 h at 4 °C and washed with the storage buffer. Finally, the UCNPs-Abs were resuspended in 100 µL of storage buffer and stored at 4 °C for further use. This method was used in Chapter 4 to 5.

2.4.3 Conjugation of magnetic beads with Abs (MBs-Abs)

Magnetic bead surface modification is included in this chapter as a preparatory step for subsequent assay platforms developed in Chapter 4 and 5. The EDC-NHS method was used for the bioconjugation of MBs with capture antibodies. First, the MBs were washed three times by adding 100 µL of 25 mM MES, pH 5, and mixing well. After washing, 0.1 mg of beads (30 mg/mL) was transferred to a reaction tube and concentrated to generate a 100 mg/mL solution. EDC and NHS were each separately dissolved in 25 mM MES buffer (pH 5) at a concentration of 40 mg/mL. Then, 25 µl of the EDC solution and 25 µL of the NHS solution were added to the washed MBs. The mixture was gently mixed and incubated with slow tilt rotation at room temperature for 40 mins. Following activation, the tube was placed on a magnet for 1 min to separate the beads, and the supernatant was removed. The MBs were then washed three times with 200 µL of 25 mM MES buffer, pH 5. Next, 1 µg of capture antibodies, dissolved in 25 mM MES buffer (pH 5), was added to the activated MBs, adjusting the final volume to 50 µL. The mixture was incubated for 1 hour at room temperature with slow tilt rotation. After antibody conjugation, the tube was placed on a magnet for 1 min, and the supernatant was discarded. The MBs-Abs were then washed three times with washing buffer (10 mM phosphate buffer, pH 7.4 containing 0.05% Tween-20). Subsequently, 1 % BSA was added for blocking, and incubated for 40 mins. Finally,

the MBs-Abs were washed three times with washing buffer to complete the conjugation process and store in 25 µL 10 mM phosphate buffer.

2.5 Conclusion

This chapter describes the experimental procedures for UCNP synthesis, surface modification, and antibody bioconjugation used in this thesis. Ligand exchange using custom-designed polymers enabled the transfer of UCNPs into aqueous media and provided functional groups for subsequent antibody coupling. Antibody conjugation was achieved using both EDC/NHS chemistry and a commercial bioconjugation kit, depending on the assay platform employed in later chapters. In addition, magnetic beads were functionalized with capture antibodies as a preparatory step for sandwich-format assays. Together, these procedures establish the experimental foundation for the UCNP- and MB-based biosensing platforms developed in subsequent chapters.

Reference

(1) Liu, B.; Chen, C.; Di, X.; Liao, J.; Wen, S.; Su, Q. P.; Shan, X.; Xu, Z. Q.; Ju, L. A.; Mi, C.; et al. Upconversion Nonlinear Structured Illumination Microscopy. *Nano Lett* **2020**, *20* (7), 4775–4781. DOI: 10.1021/acs.nanolett.0c00448 From NLM.
(2) Maddahfar, M.; Wen, S.; Hosseinpour Mashkani, S. M.; Zhang, L.; Shimoni, O.; Stenzel, M.; Zhou, J.; Fazekas de St Groth, B.; Jin, D. Stable and Highly Efficient Antibody–Nanoparticles Conjugation. *Bioconjugate Chemistry* **2021**, *32* (6), 1146–1155. DOI: 10.1021/acs.bioconjchem.1c00192.

Statement of Contribution of Authors for Chapter 3

[1] Ziwei Wu, Yitong Zhao, Mahnaz Maddahfar, Tesfaye Asrat, Bradley J Walsh, Dayong Jin, Jiajia Zhou*, “Upconversion lateral flow test for A1 beta-casein proteins in milk and infant formulas”, ***Not submitted****.*

	Z.W	Y.Z	M.M	T.A	B.W	D.J	J.Z
Experimental Design	●					●	●
Sample Preparation	●	●	●	●			
Data Collection	●	●					
Data Analysis	●		●		●	●	●
Manuscript	●				●	●	●

I was responsible for the experimental design and conducted the majority of the experimental work, including UCNP surface modification, antibody bioconjugation, lateral flow strip fabrication, data analysis, as well as manuscript writing.

Signatures from co-author:

Y.Z: Production Note: Signature removed prior to publication.

M.M: Production Note: Signature removed prior to publication.

D.J.: Production Note: Signature removed prior to publication.

T.A: Production Note: Signature removed prior to publication.

B.W: Production Note: Signature removed prior to publication.

J.J: Production Note: Signature removed prior to publication.

Chapters 3 are based on manuscripts submitted for publication. For consistency and coherence within this thesis, the content has been adapted and integrated into the thesis structure; therefore, these chapters do not strictly follow the journal article format.

Chapter 3 Milk protein detection Based on Lateral Flow Immunoassay

Lateral flow immunoassay (LFIA) remains the most widely adopted technique in point-of-care testing (POCT) due to its simplicity, portability, and rapid detection capability. These advantages make it highly suitable for diverse applications, ranging from clinical diagnostics to food safety monitoring. In this project, we aim to achieve two primary objectives: (1) to detect 1% of A1 protein in milk (the requirements set in the dairy industry) with high sensitivity, and (2) to translate LFIA technology into practical industrial applications, bridging the gap between laboratory innovation and real-world implementation in the dairy sector. Milk quality is central to the dairy industry, as variations in milk proteins can significantly impact its nutritional value, safety, and overall product consistency. Although the monitoring of such protein variants is critically important, conventional detection technologies are not easily adapted for routine quality control in milk production, largely due to their complexity, cost, and lack of on-site applicability. This research aims to deliver a robust, sensitive, and scalable diagnostic tool that meets industrial requirements for speed, reliability, and ease of use. Through our collaboration with A2 company, we seek to advance the commercial viability of nanoparticle-enhanced LFIA platforms, ensuring consistent compliance with stringent quality standards and regulatory requirements across dairy products.

3.1 Background and current problem

Cows' milk is the base of a variety of dairy products consumed by most people. Milk from dairy cows has been regarded as nature's complete food, providing an important source of nutrients, including high-quality proteins, carbohydrates, and selected micronutrients[1]. Casein and whey proteins constitute more than 85-90% of cow's milk proteins[2] (Figure 1a). Of emerging importance in the past decade has been milk protein composition, more specifically the concentration of A1, which has been linked by clinical and epidemiological studies to a range of short- and long-term health effects and disease risk [3-6]. When digested in the small intestine, A1 releases a bioactive peptide called beta-casomorphin-7 (BCM-7) (Figure 1b). Binding of this BCM-7 peptide to the opiate receptors in the gut has been demonstrated to result in gastrointestinal inflammation and subsequent symptoms of lactose intolerance.

Additionally, epidemiological and mechanistic studies reflect a potential correlation between the consumption of A1 beta -casein and diabetes mellitus type 1, coronary heart disease, infant death, and autism [7-9]. In contrast, A2 and other variants show minimal associations or impacts on health. Hence the selective exclusion of A1 from milk may avoid symptoms and undesirable effects.

The profiles of protein variants even vary for a given breed of cow and are affected by many factors including season, weather, feed, nutritional levels, health status, exercise, age, stages of milking, intervals of milking, lactation period [10, 11]. With such structural similarity of A1 and A2, it is challenging to distinguish and resolve these two proteins by standard biochemical means, let alone quantify them in a mixture. Most of the milk quality control tools focus on the testing of chemical composition, milk purity and various microbial levels rather than specific protein targeting[12]. Rapidly and effectively screening the right milk source on the farm poses a challenge, necessitating the development of a rapid protein test. This is particularly important in the context of A2 milk production, where any contamination with A1 during milk processing is considered a departure from the standard quality. Therefore, from an industry application standpoint, there is a critical emphasis on rapidly testing proteins to ensure the quality of milk products.

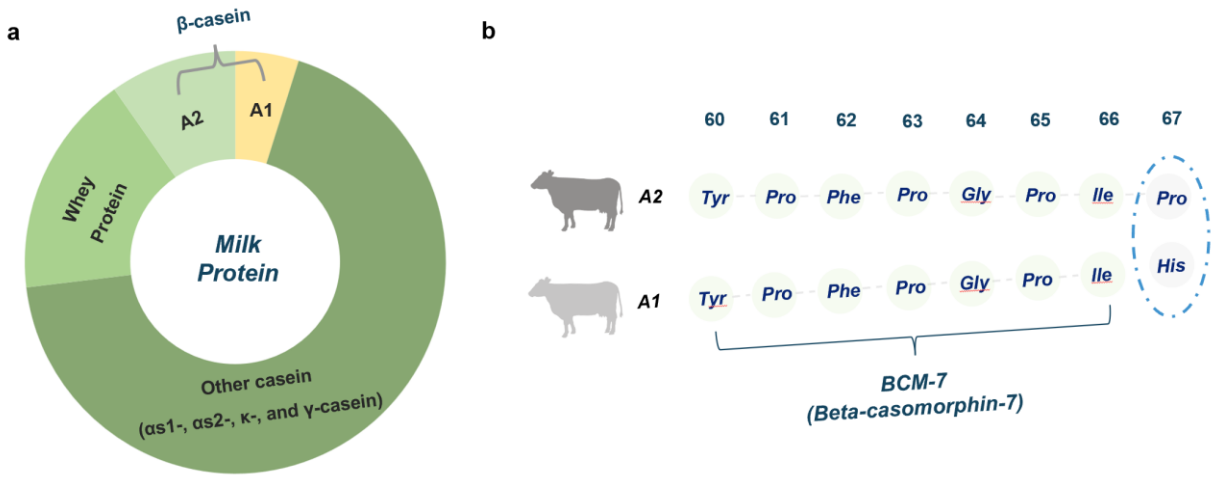

Figure 1. a, The composition of milk protein; b, the structure difference between A1 and A2 beta-casein

3.2 The traditional detection methods for A1 protein

The traditional methods for detecting and measuring A1 protein include ultra-performance liquid chromatography and high-resolution mass spectrometry (UPLC-

HRMS) for intact proteins, which can characterize the major milk proteins and their genetic variants with the goal of detecting 2% A1 in A2-based infant formula[13]. A liquid chromatography-tandem mass spectrometry (LCMS) method has been demonstrated to confirm the presence of 1% A1-like beta caseins in A2 milk[14]. Besides, a commercialized sandwich ELISA kit is available for detecting A1 beta casein with the LOD of 3.1 ng/mL and has been applied for detecting A1 protein in milk products[15]. However, these methods are constrained by long reaction time, limited quantitative capabilities and non-rapid detection necessitating the development of a more efficient and convenient detection technique.

3.3 Rapid detection methods for A1 protein

Several rapid detection methods have been developed for milk protein analysis, as summarized in Table 1. Among them, a rapid testing method involves a label-free optical biosensor sandwich format immunoassay exploiting surface plasmon resonance detection for the estimation of the beta-casein content[16]. The LOD for total beta casein was 5.5 ng/mL, and it has been applied to detect the fluid milk, with quantified beta casein content of 2.3 mg/mL. Another method used carboxyl-modified fluorescent microspheres (FMs) covalently conjugated with antibodies to form antibody-FMs complexes, which were then applied in a lateral flow assay[17]. The detected concentration of total casein in defatted milk was 100 ng/mL. However, these methods were exclusively used for detecting total beta casein and not for specific protein identification. A competitive microsphere-based detection method has been developed to distinguish between A1 and A2 beta-casein proteins[18]. This method has been applied to detect the adulteration of raw milk with 1% A1A2 milk in A2A2 milk, which originates from cows genotyped as A1A2 and A2A2, respectively. However, the washing steps could be operator-dependent, potentially resulting in increased procedural complexity.

Table 1. The Rapid detection methods for A1 protein

Method	Principle	Reaction time	Analytical LOD	Real sample Performance	Ref

Biosensor immunoassay	Sandwich format	6 mins	5.5 ng/mL of total beta casein	2.3 mg/mL of total beta casein in milk	[16]
Fluorescent microspheres assay	Competitive format	20 mins	-	100 ng/mL of total caseins in milk	[17]
Microsphere homogenous immunoassay		40 mins	-	adulteration of raw milk with 1% A1A2 milk in A2A2 milk	[18]

3.4 The problem with milk antibody and solution

As discussed in Chapter 1, highly doped UCNPs can provide enhanced luminescence intensity, which is beneficial for improving assay sensitivity in LFIA. In this work, highly doped core-shell β-$NaYF_4$ nanoparticles co-doped with 40% Yb^{3+} and 4% Er^{3+} were employed as signal reporters for the detection of A1 protein through a sandwich-format immunoreaction. A key challenge in this study arises from the limited availability of antibody pairs suitable for A1 protein detection. Currently, only polyclonal antibodies are commercially available for A1 protein, which generally exhibit lower binding efficiency in sandwich assays compared with monoclonal antibody (mAb) pairs. To illustrate the impact of antibody affinity on sandwich assay performance, ELISA experiments were performed in this work using polyclonal antibodies for A1 protein and monoclonal antibody (mAbs) for SARS-CoV-2 proteins, and the results are shown in Figure 2. The SARS-CoV-2 system is introduced here solely as a methodological reference to demonstrate the influence of antibody pairing on assay efficiency.

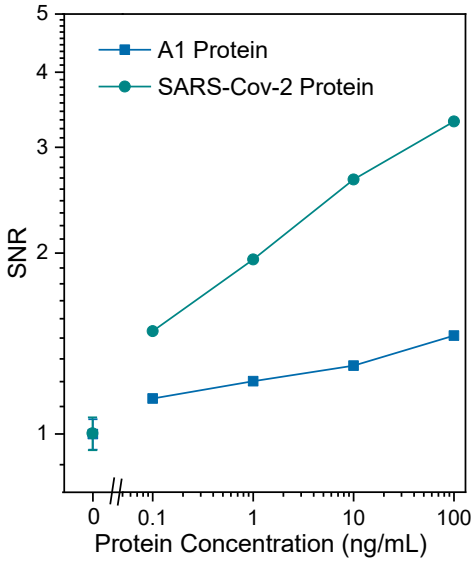

Figure 2. The comparison of binding efficiency between A1 and SARS-COV-2 protein detection in ELISA (n=3 at each concentration)

A straightforward application of protocols from our previous studies[19] using PAA modified UCNPs resulted in significant non-specific binding on the test line in LFIA Figure 3a), which ultimately leads to the failure of the assay (Figure 3b). To establish a new platform that is suitable for A1 protein detection, we modified UCNPs with POEGMEA based RAFT polymer to reduce the non-specific binding on the test line and further develop a protocol to conjugate polyclonal antibodies (pAbs) onto UCNPs (See the detailed polymer synthesis in Section 2.2.2.1 in Chapter 2. Currently, several studies have applied POEGMEA-based coatings on nanoparticles across different application areas. For example, coating magnetic nanoparticles with POEGMEA effectively reduces non-specific protein adsorption[20]. When applied to mesoporous silica nanoparticles, POEGMEA forms a hydrophilic outer brush layer that enhances colloidal stability and imparts stealth characteristics, while supporting an inner pH-responsive PDEAEMA layer for controlled drug release[21,22]. Optimizing the chain length of POEGMEA on UCNPs provides best condition for long-term colloidal stability and high antibody conjugation efficiency[23]. However, this work represents the first application of POEGMEA-modified UCNP conjugates in LFIA, as well as incorporating two key practical factors.

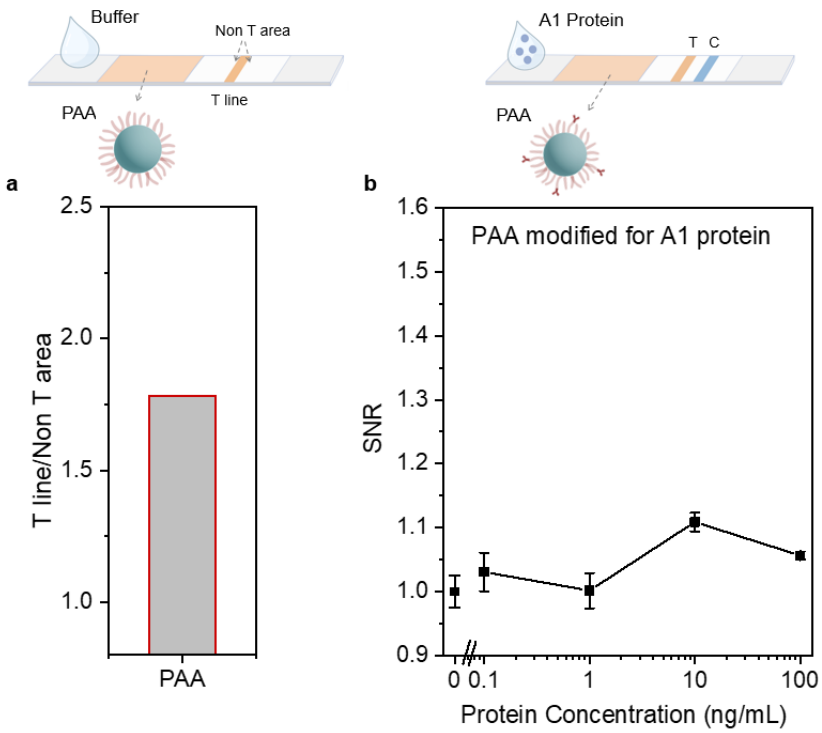

Figure 3. PAA modification and the results on assay. a, The non-specific binding of the PAA modified UCNPs; b, A1 protein concentration dependent SNR for the LFIA by using PAA modified UCNP conjugates (n=3 at each concentration). This assay fails to exhibit a linear relationship between the SNR and protein concentration.

In this work, firstly, a dry chemistry method (SI) was employed to fabricate the paper strips, aimed at industrial translation, in which the conjugates were sprayed onto the conjugation pad and dried, rather than being off-line reacted with analysts in suspension, as commonly reported in literatures. Second, a pair of polyclonal antibodies (pAbs) was used in the LFIA, instead of the more commonly used mAbs. To overcome this challenge, we created a strip design with a two-line configuration and successfully realized the test with linear relationship between A1 protein concentration and reporting signal.

3.5 Design of Strip and UCNP Probe

Our design of the upconversion luminescence based lateral flow assay is shown in Figure 4a. The reporter is made by upconversion nanoparticles conjugated with the detection antibody (polyclonal AbA1A2), namely UCNP-AbA1A2 conjugates. The conjugation between UCNPs and antibodies was facilitated by a polymer linker. As the

capture antibody of AbA1 is polyclonal, it may recognize and bind to many different epitopes of a single protein. To reduce this non-uniformity, we designed two lines on the NC membrane, i.e., a test line and a control line. With flow running, the sandwiched immunoreaction occurs at the test line and excessive conjugates are captured at the control line. The high lipid content in milk will prevent the flow on strips. Thus, to optimize the flow dynamics and ensure accurate assay performance, a dilution series of milk samples was prepared for detection by using the UCNPs-LFIA. As shown in Figure 4b, the signal-to-noise (SNR) was equal to S/N, where S is the the intensity ratio (T/C line) of experimental group (with proteins), and N is the intensity ratio (T/C line) of control group (without proteins).

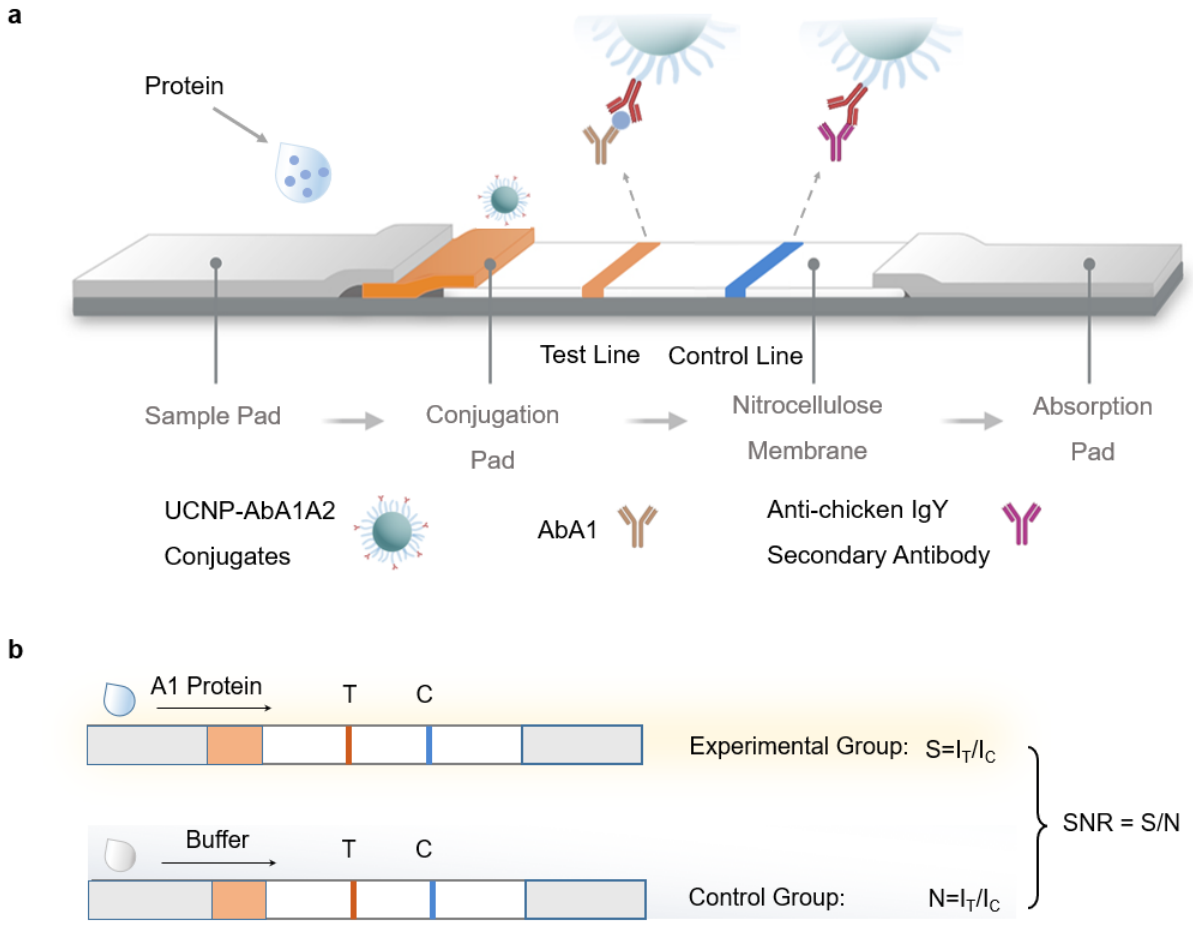

Figure 4. LFIA for A1 beta-casein protein detection. a, Schematic of the sandwich-based UCNPs-LFIA; b, Illustration of SNR calculation

3.6 Methods

3.6.1 Materials

3.6.1.1 Reagents

$YCl_3 \cdot 6H_2O$ (99.99%), $YbCl_3 \cdot 6H_2O$ (99.99%), $ErCl_3 \cdot 6H_2O$ (99.99%), NaOH (98%), NH_4F (99.99%), 1-octacene (ODE), oleic acid, Tetrahydrofuran (THF), 1-ethyl-3-[3-dimethylaminopropyl] carbodiimide (EDC), sulfo-NHS (*N*-hydroxysulfosuccinimide), MES powder, Poly(acrylic acid) powder, HEPES powder, Polyvinylpyrrolidone (PVP), Sodium Chloride Solution, Trizma base (≥ 99.9%), Tween-20, Bovine Serum Albumin (≥ 96%), Sucrose (≥ 99.5%).

3.6.1.2 Antibodies

Anti-chicken IgY secondary antibodies were purchased from Thermofisher Scientific (Massachusetts, USA) Rabbit anti-beta casein protein Polyclonal Antibody (detects both A1 and A2 beta -casein isoforms) (1 mg/mL), Chicken anti-Casein, A1 beta polyclonal Antibody (0.5 mg/mL), A1 and A2 beta -casein protein (0.4 mg/mL) were purchased from Biosensis Pty Ltd Adelaide, Australia). Goat anti-Chicken IgY (H+L) Secondary Antibody, HRP was purchased from Thermofisher. SARS-CoV-2 spike monoclonal antibody (40589-D008), SARS-CoV-2 omicron spike RBD specific antibody (40589-D007) and SARS-CoV-2 omicron (XBB.1.16) spike S1+S2 trimer protein (40589-V08H48) were purchased from Sino Biological, China.

3.6.1.3 Buffers

We developed two different coating buffers for the test line and control line, coating buffer for the test line (10 mM Tris buffer, 0.2% Triton, 0.5% Sucrose) and the control line (10 mM Tris buffer, 0.5% Sucrose), respectively. The storage buffer (20 mM Tris buffer, 2.5 mM NaF, 1% Sucrose, 0.4% Tween, 1% BSA, 0.9% PVP, 0.5 M NaCl) is used to store the UCNPs after conjugation. The running buffer (10 mM Tris buffer, 1% BSA, 1% Tween) was used to dilute samples for strip testing.

3.6.1.4 LFIA components

Sample pad (Product 8114-2250, Whatman CF4, 22 mm x 50m, 482 µm thickness) and Nitrocellulose membrane (Product 10547153, Whatman FF170HP 20 mm x 50m) were purchased from Cytiva Pty Ltd (Sydney, Australia). Conjugation pad (254 mm x 0.3 m) was purchased from Biotech Australia Pty Ltd (Melbourne, Australia).

Absorption pad (15 mm x 100 m) was purchased from Alcolizer Pty Ltd (Perth, Australia).

3.6.1.5 Milk and Infant Formula Source

Milk and formula containing both A1 and A2 beta casein or A2 beta casein only were obtained through purchase of commercially available products.

3.6.2 Fabrication of Lateral Flow Strips

The overall components of our strip include a sample pad, conjugation pad, NC membrane, and absorption pad. Since the background noise of polyclonal antibody is high in this experiment, A1 beta Polyclonal Antibody (AbA1) was diluted 20 times with coating buffer to decrease non-specific binding. The test line and control line on the NC membrane were fabricated by capillary pens loaded with the diluted AbA1 (0.025 mg/mL) and anti-chicken IgY secondary antibody (IgY) (0.1 mg/mL), respectively. The distance between the two lines was set to 4 mm. The original conjugates were sprayed on the conjugation pad with 0.3 µl x 3 times using the dry chemistry method. The end of each element of the strip was overlapped by 2 mm, thus ensuring a continuous flow of the sample solution. The conjugation pad and NC membrane were dried in a 37 °C oven for 2 hrs. Once assembled and cut to a width of 3.3 mm, the strips were stored in the desiccator for further use.

3.6.3 Strip reader design

The lateral flow assay was operated under an excitation power density of approximately 250 mW/cm^2. At this excitation level, the use of highly doped upconversion nanoparticles is sufficient to achieve robust signal generation for lateral flow detection. For signal acquisition, the strip was placed into a purpose-built test machine (Figure 5), which integrates a 980 nm near-infrared laser excitation source and a spectrometer for detecting upconversion luminescent signals at the test (T) and control (C) lines. The laser beam was focused to a spot size of approximately 400 µm and directed onto the surface of the strip. A scanning process along the X-axis was employed to sequentially excite predefined regions corresponding to the C line (2.2–2.8 mm) and the T line (4.6–5.2 mm) (Figure 6). The total reaction time for each strip was less than 10 min, and the scanning and readout process required approximately 40 s per strip.

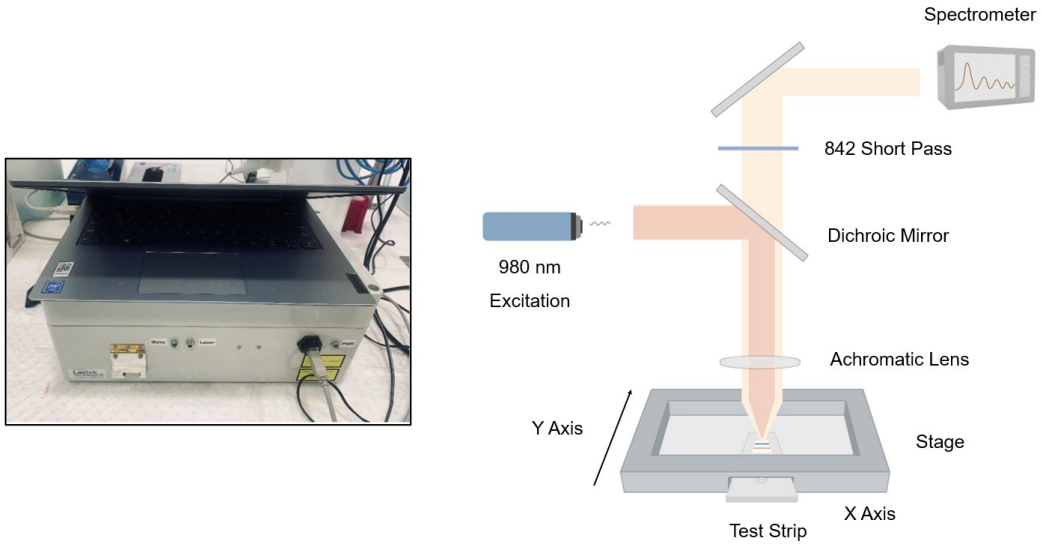

Figure 5. Custom-built 980 nm excitation and detection system for UCNP-based LFIA. The system employs a 980 nm laser for excitation, and the upconversion emission is collected through a dichroic mirror and an 842 nm short-pass filter and recorded by a spectrometer during controlled X–Y stage scanning

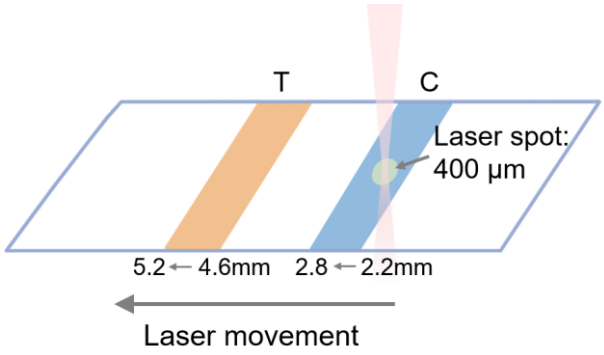

Figure 6. Schematic illustration of the scanning position and process for UCNP-based LFIA signal acquisition. The laser spot (≈400 μm) is moved across the T and C lines along the lateral flow direction, with defined scanning regions covering the respective line widths

3.6.4 Strip Testing Procedure

The milk was diluted directly without pre-treatment. 50 μl experimental (with A1 protein or milk products) or control groups (buffer only) were added to the test strip. The

solution of infant formula was formed by adding 0.1 mg powder to 0.1 ml running buffer. After adding the sample, the strip was placed into our purpose-built test machine to allow reading of the luminescent signal on both the T and C lines within 10 mins. The luminescent signal was recorded within 10 min while the strip remained moist. At this stage, sufficient residual moisture helps dissipate heat generated by laser excitation, thereby preventing local overheating or damage to the nitrocellulose membrane. The effect of water-induced luminescence quenching was minimal and did not significantly affect signal intensity or assay reproducibility.

3.7 Results

3.7.1 Morphology, Optical and Surface Properties of UCNPs

The surface of the as-synthesized UCNPs core (beta -$NaYF_4$:40% Yb^{3+},4% Er^{3+}) and core-shell (beta-$NaYF_4$:40% Yb^{3+},4% Er^{3+}@ $NaYF_4$) are capped by oleic acid, monodispersed in cyclohexane. The detailed synthesised protocol was in section 2.1.1, 2.1.3 and 2.1.4 in Chapter 2. The size of synthesized core and core-shell UCNPs cores were 27 and 30 nm, respectively. There was no sign of aggregation from the transmission electron microscopy (TEM) image (core UCNPs in Figure 7a and core-shell UCNPs in Figure 7b) and the size distribution analysis of core and core-shell UCNPs (Figure 7c and 7d).

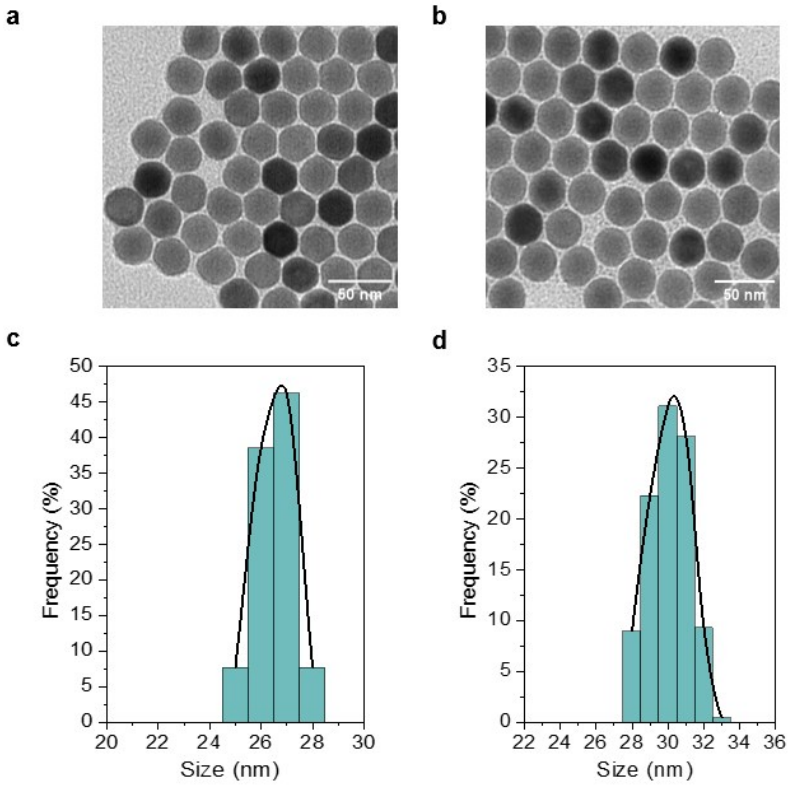

Figure 7. Characterization of the synthesized UCNPs. a, TEM image of $NaYF_4$:40% Yb,4% Er core UCNPs (Scale bar: 50 nm); b, TEM image of $NaYF_4$:40% Yb,4% Er core-shell UCNPs (Scale bar: 50 nm); c, The size distribution analysis of core UCNPs; d, The size distribution analysis of core-shell UCNPs

To change the hydrophobic to hydrophilic state, the oleate ligands on the surface of the UCNPs have been replaced with a custom designed polymer, the detailed characterization before and after surface modification process is in Chapter 2.2.2. Then, the polymer modified UCNPs have been further conjugated with the pAbs (AbA1A2) using EDC chemistry. The successful conjugation with antibodies can be confirmed using dynamic light scattering (DLS) and zeta potential measurements. As shown in Figure 8a, the Z-average hydrodynamic diameters of UCNPs coated with oleic acid, polymer, and antibody were 38 ± 0.05 nm (PdI = 0.041), 50 ± 0.05 nm (PdI = 0.048), and 220 ± 1.2 nm (PdI = 0.367), respectively. The DLS distribution plot indicated that both hydrophobic OA and hydrophilic polymer ligands resulted in a narrow size distribution of nanoparticles. While a slight broadening and an increase in average particle size were observed following antibody conjugation, this on one hand confirms the successful attachment of antibodies, and on the other hand suggests that

some UCNPs may have formed dimer structures due to antibody-induced aggregation[24]. The surface charges (zeta potential) of the polymer and antibody-functionalized UCNPs were -17.7 ± 0.5 mV and -23.7 ± 0.5 mV, respectively (Figure 8b). The negative surface charge of the polymer-coated UCNPs can be attributed to the presence of carboxylic acid groups on the polymer, which deprotonate in aqueous solution. The further increase in negative charge after antibody conjugation is likely due to the net negative charge of the A1A2 antibodies, further confirming successful bioconjugation.

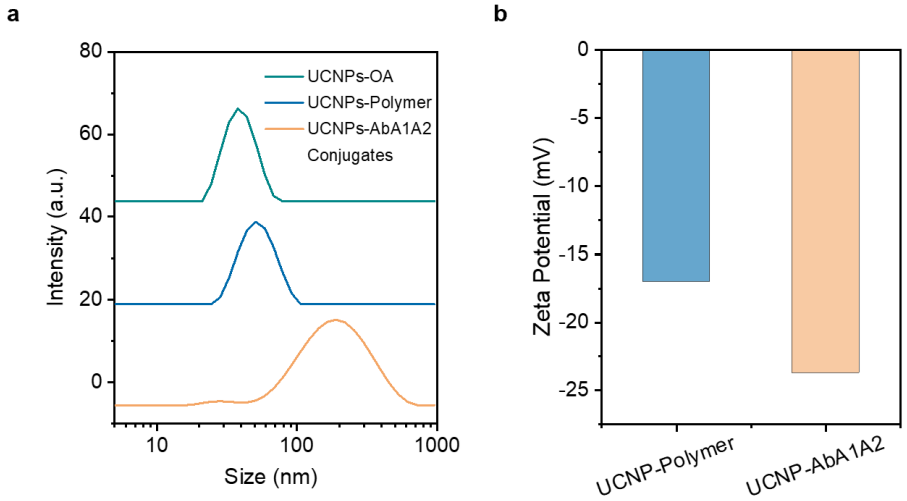

Figure 8. Characterization of the UCNPs before and after conjugation. a, DLS for UCNPs-OA, UCNPs-polymer and UCNPs-AbA1A2 conjugates; b, Zeta potential for UCNPs-polymer and UCNPs-AbA1A2 conjugates

3.7.2 LFIA assay optimization

3.7.2.1 Decrease non-specific binding

By using the polymer modified UCNPs, it only shows slightly excessive signal on the test line compared with non-test areas (ratio 1.1) in the paper strip (Figure 9a), proving the significantly reduced polymer linker induced non-specific adsorption on the test line compared with the case for PAA modified UCNPs (Figure 9b, ratio 1.8). While following the conjugation with AbA1A2, the conjugates show another type of non-specific binding because of the existence of antibodies (Figure 9c). Nevertheless, the overall non-specific binding is much reduced for the conjugates with our polymer as the linker compared with using PAA for the two-line design, as shown in Figure 9d. As

further illustrated by the full line-scan profiles of A1 pure protein as an example shown in Figure 10, the signal variation is characterized by strip-to-strip fluctuations in overall intensity rather than localized signal accumulation at specific membrane regions. This behaviour is attributed to the heterogeneous binding characteristics of the polyclonal antibodies, which lead to non-uniform capture efficiencies at both the test and control lines. Consequently, individual strips tend to exhibit either globally higher or globally lower signal intensities across both lines, rather than a gradual or spatially confined signal increase. Importantly, this observation confirms that the modest signal enhancement is not caused by UCNP retention or blockage within the nitrocellulose membrane but instead reflects antibody-related variability inherent to polyclonal systems.

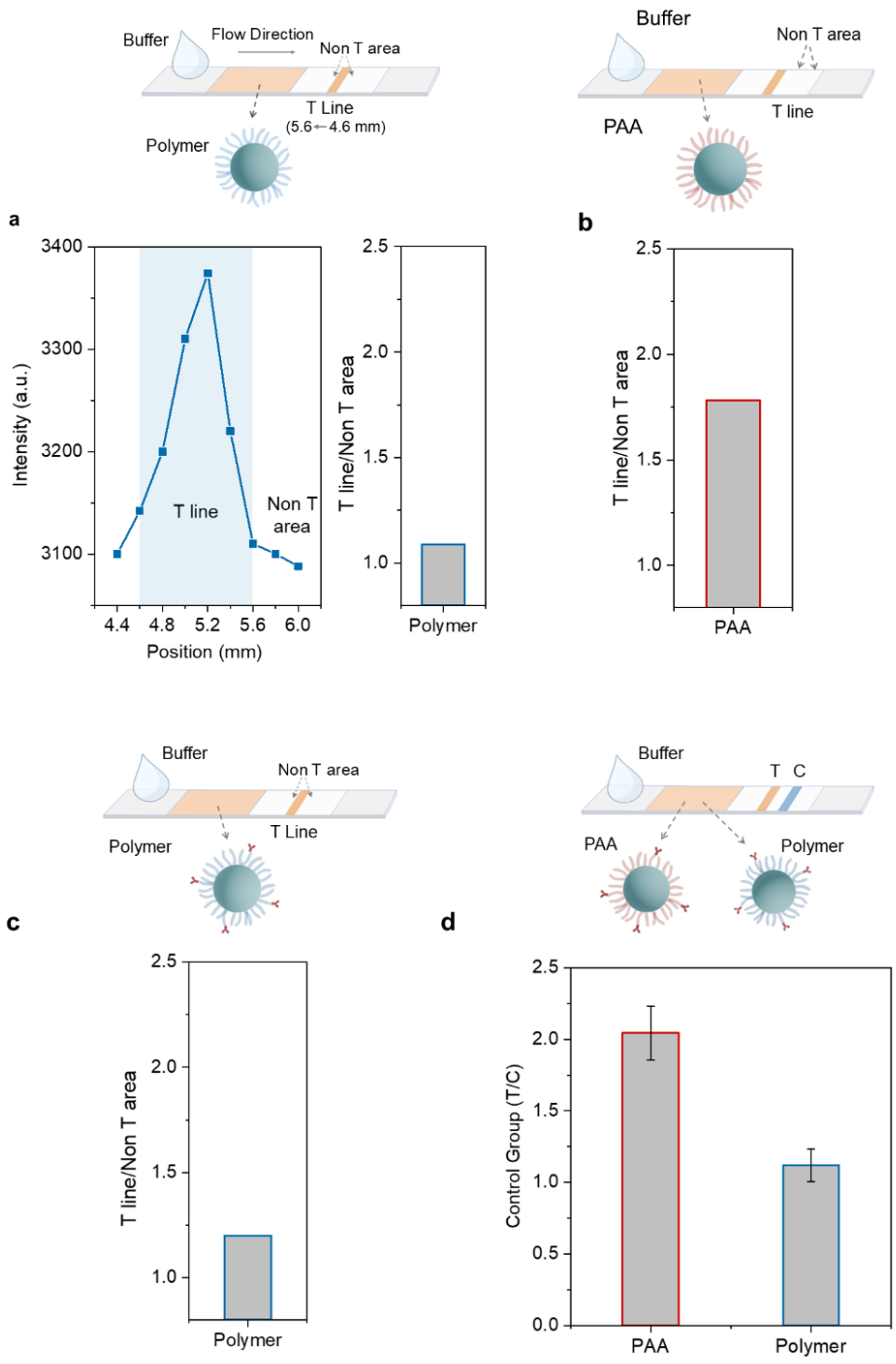

Figure 9. Strip performance assessment on non-specific binding between PAA and our polymer. a, Non-specific binding induced by the polymer was evaluated by applying UCNP-polymer to flow through the strip. The upconversion signal measured at the T line was normalized against the signal in the non-test (non T) area. The position on the NC membrane, marked in millimeters, was used to locate the T line; b, The non-specific binding of the PAA modified UCNPs; c, Non-specific binding induced

by the conjugated antibodies was evaluated by applying UCNP-AbA1A2 conjugates to flow through the strip; d, Overall assessment of non-specific binding on the two-line strip design, comparing the use of our polymer versus PAA as the linker for antibody conjugation (n=5 in each polymer)

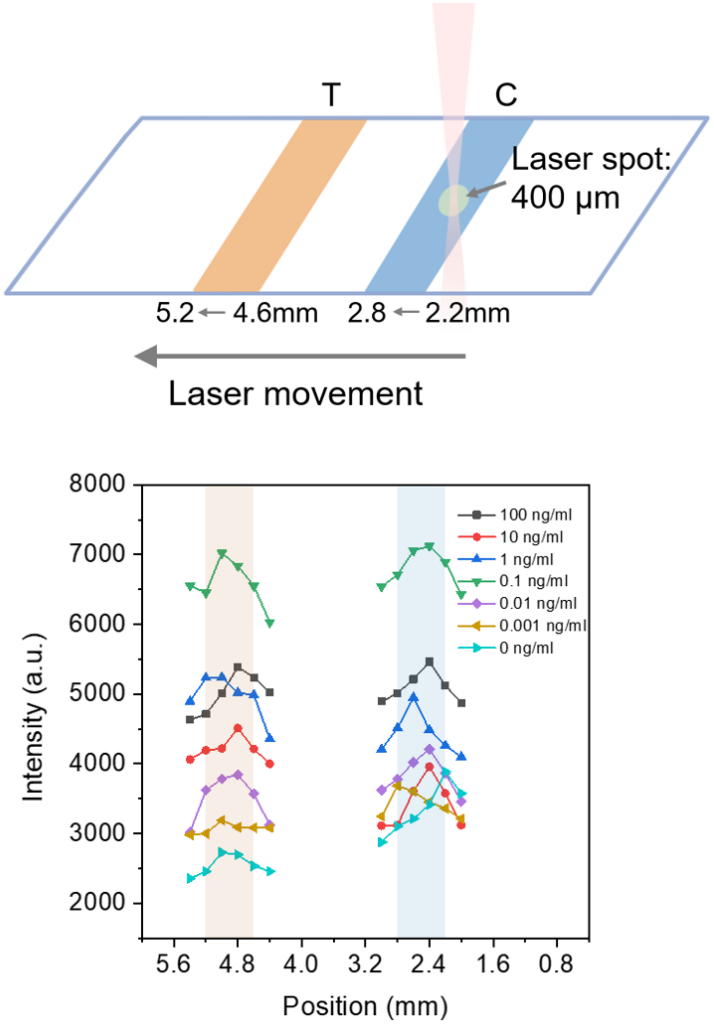

Figure 10. Scans of the LFIA strips for A1 pure protein

3.7.2.2 The feeding ratio between modified UCNP and Abs

With this new polymer, we systematically optimized every aspect of the assay, including nanoparticle polymer modification, antibody conjugation conditions, strip fabrication, assay buffer composition, and testing conditions. The final protocols presented represent the optimized procedures and have been repeated dozens of times to ensure experimental reproducibility. Here, we have optimized of the feeding molar ratio between modified UCNPs and AbA1A2 during conjugation (Figure 11a).

Three batches of conjugates with different molar ratios, 1:4, 1:8, and 1:12, were evaluated for their performance in LFIA. All three batches produced linear curves; Although the 1:4 ratio group showed a comparable detection range to 1:8, its SNR was consistently lower, likely due to insufficient antibody coverage on the UCNP surface, which limits the formation of stable immunocomplexes and reduces overall binding efficiency (Figure 11b). In contrast, the 1:12 ratio group exhibited the lowest SNR and a narrower detection range, likely due to excess antibody loading, which leads to increased non-specific binding. The 1:8 ratio was identified as the optimal conjugation condition, providing a balanced antibody density that maximizes assay sensitivity while maintaining signal stability.

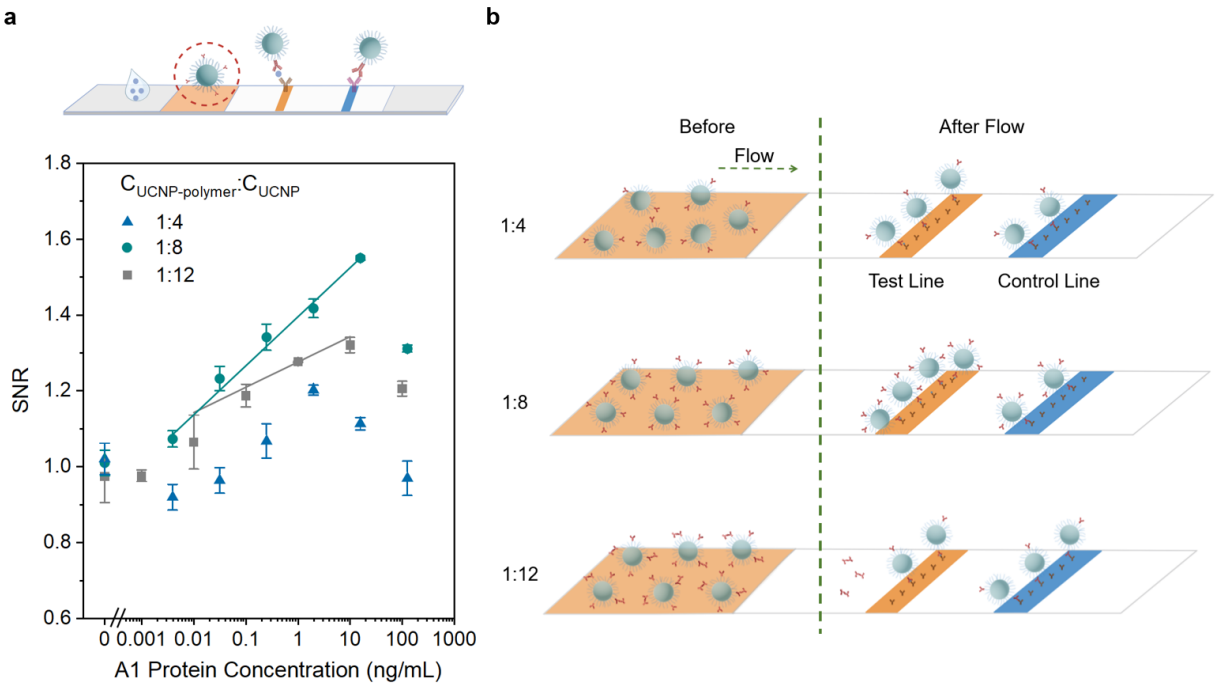

Figure 11. The optimization of feeding ratios modified UCNPs and AbA1A2. a, The linear curves obtained from UCNP-labeled immunoprobes at different ratios modified UCNPs and AbA1A2 (1:4, 1:8, and 1:12) in response to varying concentrations of A1 β-casein protein (n=3 at each concentration); b, Schematic illustration of different feeding ratios before and after lateral flow

3.7.2.3 The concentration of Abs on T line

To optimize the performance of the LFIA, we evaluated the effect of varying the concentration of the capture antibody (AbA1) coated on the test (T) line of the nitrocellulose (NC) membrane. Four different concentrations (0.1, 0.05, 0.025, and 0.015 mg/mL) were tested to determine the condition that yields the highest SNR across a range of A1 β-casein concentrations. As shown in Figure 12, all groups exhibited a positive signal response, with SNR increasing as the target concentration rose, followed by a decline at higher concentrations. Notably, the T line coated with 0.025 mg/mL AbA1 demonstrated the highest overall SNR, suggesting it offers the best balance between sufficient antibody availability for target capture and minimized non-specific background.

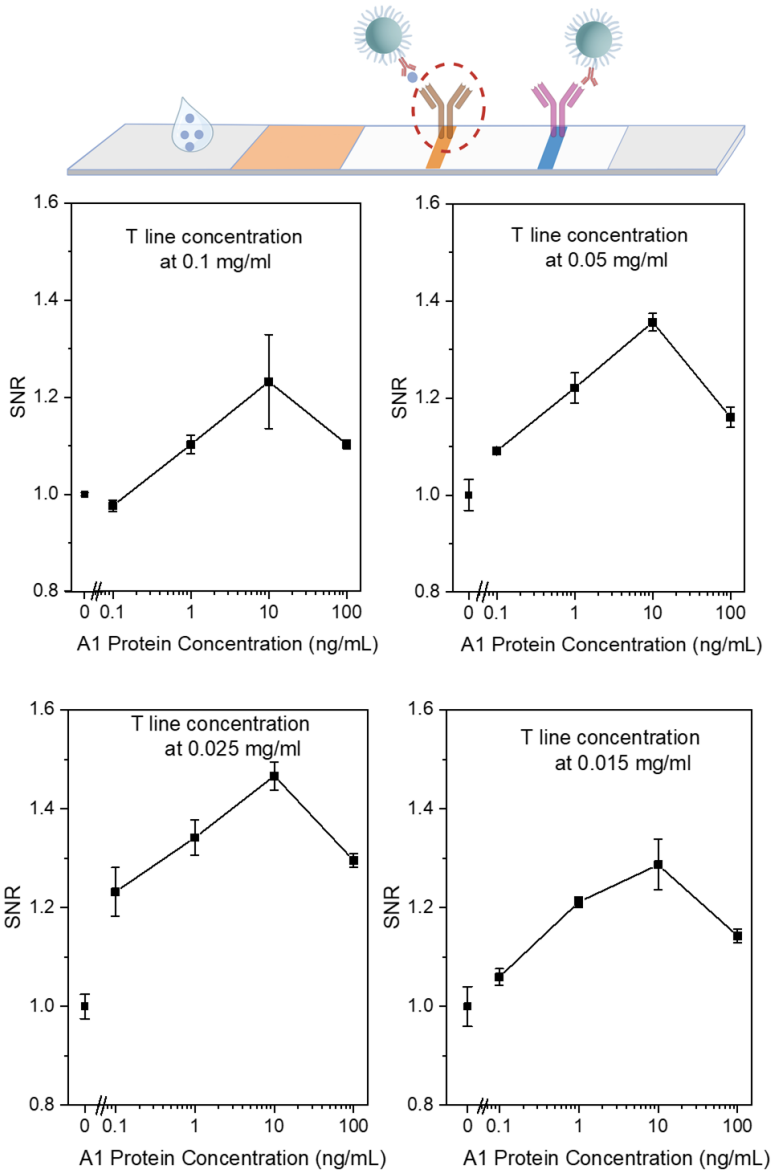

Figure 12. Optimization of the concentration of AbA1 on the T line of the nitrocellulose (NC) membrane in LFIA was performed using four different AbA1 concentrations (0.1, 0.05, 0.025, and 0.015 mg/mL), each evaluated across a series of A1 β-casein concentrations (n=3 at each concentration)

3.7.2.4 The percentage of Tween-20 for different cartridge (increase the reaction time)

To regulate the flow rate and enhance interaction time between the target and capture reagents, we optimized the percentage of Tween in the running buffer. Three different Tween concentrations (0.2%, 0.4%, and 0.8%) were evaluated in the LFIA system. As

shown in Figure 13, the 0.4% Tween-20 group demonstrated the highest SNR, suggesting that this concentration provides an optimal balance between flow speed and antigen–conjugates interaction. In contrast, both lower (0.2%) and higher (0.8%) concentrations resulted in reduced SNR, likely due to insufficient or overly delayed flow, respectively.

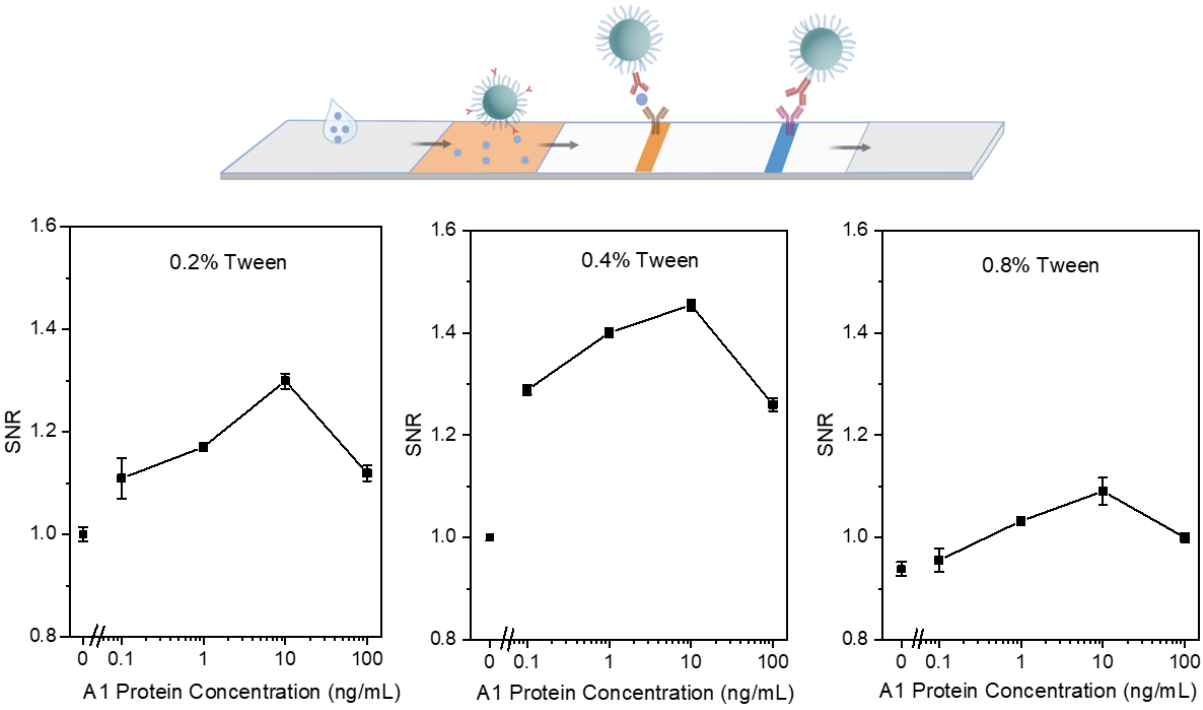

Figure 13. Optimization of Tween-20 concentration in the running buffer for LFIA. Three concentrations of Tween-20 (0.2%, 0.4%, and 0.8%) were tested to evaluate their effect on assay performance (n=3 at each concentration)

3.7.3 Performance Evaluation: Limit of Detection and Specificity

Then we used the optimized condition from 3.2.3 for LFIA test to explore the LOD, which is calculated to be 0.061 ng/mL, as shown in Figure 14a. The LOD in this work is defined as 3.3 times of standard deviation of the blank samples divided by the slope of the calibration curve. The response for A1 protein detection showed great linearity in the range from 0.001 ng/mL to 10 ng/mL (R2 = 0.998 and R2 = 0.969). While a high concentration of A1 protein, such as 100 ng/mL, resulted in a decreased SNR, due to excess antigen saturating the available binding sites on the capture and detection antibodies, hindering the formation of a sandwich complex on the T line (Figure 14b).

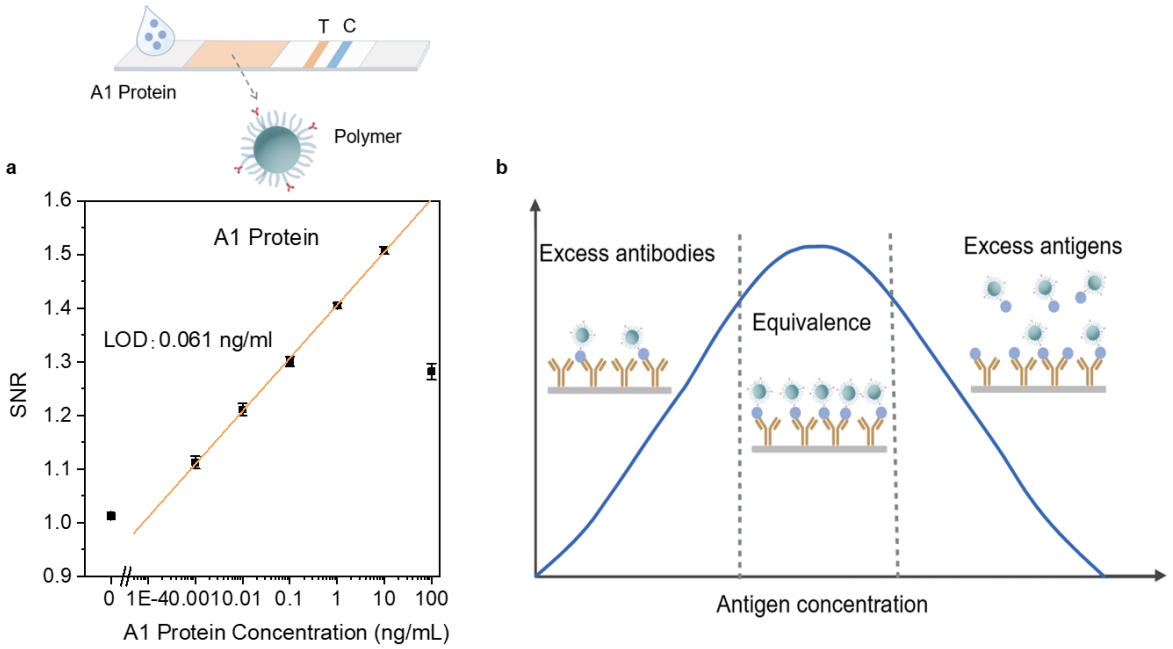

Figure 14. Strip performance assessment. a, Linear relationship curve and LOD (n=10 at each concentration); b, Schematic of the normal sandwich format.

Due to the similar structures of A1 and A2 proteins, the accuracy of the results can be influenced by the presence of the A2 protein molecules that typically dominate among beta-casein milk proteins. To validate the specificity of our method, we used the strips to assess the detection of A2 protein, aiming to also assess any potential cross-reactivity of A1 antibody with A2. 10 ng/mL A2 protein was applied to the strip, yielding nearly the same SNR as the control (Figure 15 orange and grey bars). This verified the absence of a cross reactivity of the A1 antibody with A2 protein. Alternatively, we mixed the A1 and A2 in a ratio of 1% to 99% and diluted the mixture by running buffer (Figure 15 red bars), to further confirm the specific detection of A1 without A2 interference. We found that the SNR of 1% A1 protein in A2 protein was similar to the recombinant A1 protein detection shown in Figure 2d, indicating satisfactory specificity.

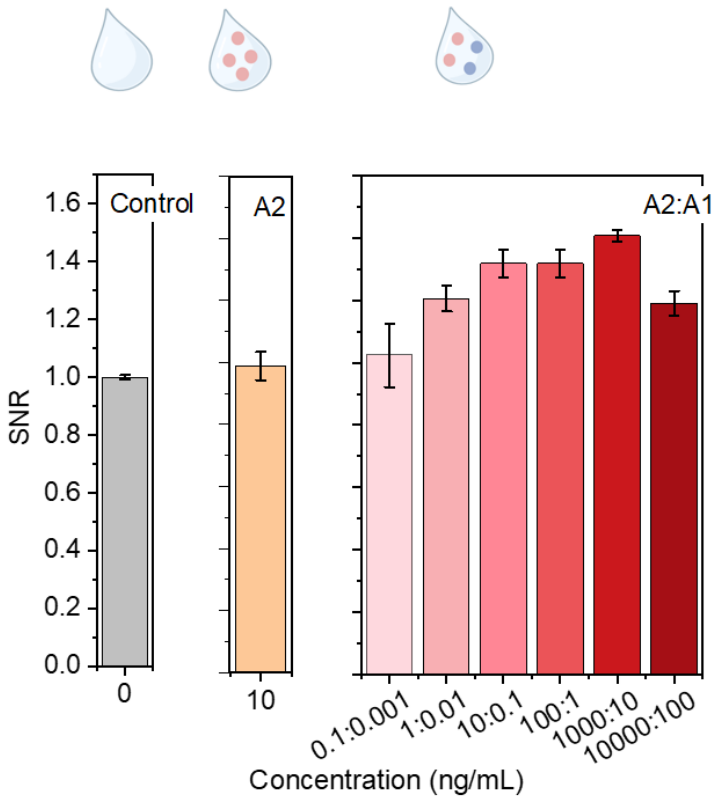

Figure 15. Specificity testing of the UCNP-based LFIA in the presence of A2 protein. SNR measurements were performed for the blank control, A2-only samples, and mixed A2:A1 samples at a fixed ratio of 1:100 to evaluate assay specificity against potential interference from structurally similar milk proteins (n=5 at each concentration)

3.7.4 Eliminating Interference from Unknown Ingredients in Milk Products

We next analyzed whether our test method was affected by potential influences from other ingredients in milk and formulas. Given the complex and varied nature of ingredients in milk products across different brands, creating a buffer that accurately mimics all these components poses a significant challenge. Here, we utilized A2 branded milk and infant formula as sources of unknown ingredients. These products were either diluted by a factor of 10^4 or prepared as a solution of 0.01mg/mL using running buffer, forming background buffers A and B. The decision to use A2 branded products was due to the claimed absence of A1 proteins. Next, we attempted to detect A1 recombinant proteins in background buffers A and B (Figure 16). Compared to the detection in running buffer shown in Figure 15a, we observed relatively lower SNR, which indicates the interference of other unknown ingredients. Fortunately, despite the

notable influence, we found that the A1 protein can still be detected within the dilution range of 0.1-100 ng/mL, with a linear relationship from 0.1 ng/mL to 10 ng/mL.

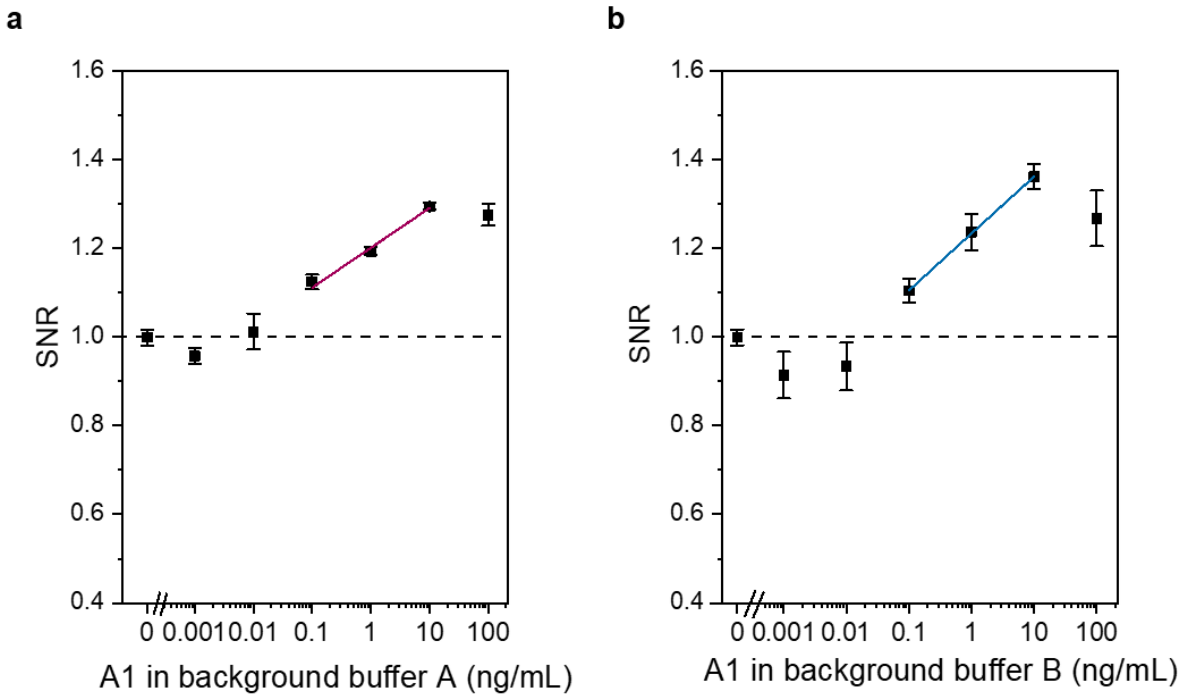

Figure 16. Calibration curve of A1 protein detection in background buffer A (a) and buffer B (b) (n=5 at each concentration)

3.7.5 A1 protein quantified in milk and infant formula

Following the establishment of this UCNP-LFIA technology, we further demonstrated its ability to quantify A1 protein in three brands of milk and three brands of infant formula, respectively. The milk was diluted 10^4 to 10^9 times using running buffer directly. For the formula, we initially weighed 1 mg and diluted in distilled water to a concentration of 1 mg/mL, then further diluted it by 10^2 to 10^8 using the running buffer without any protein. As shown in Figure 4, one brand of milk and one brand of infant formula yielded undetectable signals, while the other two products showed strong positive SNR. By calibrating this with the established linear relationship curve (red line in Figure 17a and blue line in Figure 17b), we quantified the A1 concentration to be 7.6 ng/mL at 10^5 dilution of the milk 2, equivalent to 0.76 mg/mL of A1 in milk 2. In milk 3, due to the concentration measured at 10^5 has exceeded our detection linear curve; in order to obtain a more accurate concentration value, we use the quantitative detection value at a dilution of 10^6, yielding the concentration with 1.42 ng/mL. This

means that the A1 content in milk 3 is 1.42 mg/mL. Similarly, we quantify the A1 concentration to be 6.3 ng/mL and 1.8 ng/mL at the 10^3 dilution of the infant formulas 1 and 2, respectively. While the A1 non-detectable milk and infant formula samples are the A2 branded ones as expected.

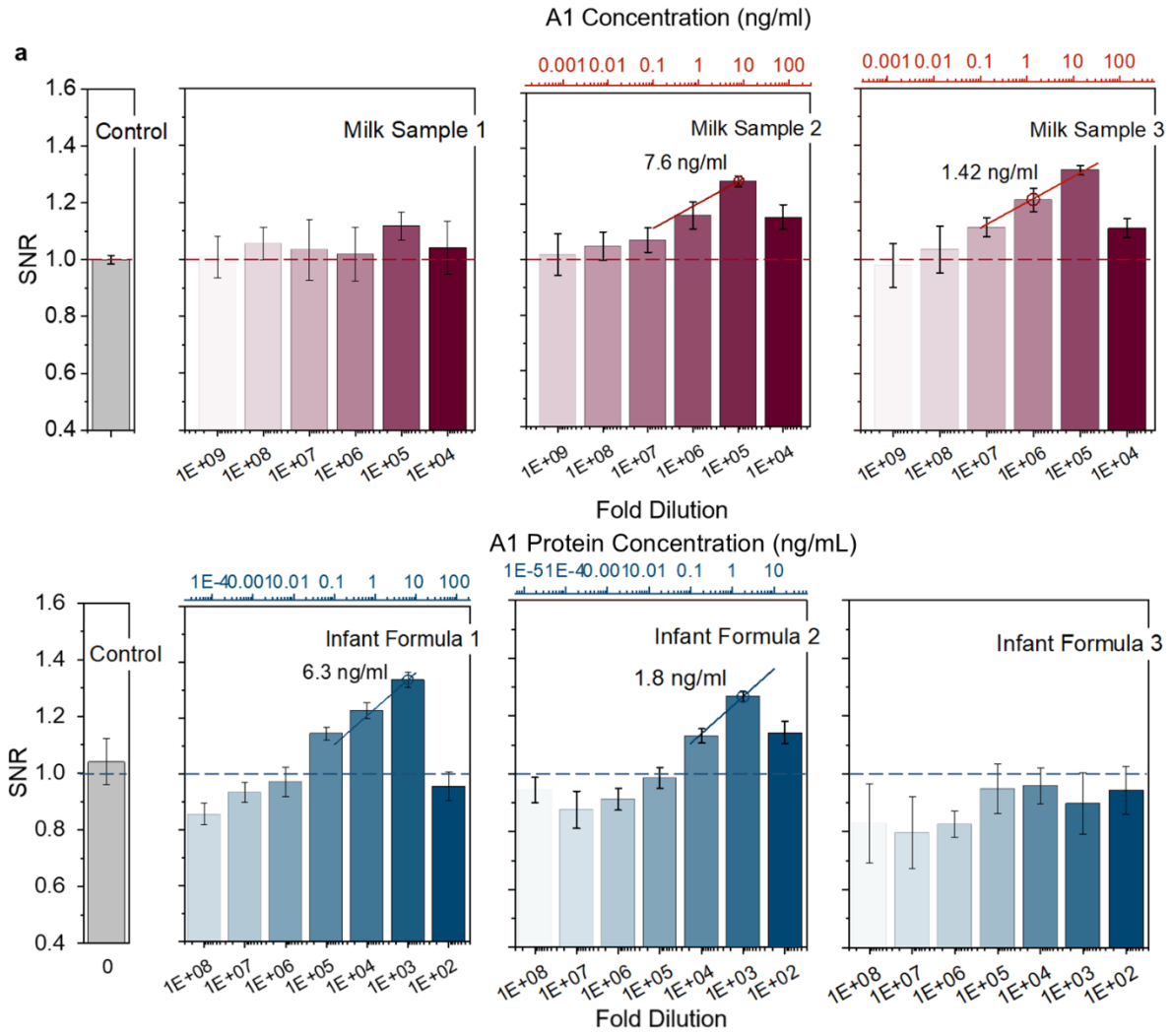

Figure 17. A1 protein detection and quantification in Milk (a) and infant formula (b) (n=5 at each concentration)

3.7.6 Validity analysis of testing results

Table 2. The comparison of our testing method with LCMS

	LC-MS		Our testing method	
	A1 in total beta-casein, (%)	A1 in milk, g/100 mL	A1 in total beta-casein, (%)	Detected A1 in milk, g/100 mL
Milk 1	<1	-	-	-
Milk 2	14.9	0.149 ± 0.0298	7.6 ± 1.52	0.076 ±0.0152
Milk 3	16.5	0.165 ± 0.033	14.2 ± 2.84	0.142 ±0.0284
	A1 in total beta-casein, (%)	A1 in milk, g/100 mL	A1 in total casein, (%)	Detected A1 in infant formula, g/100mL
Infant formula 1	32.6	-	10.2	0.00063
Infant formula 2	18.3	-	4.6	0.00018
Infant formula 3	<1	-	-	-

To validate our results, we compared them with that from LC-MS measurement (Table 2). All LC-MS measurements of the six products, including sample treatment, were conducted by third party providers and report the A1 protein content as a percentage of the total beta-casein. The beta-casein content in milk can fluctuate due to the season, conditions and other environmental factors, but it generally falls within the range of 10,000 ppm ± 2,000 ppm. This range was used for our calculations. From the results, we can confirm the ability of our method to differentiate the concentration difference of A1% in total beta-casein across different brands of milk, as well as providing the concentrations of A1 protein in milk. The tested trend of A1 percentage in total beta-casein for milk is Milk 1 < Milk 2 < Milk 3, which is consistent with the LC-MS results. Infant formula is a processed product, and its beta-casein content can vary depending on the formulation, which is unknown in our case. Therefore, a direct comparison between our test results and the LC-MS data is not feasible. As shown in Table 1, we were able to determine the A1 concentration and calculate its percentage

relative to total casein, based on the additional product information provided in Table 3.

Table 3. Information from commercial product information

	Information from products			
	total beta-casein in milk, g/100 mL	1 scoop of powder, g/100mL	Total casein, g/100 mL	total protein, g/100 mL
Milk 1	1 ±0.2	-		3.3
Milk 2				3.4
Milk 3				3.3
Infant formula 1	-	9.1	0.56	1.4
Infant formula 2		15	0.59	1.5
Infant formula 3		15	0.59	1.5

3.8 Conclusion

In this study, we have designed a sandwich format-based lateral flow immunoassay platform with UCNPs as reporters for milk protein detection. Our method achieved a limit of detection of 61 pg/mL. We have validated the method for specificity to A1 beta-casein protein, capable of differentiating 1% of A1 in A2 proteins. This platform technology has been successfully applied for rapid and quantitative detection of A1 protein in milk and infant formula, without the need for sample pretreatment. The

simplicity of this method fully meets the growing demand for quick, reliable, and easy-to-use diagnostic tools in various settings within industries and rural farms.

3.9 Prospective

Despite the successful development of a UCNP-based LFIA platform for A1 β-casein detection, several challenges remain, primarily stemming from the properties of the antibody and the complexity of real milk and formula samples.

Currently, only polyclonal antibodies specific to A1 β-casein are commercially available, and these exhibit inherent limitations in sandwich immunoassays. As Polyclonal antibodies bind to multiple epitopes, which will lead to batch-to-batch variability, lower binding specificity, and a higher likelihood of nonspecific interactions on the test line. This was obvious in our initial experiments using PAA-modified UCNPs, where high background signals were observed due to nonspecific adsorption. Furthermore, both traditional ELISA and LFIA using polyclonal-pair antibodies showed relatively low SNR, which may also be attributed to the poly-poly combination. While the composition of beta-casein in fresh milk is relatively consistent, the performance of A1 detection in infant formula is more challenging due to the presence of various added components. These complex matrices can interfere with antibody-antigen binding, ultimately affecting the SNR and performance of the assay.

Based on the results from Table 1, our quantified percentages are relatively lower compared to those obtained from the LC-MS measurements. The loss of A1 proteins in LFIA could be attributed to two possible reasons. First, A1 protein loss may occur before the sample reaches the test line, potentially due to it becoming trapped in the sample pad or NC membrane (Figure 18a). Second, in fresh milk in particular, beta-casein is primarily located at the core of casein micelles, making it inaccessible to the conjugates, which could contribute to the observed loss (Figure 18b). To address these concerns, future development should focus on designing tests that measure both A1 and A2 proteins in a given sample. By doing so, the A1 protein percentage can be determined relative to the A2 protein, mitigating the impact of pad or membrane-induced losses. Moreover, incorporating a chaotropic agent in the running buffer may help release β-casein, while using a reducing buffer (such as DTT or BME) could break the κ-casein bonds on the outer shell of the micelle. This approach would

enhance the accessibility of A1 proteins, maximizing their interaction with the conjugates and improving their capture efficiency.

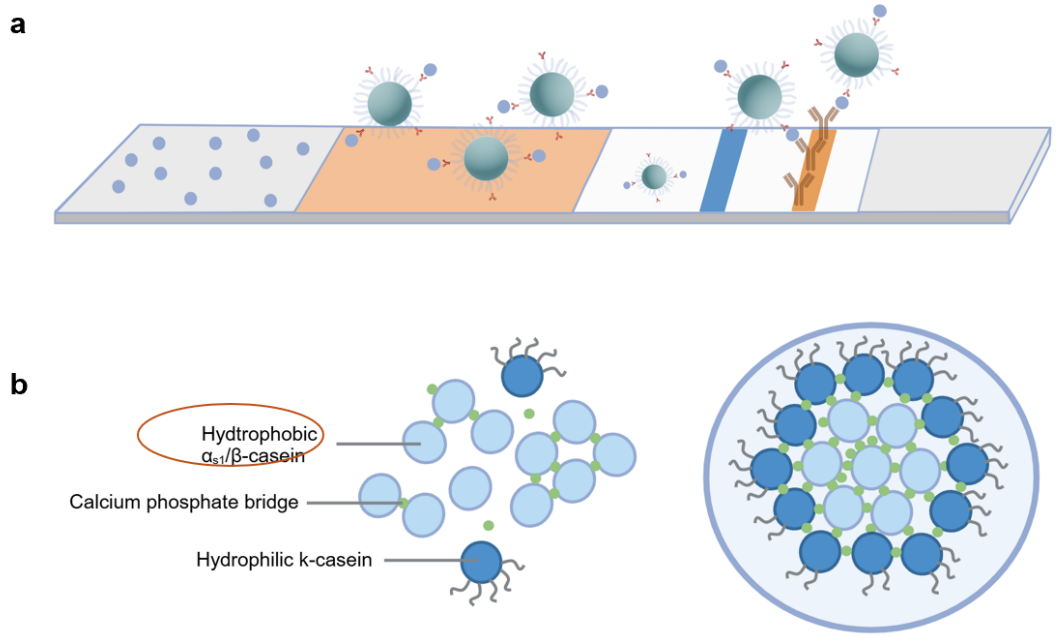

Figure 18. The Scheme of the loss of A1 proteins in LFIA. a, Sample loss occurs as target proteins may be retained or non-specifically adsorbed before reaching the test line, reducing detection efficiency; b, Illustration of casein micelle structure, where β-casein is primarily embedded within the hydrophobic core of the micelle, reducing its accessibility to UCNP–antibody conjugates during detection.

Reference

(1) Visioli, F.; Strata, A. Milk, dairy products, and their functional effects in humans: a narrative review of recent evidence. *Adv Nutr* **2014**, *5* (2), 131–143. DOI: 10.3945/an.113.005025 From NLM.
(2) Ruska, D.; Jonkus, D. Crude Protein and Non-protein Nitrogen Content in Dairy Cow Milk. *Proceedings of the Latvia University of Agriculture* **2014**, *32*. DOI: 10.2478/plua-2014-0011.
(3) Cieślińska, A.; Fiedorowicz, E.; Rozmus, D.; Sienkiewicz-Szłapka, E.; Jarmołowska, B.; Kamiński, S. Does a Little Difference Make a Big Difference? Bovine β-Casein A1 and A2 Variants and Human Health-An Update. *Int J Mol Sci* **2022**, *23* (24). DOI: 10.3390/ijms232415637 From NLM.

(4) Kuellenberg de Gaudry, D.; Lohner, S.; Bischoff, K.; Schmucker, C.; Hoerrlein, S.; Roeger, C.; Schwingshackl, L.; Meerpohl, J. J. A1- and A2 beta-casein on health-related outcomes: a scoping review of animal studies. *Eur J Nutr* **2022**, *61* (1), 1–21. DOI: 10.1007/s00394-021-02551-x From NLM.
(5) Fernández-Rico, S.; Mondragón, A. D. C.; López-Santamarina, A.; Cardelle-Cobas, A.; Regal, P.; Lamas, A.; Ibarra, I. S.; Cepeda, A.; Miranda, J. M. A2 Milk: New Perspectives for Food Technology and Human Health. *Foods* **2022**, *11* (16). DOI: 10.3390/foods11162387 From NLM.
(6) Kay, S. S.; Delgado, S.; Mittal, J.; Eshraghi, R. S.; Mittal, R.; Eshraghi, A. A. Beneficial Effects of Milk Having A2 β-Casein Protein: Myth or Reality? *J Nutr* **2021**, *151* (5), 1061–1072. DOI: 10.1093/jn/nxaa454 From NLM.
(7) Hegde, N. Research on A1 and A2 milk: A1 milk is not a matter of health concern. **2019**.
(8) Parashar, A.; Saini, R. A1 milk and its controversy-a review. **2019**, 4611–4619.
(9) Willett, W. C.; Ludwig, D. S. Milk and Health. *New England Journal of Medicine* **2020**, *382* (7), 644–654. DOI: 10.1056/NEJMra1903547.
(10) Cole, J. B.; Makanjuola, B. O.; Rochus, C. M.; van Staaveren, N.; Baes, C. The effects of breeding and selection on lactation in dairy cattle. *Anim Front* **2023**, *13* (3), 55–63. DOI: 10.1093/af/vfad044 From NLM.
(11) Chem, C. *Casein Rapid Test Pro II Kit [Lateral Flow]*. 1989. (accessed).
(12) Tessema, A.; Tibbo, M. *Milk quality control*; 2009. DOI: 10.13140/RG.2.1.2400.9200.
(13) Fuerer, C.; Jenni, R.; Cardinaux, L.; Andetsion, F.; Wagnière, S.; Moulin, J.; Affolter, M. Protein fingerprinting and quantification of β-casein variants by ultra-performance liquid chromatography–high-resolution mass spectrometry. *Journal of Dairy Science* **2020**, *103* (2), 1193–1207. DOI: https://doi.org/10.3168/jds.2019-16273.
(14) De Poi, R.; De Dominicis, E.; Gritti, E.; Fiorese, F.; Saner, S.; Polverino de Laureto, P. Development of an LC-MS Method for the Identification of β-Casein Genetic Variants in Bovine Milk. *Food Analytical Methods* **2020**, *13*. DOI: 10.1007/s12161-020-01817-0.
(15) Biosensis. *A1 Beta casein (A1), Bovine, ELISA assay*. 2006. (accessed).
(16) Indyk, H. E.; Gill, B. D.; Wood, J. E.; Chetikam, S.; Kobayashi, T. The determination of intact β-casein in milk products by biosensor immunoassay. *Journal of Food Composition and Analysis* **2021**, *101*, 103946. DOI: https://doi.org/10.1016/j.jfca.2021.103946.
(17) Cheng, S.; Yajie, Y.; Xiaoqin, N.; Juan, P.; and Lai, W. Fluorescent microspheres lateral flow assay for sensitive detection of the milk allergen casein. *Food and Agricultural Immunology* **2017**, *28* (6), 1017–1028. DOI: 10.1080/09540105.2017.1325841.
(18) Elferink, A. J. W.; Entiriwaa, D.; Bulgarelli, P.; Smits, N. G. E.; Peters, J. Development of a Microsphere-Based Immunoassay Authenticating A2 Milk and Species Purity in the Milk Production Chain. *Molecules* **2022**, *27* (10), 3199.
(19) Masoumeh Ghorbanpour, S.; Wen, S.; Kaitu'u-Lino, T. J.; Hannan, N. J.; Jin, D.; McClements, L. Quantitative Point of Care Tests for Timely Diagnosis of Early-Onset Preeclampsia with High Sensitivity and Specificity. *Angew Chem Int Ed Engl* **2023**, *62* (26), e202301193. DOI: 10.1002/anie.202301193 From NLM.
(20) Jarić, S.; Schobesberger, S.; Velicki, L.; Milovančev, A.; Nikolić, S.; Ertl, P.; Bobrinetskiy, I.; Knežević, N. Ž. Direct electrochemical reduction of graphene oxide thin film for aptamer-based selective and highly sensitive detection of matrix

metalloproteinase 2. *Talanta* **2024**, *274*, 126079. DOI: https://doi.org/10.1016/j.talanta.2024.126079.
(21) Alfawaz, A.; Alzahrani, K.; Niazy, A.; Alghamadi, H.; Lambarte, R.; Beagan, A.; Alfhaid, L.; Alotaibi, K.; Alswieleh, A. Smart Nanocarrier Based on Poly(oligo(ethylene glycol) methyl ether acrylate) Terminated pH-Responsive Polymer Brushes Grafted Mesoporous Silica Nanoparticles. *Applied Sciences* **2022**, *12* (7), 3688.
(22) Alotaibi, K. M.; Almethen, A. A.; Beagan, A. M.; Alfhaid, L. H.; Ahamed, M.; El-Toni, A. M.; Alswieleh, A. M. Poly(oligo(ethylene glycol) methyl ether methacrylate) Capped pH-Responsive Poly(2-(diethylamino)ethyl methacrylate) Brushes Grafted on Mesoporous Silica Nanoparticles as Nanocarrier. *Polymers* **2021**, *13* (5), 823.
(23) Maddahfar, M.; Wen, S.; Hosseinpour Mashkani, S. M.; Zhang, L.; Shimoni, O.; Stenzel, M.; Zhou, J.; Fazekas de St Groth, B.; Jin, D. Stable and Highly Efficient Antibody–Nanoparticles Conjugation. *Bioconjugate Chemistry* **2021**, *32* (6), 1146–1155. DOI: 10.1021/acs.bioconjchem.1c00192.
(24) Busch, R. T.; Karim, F.; Weis, J.; Sun, Y.; Zhao, C.; Vasquez, E. S. Optimization and Structural Stability of Gold Nanoparticle–Antibody Bioconjugates. *ACS Omega* **2019**, *4* (12), 15269–15279. DOI: 10.1021/acsomega.9b02276.

Statement of Contribution of Authors for Chapter 4

[2] Ziwei Wu, Yangjian Cai, Yitong Zhao, Mahnaz Maddahfar, Martin Sadraeian, Dayong Jin, Jiajia Zhou*, “Beads-on-a-Tip testing for ultrasensitive antigen detection across a large dynamic range”, ***Smart Molecules***, published

	Z.W	Y.C	Y.Z	M.M	M.S	D.J	J.Z
Experimental Design	●					●	●
Microscopy Set-up			●				
Sample Preparation	●	●		●	●		
Data Collection	●						
Data Analysis	●					●	●
Manuscript	●					●	●

The conceptual framework of this study was developed by my co-supervisor, Prof. Dayong Jin. The experimental design was carried out jointly by Prof. Jiajia Zhou and me. I conducted majority of experimental work, including surface modification of UCNPs, antibody bioconjugation, sample imaging, data collection, data analysis and manuscript writing.

Signatures from co-author:

Y.C: Production Note: Signature removed prior to publication.

Y.Z: Production Note: Signature removed prior to publication.

M.M: Production Note: Signature removed prior to publication.

M.S: Production Note: Signature removed prior to publication.

D.J: Production Note: Signature removed prior to publication.

J.J: Production Note: Signature removed prior to publication.

Chapters 4 are based on manuscripts submitted for publication. For consistency and coherence within this thesis, the content has been adapted and integrated into the thesis structure; therefore, these chapters do not strictly follow the journal article format.

Chapter 4. Beads-on-a-Tip Platform for SARS-CoV-2 Antigen Detection

Through the first project, we achieved a limit of detection of 61 pg/mL for milk protein, with a dynamic detection range extending from 1 pg/mL to 100 ng/mL. While these results demonstrate a high sensitivity for milk protein analysis, we identified two key factors that motivated a strategic shift in our platform development toward SARS-CoV-2 protein detection. Firstly, as detailed in Chapter 3, we conducted a comparative study of antibody binding efficiencies using sandwich ELISA for both milk proteins and SARS-CoV-2 antigens. The results revealed that the antibody pair targeting SARS-CoV-2 exhibited significantly higher binding efficiency than the milk-specific antibodies, which are mostly polyclonal and prone to lower specificity. Secondly, the practical requirements for milk protein detection generally do not necessitate an ultra-low LOD. In contrast, the detection of SARS-CoV-2 antigens demands extremely high sensitivity and a broader dynamic range. Achieving an ultra-low LOD is essential for accurate early-stage diagnosis, enabling timely medical intervention and contributing to improved disease management and public health outcomes. We have already used the LFIA for the milk protein in Chapter 3, however, they often have limitations in sensitivity, particularly when detecting low-abundance targets. To address this, we explored the integration of magnetic beads-based assays, which offer enhanced sensitivity and quantification capabilities compared to LFIAs. By combining the strengths of LFIA with the improved sensitivity of bead-based systems, we aim to overcome the limitations of LFIAs and develop a more sensitive platform for detecting low-concentration targets. This approach not only improves detection performance but also expands the potential applications of our technology in diagnostics and beyond.

4.1 Background

The COVID-19 pandemic underscores the urgent need for accurate, rapid diagnostics, as early antigen detection is key to effective patient care and transmission control. While PCR is highly accurate and widely regarded as the diagnostic gold standard[1,2], its time-intensive protocol, dependence on sophisticated laboratory equipment, and need for skilled technicians restrict its practicality in POCT in clinical settings or at home. The World Health Organization has recommended LFIAs for emergency use,

owing to their rapid turnaround time, affordability, and user-friendly[3], but their limited accuracy remains a concern particularly for detecting low-abundance antigens during the early stages of infection.

LFIAs typically rely on the porous membrane, i.e., nitrocellulose membrane, to generate capillary flow, which drives the transport of reporter nanoparticles and facilitates their interaction with analytes at conjugation pad and with capture antibodies at the test line[4,5]. LFIAs often suffer from the various forms of non-specific adsorption of reporter nanoparticles at the test line, including nanoparticles with and without active antibodies, as illustrated in Figure 1, as non-specific binding contributes to background noise, particularly when the analytes of target antigens are low-abundant, e.g. in the pico-gram range.

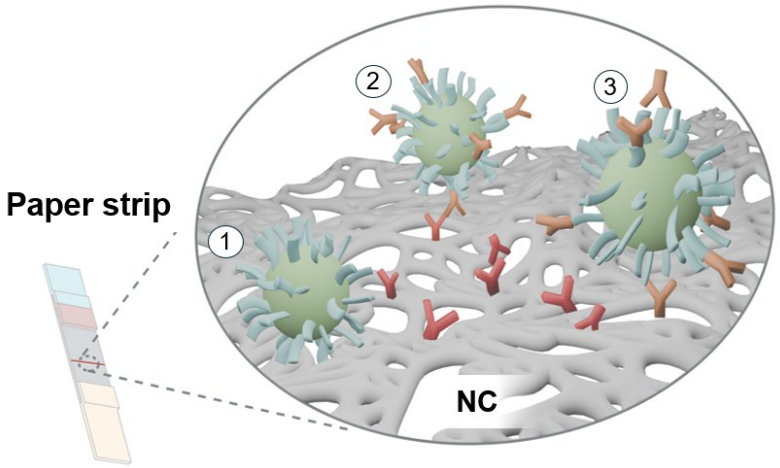

Figure 1. Schematic illustration of a paper strip–based test highlighting potential sources of non-specific adsorption at the test line on a nitrocellulose (NC) membrane. Non-specific signal may arise from 1) adsorption of nanoparticles lacking antibodies; 2) non-specific adsorption of nanoparticle-antibody conjugates by capture antibodies; and 3) entrapment of conjugates within the NC pore structure

To overcome these limitations, magnetic beads (MBs) have emerged as a promising alternative solid-phase support for immunoassays.[6, 7] As illustrated in the Figure 2, MBs can be functionalized with various chemical groups (e.g., –COOH, –NH_3, epoxy, CHO, tosyl)[8] to enable stable covalent attachment of diverse biomolecules such as antibodies, aptamers, peptides, and nucleic acids.[9] This versatility allows precise and specific surface engineering tailored to the target analyte. Additionally, MBs offer a

high surface-to-volume ratio for efficient biomolecule conjugation, superior colloidal stability for homogeneous reactions, and magnetic responsiveness for rapid separation and washing steps.[10] These features collectively contribute to improved SNR and enhanced assay sensitivity, which are particularly critical for the early detection of antigens present at ultra-low concentrations. The following section reviews recent advances in MBs-based immunoassay platforms and their applications in the detection of various protein biomarkers.

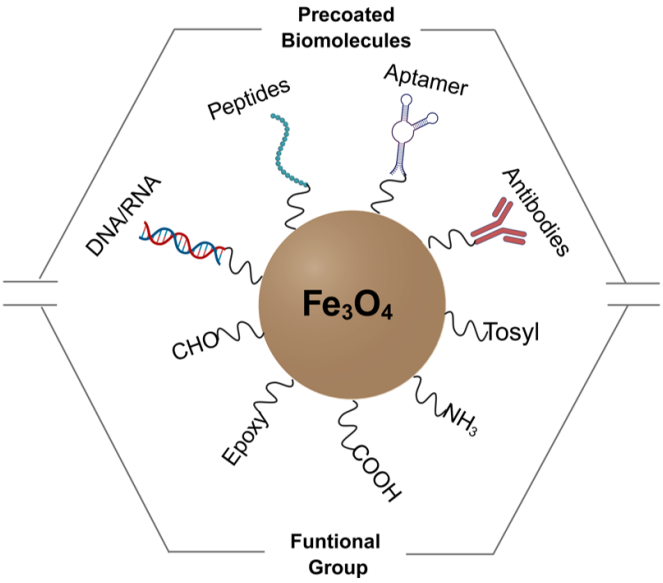

Figure 2. Surface functionalization of Fe_3O_4 magnetic beads for biomolecule conjugation.

4.2 The current research on the MBs-based assay

All the detection strategies summarized in Table 1 employ MBs as a key component within a sandwich immunoassay configuration and are further integrated with diverse analytical platforms to achieve highly sensitive and specific biomarker quantification. Among these, plate-based systems are the most commonly adopted due to their compatibility with conventional ELISA workflows while leveraging MBs to enhance washing efficiency and facilitate magnetic separation. In these formats, MBs function dually as capture substrates and solid phase supports, enabling effective isolation and preconcentration of target analytes from complex biological matrices. This approach has been shown to significantly improve assay performance, as evidenced by the consistently LOD reported in the table, often reaching into the sub-picogram to femtogram range, indicating the superior analytical sensitivity afforded by MB-

integrated platforms. However, some detection platforms often require complex instrumentation and precise operational procedures, which limit their suitability for point-of-care applications.

Table 1. Summary of advanced MBs-based sandwich immunoassay platforms for biomarkers

Method	**Target**	**Detector**	**LOD (ng/mL)**	**Ref**
MBs-ULISA	PSA	Upconversion scanner Upcon S-Pro	0.001	[11]
MBs-microfluidics	S protein	Magnetic modulation-enhanced LRET biosensor	0.0021	[12]
MBs-Single molecule array assays	S1 protein	Simoa HD-X Analyzer	0.005	[13]
MBs-Au	CEA protein	Chemiluminescence detector	0.0016	[14]
MBs-Surface plasmon resonance (SPR)	Brain natriuretic peptide	SPR instrument	0.025	[15]
MBs-microwell-based electrochemical sensor	Amyloid beta	Microelectrode array (MEA) biosensor	<0.00001	[16]

4.3 Design of Beads-on-a-Tip platform

To minimize non-specific binding induced inaccuracies and lower the limit of detection (LOD) while maintaining a rapid turnaround time, we here propose a pipette tip-based

homogenous assay platform (Beads-on-a-Tip, as shown in Figure 3a) that bridges the gap between PCR and conventional NC membrane-based LFIAs. In this work, plastic pipette tips were selected as the assay vessel to enable low-cost implementation and compatibility with scalable manufacturing. The tip serves primarily as a fluid-handling and magnetic confinement component rather than an active sensing interface, while the analytical signal originates from UCNP-labelled immunocomplexes associated with magnetic beads. This design ensures robustness, ease of operation, and suitability for point-of-care testing applications. In the Beads-on-a-Tip platform, we employ the magnetic beads (MBs) as the reaction subtract, and the upconversion nanoparticles (UCNPs) as the reporter.

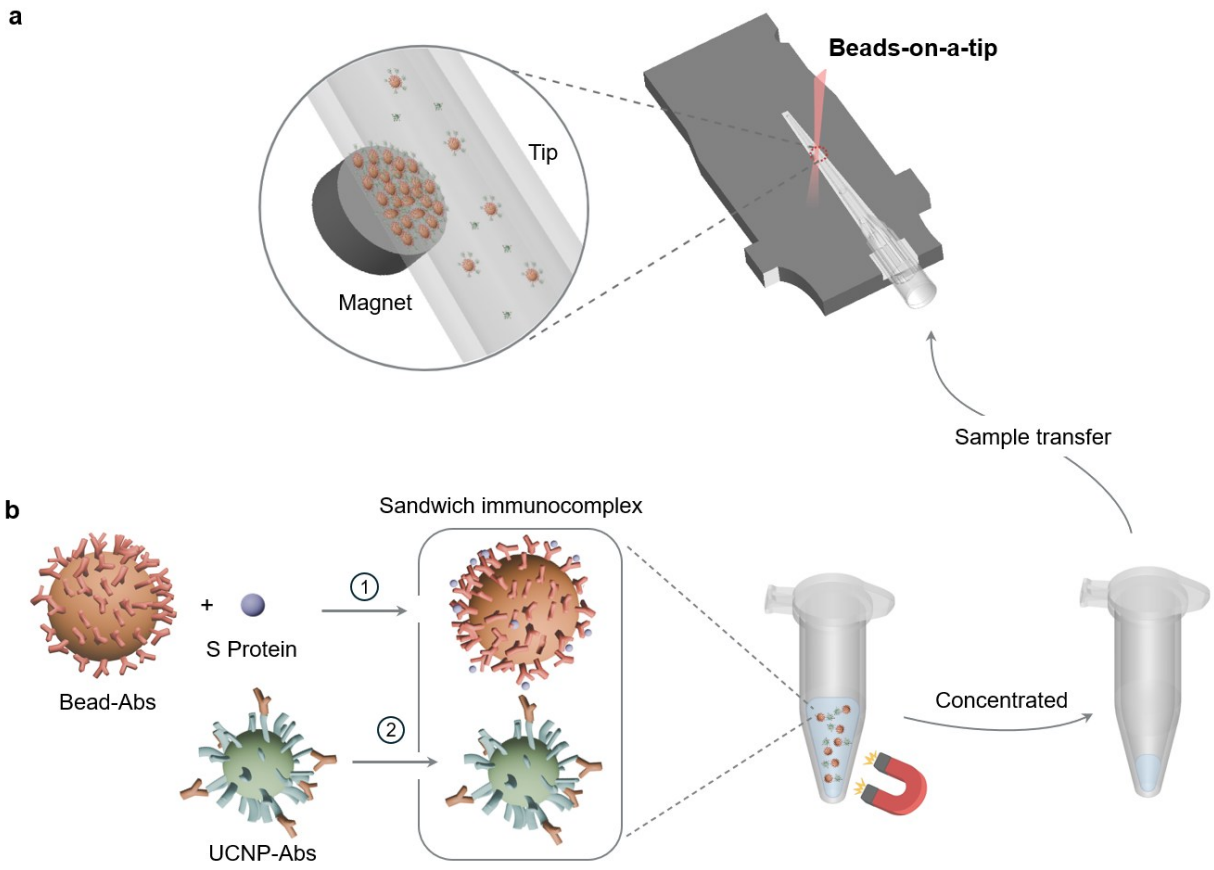

Figure 3. Schematic illustration of Beads-on-a-Tip platform and reaction process. a, Beads-on-a-Tip platform featuring magnetic capture and localized concentration of immunocomplexes for efficient detection; b, Formation of a sandwich immunocomplex, followed by magnetic washing to remove unbound components and volume condensation prior to transfer into the pipette tip.

Our Beads-on-a-Tip platform avoids the use of NC membranes by instead utilizing MBs. Rather than traditional paper-based strips, the entire assay is conducted within a 10 µL pipette tip inserted into a custom-designed cartridge (Figure 3a and Figure 4a). This setup enables optical readout using our portable detection reader, which shares the same optical path and software as the LFIA system described in Chapter 3, but utilizes a different sample holder. We further employed a magnet positioned beneath the tip (Figure 4b) to entrap the immunocomplex within a narrow region (As shown in Figure 3a). This entrapped region, which serves as the testing zone, is close to the focus of the 980 nm excitation laser beam in our detection reader, which has a beam diameter of 400 µm. The entire reaction process of 100 uL suspension was performed within disposable microtubes, which provides a homogenous reaction environment for reagents mixing. In this platform, as shown in Figure 3b, it utilized MBs conjugated with antibodies (MBs-Abs) to capture target antigens, which were subsequently recognized by UCNPs conjugated detection antibodies (UCNPs-Abs), forming a final sandwich-type immunocomplex (MBs-Abs-Ags-UCNPs-Abs). The washing procedures were applied by an external magnet to remove unbound and non-specifically bound components, followed by a suspension volume condense to 10 uL. After transferring the final immunocomplex into the pipette tip, magnetic enrichment concentrates the complexes at the test zone, ensuring that the laser excite the majority of MBs-bound immunocomplex while minimizing interference from excess unbound UCNP reagents remaining in the supernatant. The localized enrichment enables the signal amplification and significantly enhances detection sensitivity.

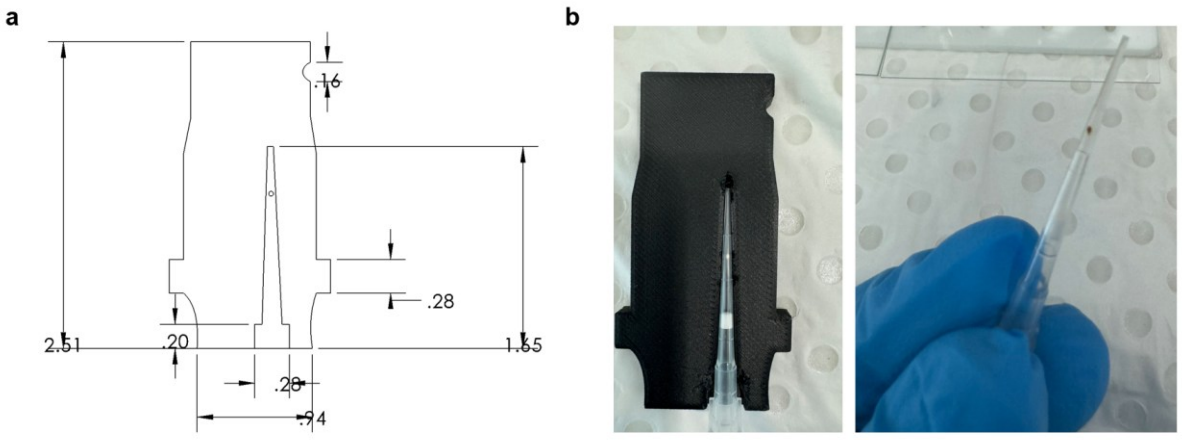

Figure 4. Scheme of Beads-on-a-Tip based platform design and implementation. a, CAD drawing of the Beads-on-a-Tip based holder (dimensions in cm); b, left: photo of

the platform setup, right: photos of conjugated MBs and supernatant separation using magnet

4.4 Experimental Section

4.4.1 Reagents and Buffers

The reagents and buffers used were the same as those described in Section 3.6.1.1 of Chapter 2, with the addition of Dynabeads™ M-270 Carboxylic Acid (14305D), purchased from Thermo Fisher, and the AnteoTech Nano Kit (A-PCKS), purchased from AnteoTech.

4.4.2 Antibodies and Antigens

The SARS-CoV-2 antibodies and antigens used in this study were the same as those described in Section 3.6.1.2 of Chapter 2.

4.4.3 Conjugation of omicron antibody on the surface of UCNPs-polymer (modified UCNP-Ab)

The conjugation of MBs–Abs was performed following the protocol described in Chapter 2.4.2.

4.4.4 Conjugation of MBs-Abs

The conjugation of MBs–Abs was performed following the protocol described in Chapter 2.4.3.

4.4.5 The procedure of ULISA assay

The microplate was coated with 5 μg of SARS-CoV-2 spike monoclonal antibody in 10 mM PBS and incubated overnight at 4 °C. The next day, the plate was washed three times with PBS containing 0.05% Tween-20 and then blocked with PBS with 2% BSA for 2 hours at room temperature. After blocking, the plate was washed again, followed by the addition of serial dilutions of antigens, which were incubated for 1 hour. The plate was then washed three times. Subsequently, UCNP-conjugated antibodies (omicron variant spike RBD) were diluted to 40 μg /mL with the storage buffer (10 Mm Tris buffer, pH 7.4, 150 mM NaCl, 1% BSA, 0.5% sucrose, 25 mM NaF, 1% Tween, 0.9% PVP) then added and incubated for another 1 hour. After a final washing step,

the plate was dried completely. The results were measured using a customized 980 nm microplate reader.

4.4.6 The fabrication of test strips and procedure of LFIA test

This lateral flow assay used only one T-line design. The test line area of the nitrocellulose membrane was sprayed with the antibody (0.125 mg/mL) using a dispenser and dried for approximately 1 hour at 35 °C. Then, the nitrocellulose membrane, conjugation pad, sample pad, and absorption pad were orderly mounted on the PVC back pad with 2 mm overlap. The assembled pads were cut into strips with a width of 3.3 mm and assembled in the cartridges.

In the strip testing, 1 μL of UCNP-Abs (1 mg/mL) was transferred to a 150 μL running buffer (10 mM Tris buffer, pH 7.6, with 1% BSA and 0.6% Tween-20) with different concentrations of the antigen (0, 0.001, 0.01, 0.1, 1, 10, 100, 1000 ng/mL). For the unwashed LFIA, after mixing the samples for 5 minutes, 50 μL of the sample solution was added to the sample pad of the strip. For the washed LFIA, after dropping 50 uL of sample solution, the strips were washed with 100 μL of running buffer. After 5 min, the strip was scanned the test line by our strip reader (Lasteck Photonic Technology Solutions, Australia) equipped with 980 nm laser. The emission intensity at 650 nm of the nanoprobes at the test line area of NC membrane was then analyzed.

4.4.7 Confocal and wide-field Microscope

An inverted confocal microscope (FV1200 Olympus) was combined with a self-built wide-field microscope connected to a butterfly FBG-stabilized 976 nm laser diode (900mW Thorlabs). The filter cube for the detection of Er^{3+}-doped UCNPs consisted of a dichroic mirror (980nm customised) and a short-pass filter (842nm Thorlabs). The images were acquired on an EMCCD camera (iXon Ultra 888 Andor), a 100x objective (1.45 NA Olympus) and a 40x objective (1.4 NA Olympus), which resulted in a power density of $3.2*10^4$ W/cm^2.

4.5 Characterization of UCNPs and MBs

4.5.1 Characterization of UCNPs-Abs

Core@shell structured UCNPs with the composition of β-NaYF4:40% Yb3+,4% Er3+@NaYF4 were synthesized using the co-precipitation method (The synthesis protocol followed the procedures described in Sections 2.1.1, 2.1.3 and 2.1.4 of Chapter 2). As observed under TEM in Figure 5a, the UCNPs exhibit a uniform spherical morphology with an average diameter of 43 nm. The monodispersity of UCNPs in cyclohexane is attributed to the surface-capping ligand, oleic acid (illustrated in green in Figure 5a). To render the UCNPs compatible with the aqueous phase, we synthesized a RAFT polymer as the new ligand (illustrated in blue in Figure 5b) to replace the oleic acid, following procedures was described in Section 2.2.2 in Chapter 2). After ligand exchange, the resulting UCNPs-polymer remained monodispersed in water, as observed by TEM. Although the polymer layer is not visible under TEM due to the low electron contrast of its constituent elements, its presence was confirmed by FTIR (shown in Section 2.2.2.3 in Chapter 2), DLS (Figure 5d), and zeta potential (Figure 5e) measurements. The surface-exposed -COOH groups of the polymer enable covalent coupling with -NH_2 groups on antibodies via EDC chemistry (See the detailed information from Section 2.3.2.2 in Chapter 2), resulting in UCNPs-Abs conjugates, as illustrated in Figure 5c. After this bioconjugation, the zeta potential of UCNPs increased from -22.4 to -16.8 mV and the hydrodynamic size increased from 58 nm to 149 nm. The observed broadening and increase in average particle size, along with the shift in surface charge, confirm the successful conjugation of antibodies onto the UCNP surface.

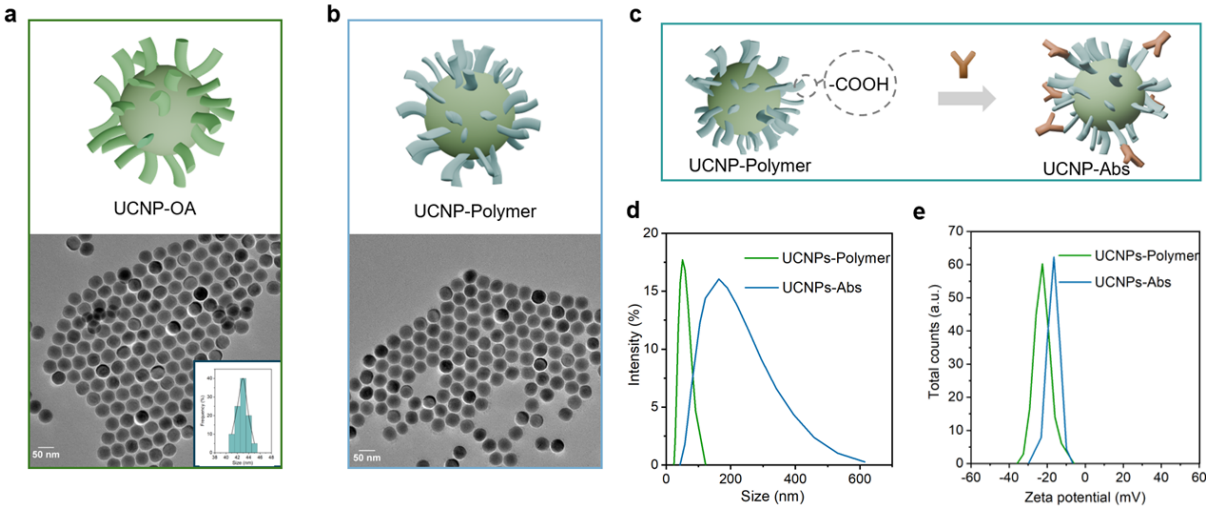

Figure 5. Characterizations to confirm formation of UCNPs-Abs. a, TEM image of the as-synthesized UCNPs with oleic acid surface; b, TEM image of the UCNPs after surface modification by using polymers; c, Polymer coating introduces -COOH groups on UCNPs, enabling covalent conjugation with antibodies to form UCNPs-Abs; d, DLS for UCNPs-polymer and UCNPs-Abs conjugates; e, Zeta potential for UCNPs-polymer and UCNPs-Abs conjugates.

4.5.2 Characterization of MBs-Abs

Similarly, MBs-Abs conjugates were prepared using the EDC coupling method (see Section 2.3.3 in Chapter 2). To determine the optimal antibody concentration that maximizes the average number of antibodies per bead with the aim of achieving the highest number of available reactive epitopes for the subsequent sandwich immunoreaction, a concentration gradient ranging from 0.005 µg to 2.5 µg per 12 µg of beads was evaluated (Figure 6a). The assessment was performed by adding a secondary antibody labelled with Alexa488, where the fluorescence intensity of Alexa per bead reflects the trend in the amount of active antibodies on the bead. Figure 1f shows a representative series of confocal images under 488 nm excitation. Statistical analysis of at least 50 beads per group revealed a saturation effect in the signal-to-noise ratio (SNR), defined as the emission intensity of Alexa488 per bead divided by the background noise. While between 0.005 µg and 1 µg of antibody input, the binding efficiency increased with the antibody concentration, a notable decrease in fluorescence intensity was observed when the antibody input exceeded 1 µg, likely due to the concentration quenching of Alexa dyes on the bead surface, rather than the possible antibody saturation[17], otherwise the fluorescence signal at 1.5 µg and 2 µg should have reached a plateau. In the following sections, when performing the Beads-on-a-Tip assay using 1 µg and 1.5 µg antibodies (Figure 6b), a lower LOD of 0.101 pg/mL was achieved by using 1 µg antibody, compared to a LOD of 0.883 pg/mL using 1.5 µg antibody.

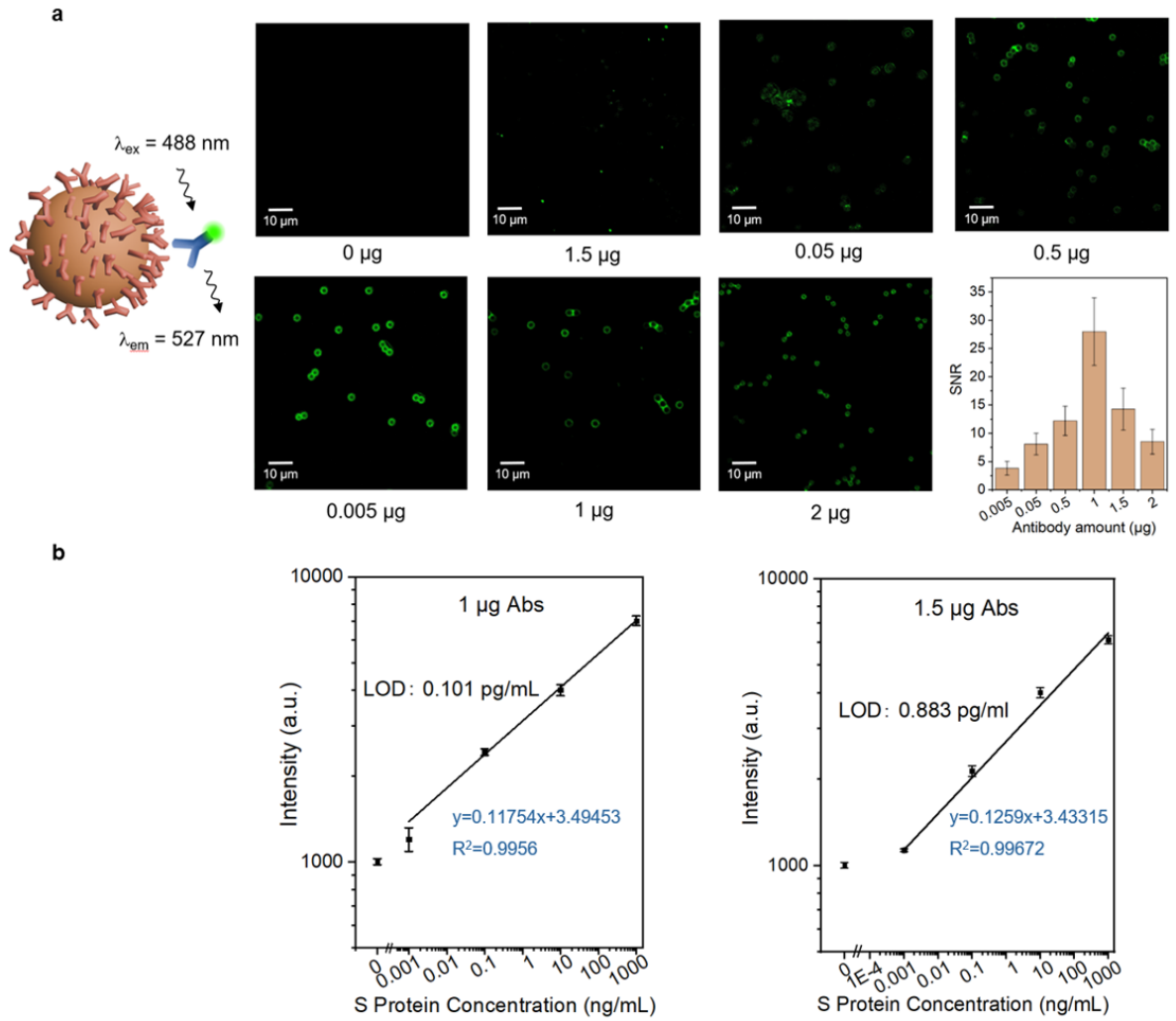

Figure 6. Characterization of antibody conjugation on MBs–Abs. a, Alexa488-labeled secondary antibodies were used to evaluate the amount of primary antibodies bound to the bead surface. Representative confocal images show varying fluorescence intensities per bead corresponding to different antibody input amounts (per 12 μg of beads). Statistical analysis was performed by quantifying the fluorescence intensity of at least 50 beads per group; b, Calibration curves obtained from Beads-on-a-Tip assay using 1 μg and 1.5 μg antibodies (n=3), with the corresponding fitting equations and coefficients of determination (R^2) shown in each condition

4.6 Optimization of Reaction Conditions for MBs-Based Immunoassay

4.6.1 Selection of Optimal Buffer System for Immunoassay Performance

To optimize the reaction conditions for the MBs-based immunoassay, we first compared three commonly used buffer systems, phosphate-buffered saline (PBS), phosphate buffer, and Tris buffer, under identical experimental conditions during Step 1, which involved the binding of target antigens to MBs-Abs conjugates (Figure 7). These buffers differ in ionic strength and buffering capacity, which can affect nanoparticle stability, antibody-antigen binding efficiency, and background signal. The results showed that both PBS and phosphate buffer produced consistently higher SNR values across all protein concentrations, indicating favorable conditions for specific binding and signal generation. In contrast, Tris buffer resulted in the lowest SNR, likely due to suboptimal ionic conditions that hindered immunoreactions. It should be noted that the comparison in Figure 7 reflects only the initial antigen-binding step (Step 1), during which UCNPs are not involved and the incubation time is relatively short. Under these conditions, the potential effects of buffer ionic strength on UCNP surface stability are not fully manifested.

Here, phosphate-based buffers were selected as the reaction medium to minimize the impact of buffer composition on the performance of UCNP-antibody conjugates in subsequent assays, while maintaining compatibility with the phosphate-mediated surface attachment of the polymer ligands. Unlike phosphate-buffered saline (PBS), simple phosphate buffers do not contain additional salts such as NaCl or KCl, which result in a lower overall ionic strength. This distinction is particularly important for UCNPs whose surface modification relies on coordination between phosphate functional groups and surface lanthanide ions. In PBS, the presence of free ions such as Na^+ and Cl^-, together with elevated ionic strength, can weaken phosphate-lanthanide coordination, potentially leading to ligand desorption, surface instability, or nanoparticle aggregation. Such effects are more pronounced for UCNPs bearing carboxylated or weakly bound polymer ligands, including PAA. This phenomenon has been reported by Himmelstoß et al., who showed that negatively charged UCNPs modified with surface ligands such as citrate, PAA, and phosphoglycerol (PG) exhibited reduced stability under high-ionic-strength conditions[18]. These considerations explain why phosphate buffer was chosen in this study to reduce the potential adverse effects associated with PBS on UCNP surface stability, thereby

improving colloidal robustness and assay reproducibility in downstream immunoassay procedures.

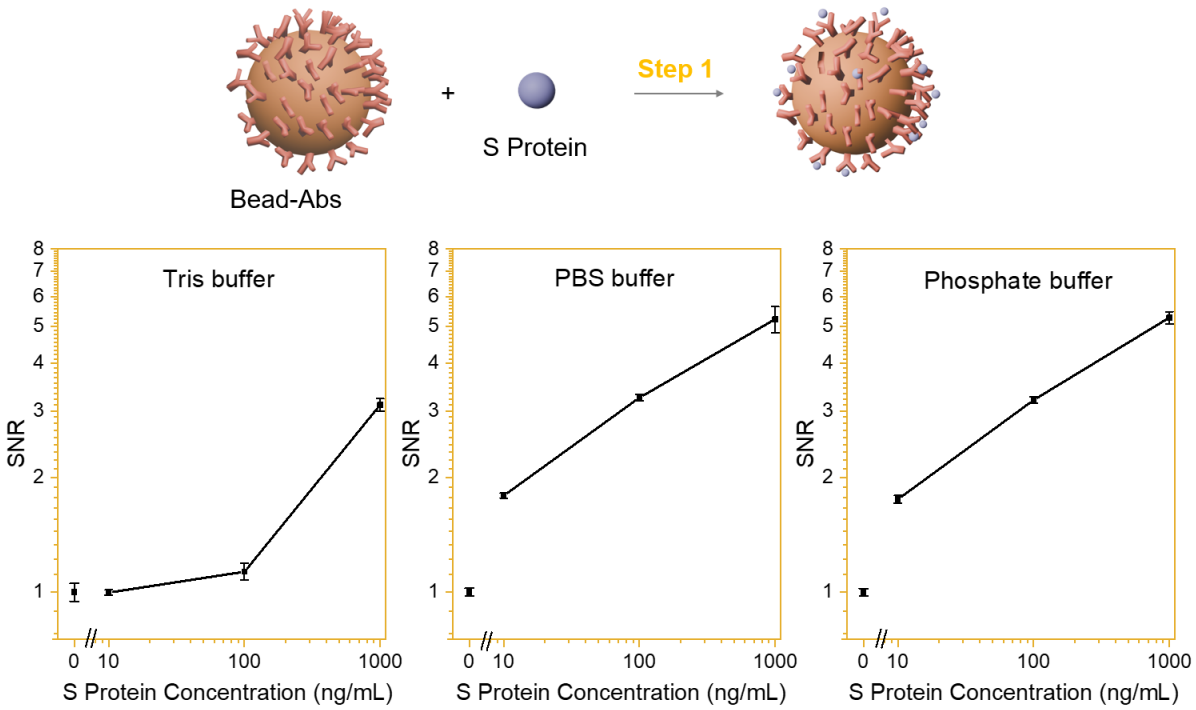

Figure 7. Evaluation of different buffer systems on the performance of MBs-Abs conjugates for protein detection (n=3). The schematic illustrates the binding of S protein to MBs-Abs during the step 1, while the plots compare the SNR responses obtained in Tris, PBS, and phosphate buffers at different antigen concentrations

4.6.2 Optimizing incubation time

In the bead suspension assays, the lower number of MBs will benefit the effective analyte enrichment, as higher concentration of analytes will be captured by the lower number of MBs, but it will require longer time for the limited number of beads to capture the analyte molecules onto the surface of MBs. To find a reasonable balance between the enrichment efficiency and the analyte enrichment time, as illustrated in Figure 8a, we performed and optimized a two-step reaction to form the sandwiched immunocomplex, including MBs-Abs capturing the antigen and UCNPs-Abs signal reporting. The incubation time was optimized to enhance antigen detection sensitivity, under a series of S antigen concentrations. Signal intensity increased consistently with

antigen concentration across all groups, indicating effective, concentration-dependent capture and detection. At the MBs concentration of 12 μg/mL used in our following experiments, 20 minutes incubation was found insufficient, and extending the incubation to 40 minutes can significantly enhance the signal strength, which established a clear linear relationship from 1 to 1000 ng/mL (Figure 8b). Negligible difference was observed for the incubation time between 40 and 60 minutes. Subsequently, at the UCNPs-Abs concentration of 1 mg/m, incubation durations for the UCNPs-Abs signal reporting step, at 1, 5, and 10 minutes, was investigated by fixing the MBs-Abs capturing incubation at the optimal 40-minute interval. As shown in Figure 8c, signal intensity increased rapidly from 1 minute to 5 minutes across all the antigen concentrations, with a clear linear relationship. However, extending the incubation to 10 minutes did not yield any significant improvement, compared to the 5-minute condition.

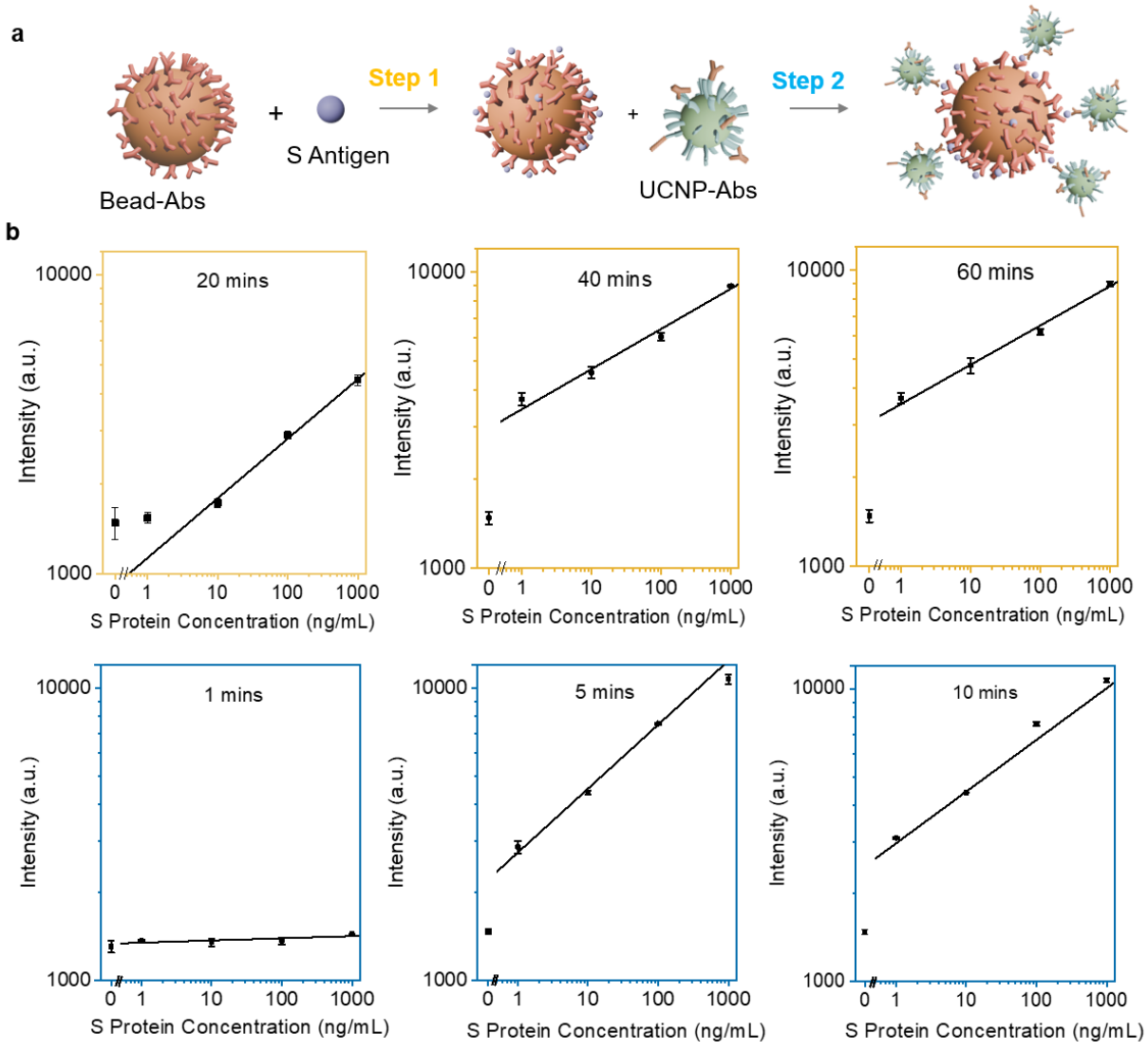

Figure 8. Optimization of incubation time for both MBs-Abs antigen capturing and UCNPs-Abs signal reporting steps. a, The process of the two-step formation of sandwich immunocomplexes; b, Signal response curves showing the effect of different incubation times (20, 40, and 60 minutes) with S antigen (n=3 in each time); c, Signal response curves showing the effect of different incubation times (1, 5, and 10 minutes) with UCNP-Abs (n=3 in each time).

4.6.3 Optimizing UCNPs-Abs to Beads-Abs ratio

UCNPs-Abs serve as signal reporters, which signal strength should be proportional to the levels of antigen analytes, and their ratio to beads-Abs plays a key role in modulating specific versus non-specific binding during the assay. This ratio ultimately influences the LOD, which determines the sensitivity of assay for detecting low-abundance antigens. To optimize the parameter, we varied the ratio of UCNPs-Abs to Beads-Abs in Step 2 by testing 1 μg, 5 μg, and 10 μg of UCNPs-Abs against a fixed amount of 2.4 μg Beads-Abs. The assay was then performed across a broad range of antigen concentrations, from 0.0001 to 10,000 ng/mL, with results shown in Figure 9.

With 1 μg of UCNPs-Abs, the assay exhibited limited upconversion response at lower antigen concentrations, with appreciable signal only at the concentrations higher than 10 ng/mL. This indicates that the limited amount of UCNPs-Abs conjugates was insufficient for effective target recognition and signal readout, resulting in a relatively high LOD of 4100 pg/mL. LOD in this work is defined as the target concentration where the intensity is equal to the sum of the background noise and three times the standard deviation above the background noise[19, 20]. Increasing the number of UCNPs-Abs conjugates to 5 μg and 10 μg has significantly extended the detectable range, reaching down to the femtogram level. The enhanced upconversion signal at each antigen concentration suggests that a greater number of UCNPs-Ab conjugates successfully bound to target antigens, thereby improving the assay's ability to detect trace analyte levels. This led to improved LODs of 0.706 pg/mL and 0.738 pg/mL for the 5 μg and 10 μg conditions, respectively. The slightly higher LOD observed with the 10 μg condition is attributed to increased non-specific binding, as evidenced by elevated signal intensities in the control samples. Therefore, 5 μg of UCNPs-Aba conjugates was chosen in our protocol. Then, the repeatability of the assay under the final

optimized conditions was evaluated through three independently performed experiments using the same batch of UCNPs. The DLS and zeta-potential measurements of both polymer-modified and antibody-conjugated UCNPs showed minimal variation among the three replicates (Figure 10). Despite slight variations in signal intensity, the three independent replicates demonstrated good reproducibility of the assay (Figure 11). In the future real sample measurements, a blank control can be first tested to define the baseline signal. Given the established linear calibration relationship under the optimized conditions, the concentration of the unknown sample can then be approximately estimated accordingly.

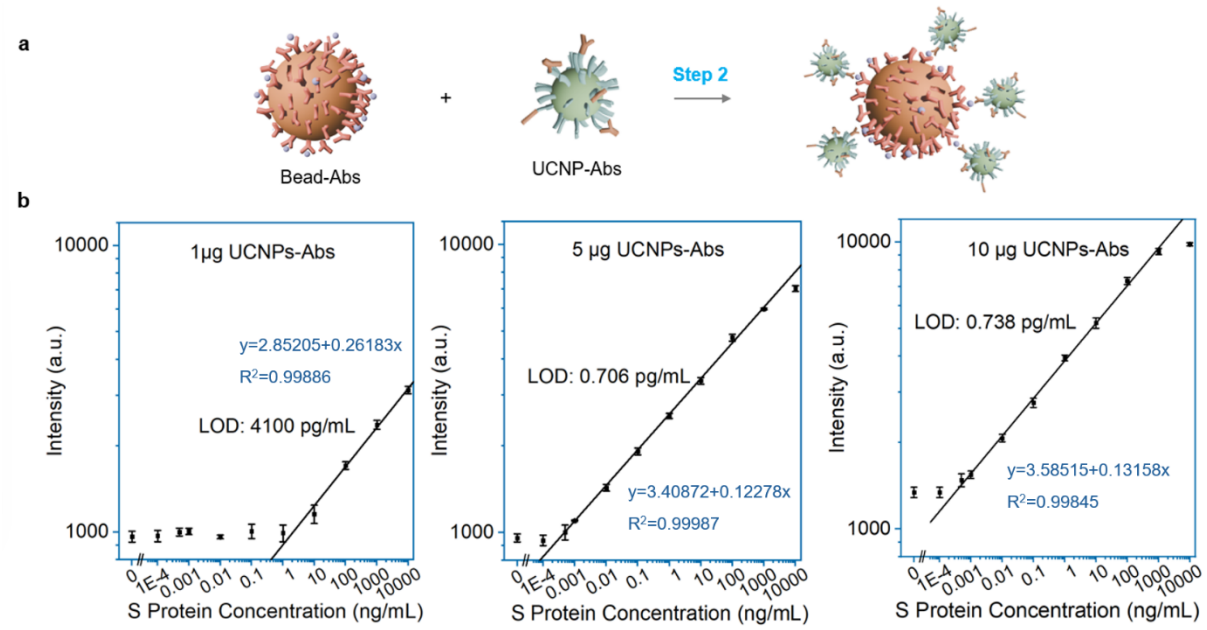

Figure 9. Effect of varying UCNP-Ab concentrations on S protein detection. a, The illustration of the second step in sandwich immunocomplex formation; b, Calibration curves for S protein detection using 1 μg, 5 μg, and 10 μg of UCNPs-Abs (n=10 in each variant). Black lines represent linear regression fits within the indicated concentration ranges, with the corresponding fitting equations and coefficients of determination (R^2) shown in each condition

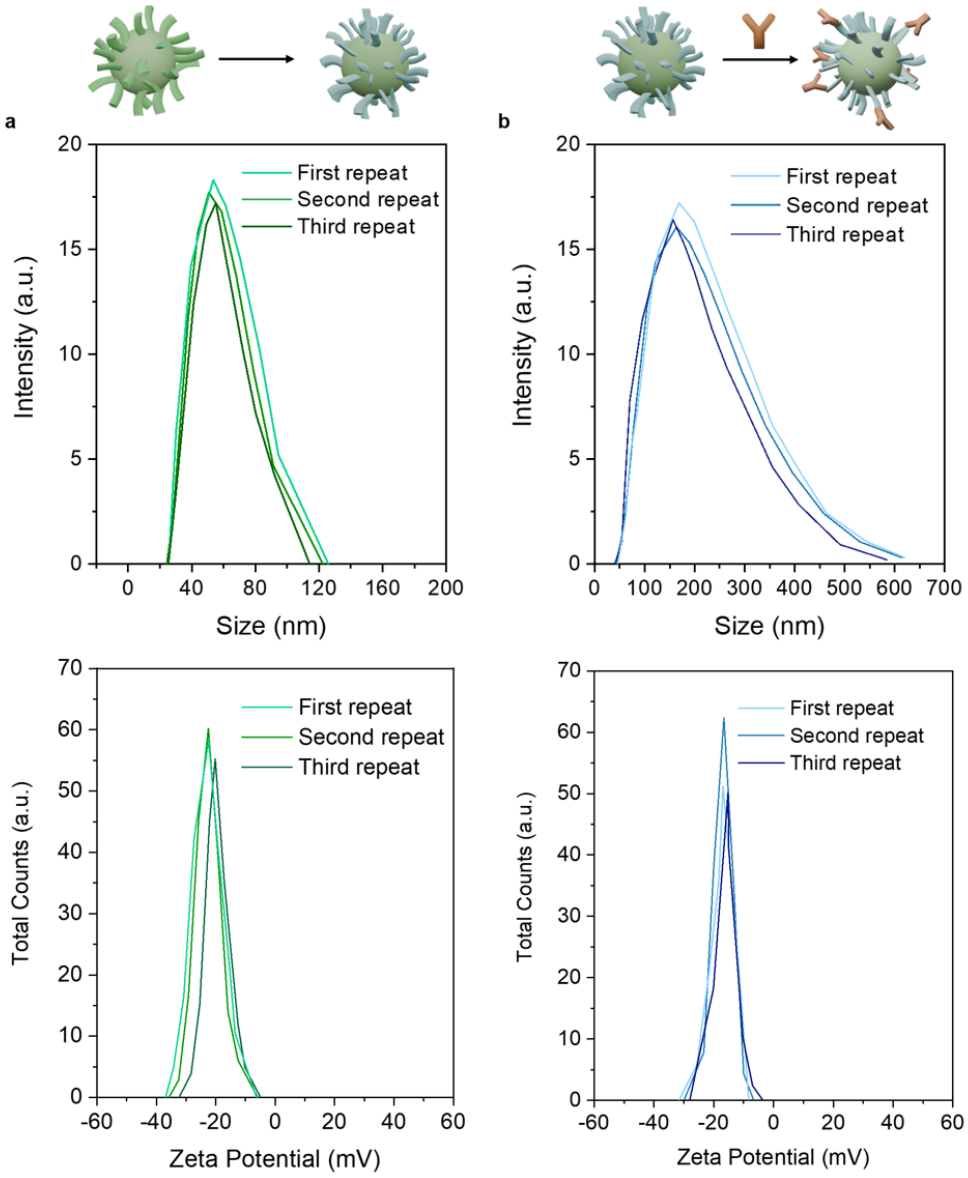

Figure 10. Repeatability of polymer modification and antibody bioconjugation on UCNPs (n=3). a, DLS and zeta-potential measurements of polymer-modified UCNPs; b, DLS and zeta-potential measurements of antibody-conjugated UCNPs

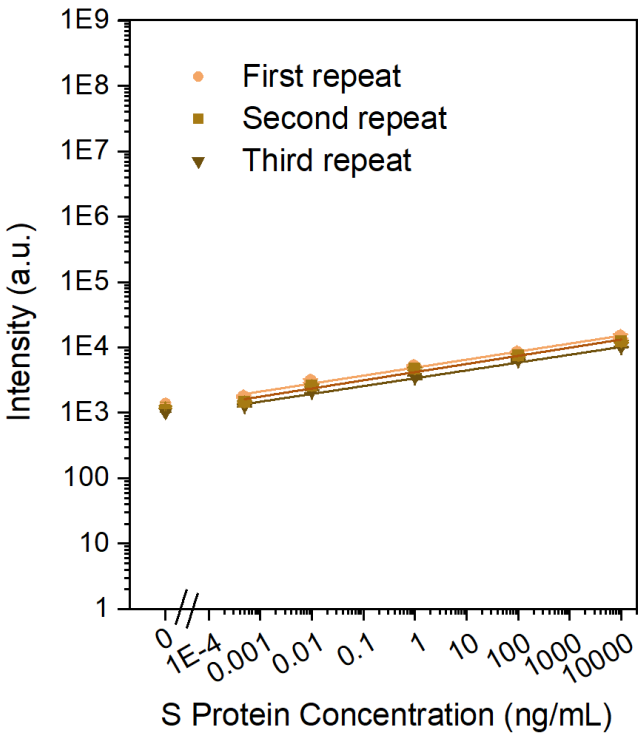

Figure 11. Calibration curves from three independent replicates of the beads-based assay (n=3).

4.7 Performance comparison with alternative detection strategies

Wide-field imaging using a custom-designed microscope with 980 nm laser excitation provides a sensitive and informative approach, allowing visualization of signals from individual beads as well as the homogeneity of the formed sandwich immunocomplexes. Accordingly, we performed imaging of dried immunocomplexes dispersed on a cover glass for all three groups presented in Figure 12. The fluorescence signals corresponding to immunocomplex formation on individual beads were observed with increasing antigen concentrations. Minimal background fluorescence was observed in the negative controls (0 ng/mL) for all groups, confirming the minimal non-specificity of signal generation. The results closely matched those obtained from the Beads-on-a-Tip platform: the 5 µg UCNPs-Abs group demonstrated the best performance, with a calculated LOD of 0.746 pg/mL, as shown in Figure 10a. In comparison, the 10 µg group achieved an LOD of 0.779 pg/mL, while the 1 µg group showed a significantly higher LOD of 200 pg/mL (Figure 10c). Representative imaging results for the 5 µg UCNPs-Abs group across a wide antigen

concentration range (0 to 10,000 ng/mL) are shown in Figure 10b, confirming that individual beads exhibit homogeneous upconversion signals. Altogether, it is reasonable to conclude that our Beads-on-a-Tip method is as sensitive as the imaging-based approach. However, the former is more suitable for POCT, offering a one-go signal readout, while the latter relies on advanced imaging microscopy and statistical analysis of a large number of beads to determine the signal of a sample.

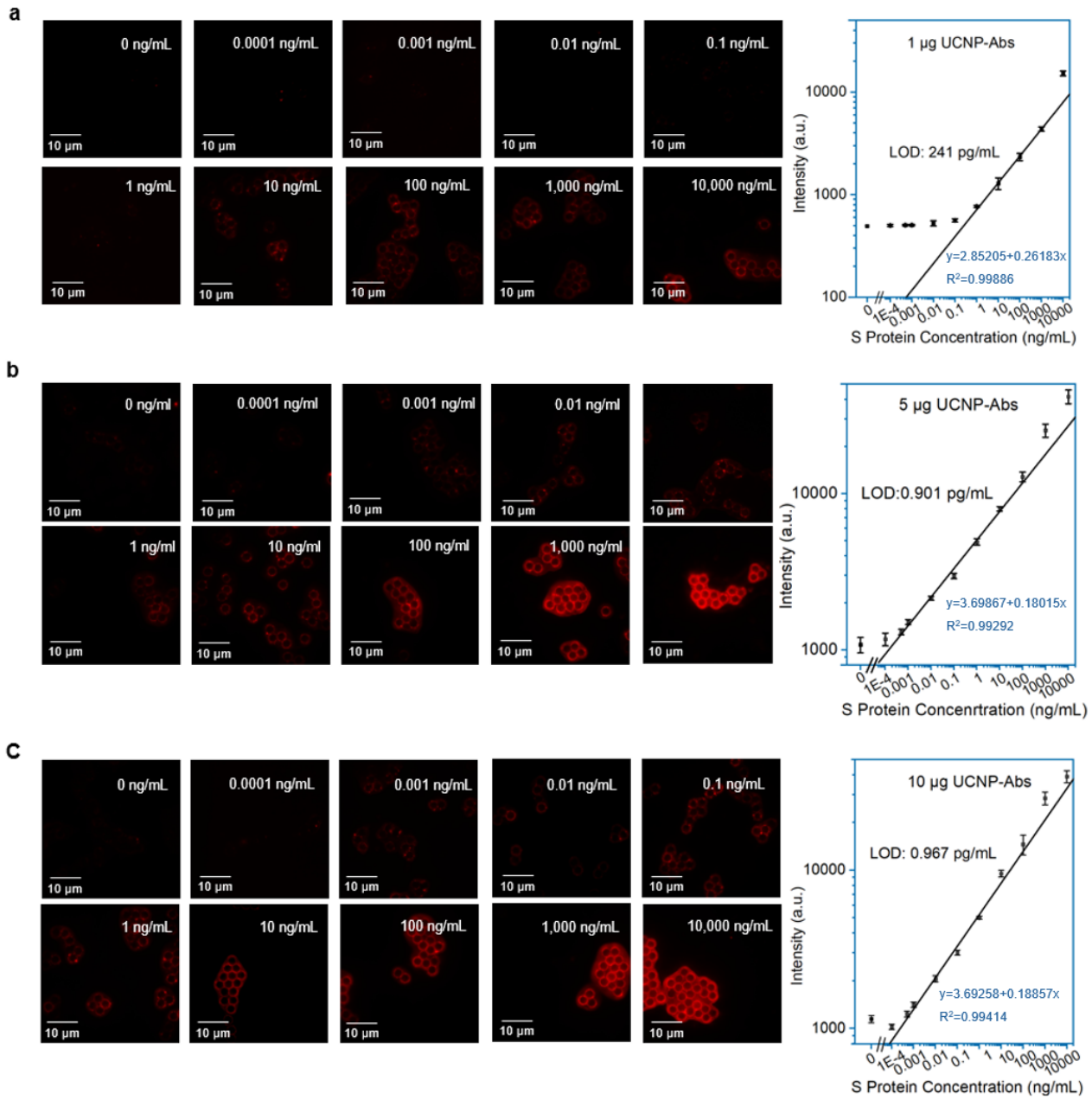

Figure 12. Fluorescence imaging under 980 nm wide-field imaging system and calibration curve of sandwich ifmmunocomplexes at varying protein concentrations

using 1 µg (a) 5 µg (b) and 10 µg (c) of UCNPs-Abs conjugates (n=100 MBs conjugates in each variant)

To evaluate whether the use of Beads-Abs as the substrate offers the expected advantages of signal concentration and active washing by extracting target products at each step, we performed the assay using a microplate-based upconversion enzyme-linked immunosorbent assay (ULISA, Figure 13a and 13c). In the ULISA, the formed Abs-Ag-UCNPs-Abs sandwich immunocomplexes are randomly immobilized on the bottom of the well plate, and washing is performed passively by removing unbound species. Otherwise, ULISA provides a homogeneous liquid-phase assay environment with sufficient incubation time, similar to that used in the Beads-on-a-Tip platform. The results, shown in Figure 13a, demonstrate a LOD of 6.45 pg/mL via ULISA, which is approximately three times higher than that achieved with the Beads-on-a-Tip.

As the Beads-on-a-Tip platform is designed for POCT, it is important to evaluate its performance in comparison with conventional methods such as paper-based LFIA. To ensure sufficient binding, an off-line reaction between the UCNPs-Abs conjugates and target antigens was first carried out, followed by application of the reaction products onto the paper strip for lateral flow testing. Signal detection was performed at the test (T) line. The detector is shown in Figure 13d. The best achievable LOD is shown in Figure 13b, reaching 6.53 pg/mL after a single wash with pure buffer. This represents a slight improvement compared to the LFIA result without washing, which showed an LOD of 9.72 pg/mL (Figure 14). These results suggest that subsequent passive washing has minimal effect in removing species responsible for non-specific binding.

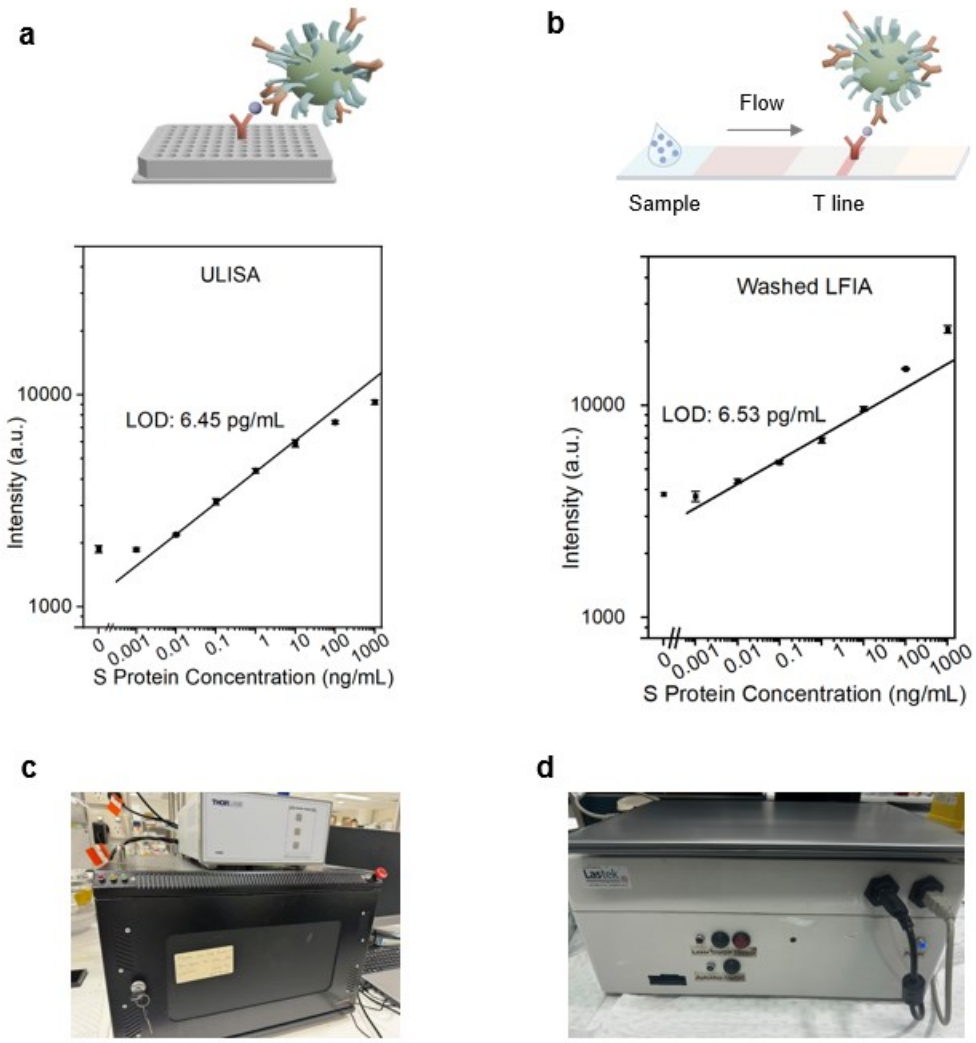

Figure 13. Comparative analysis of assay performance across ULISA and washed LFIA. a, The calibration curves for S antigen detection of ULISA (n=10); b, The calibration curves for S antigen detection of washed LFIA (n=10); c, ULISA microplate reader; d, Strip reader for LFIA

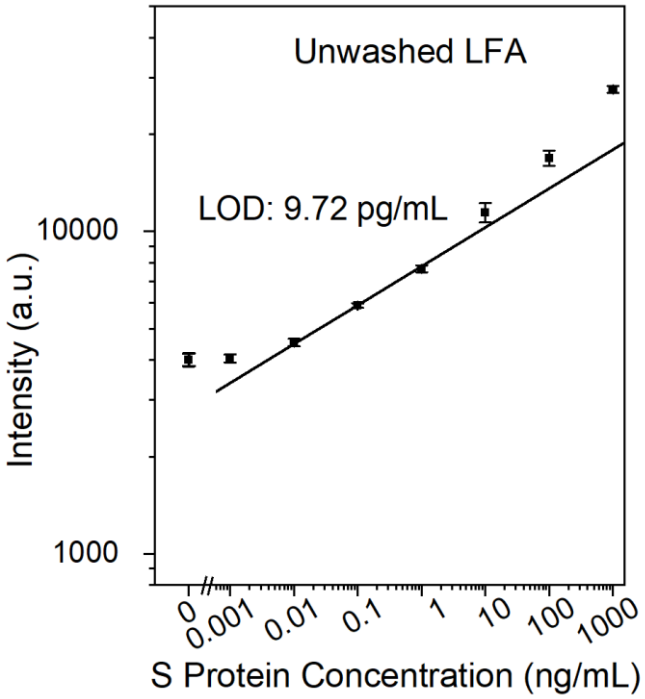

Figure 14. The result of the LFIA without washing (n=10 in each variant).

4.8 Analysis of achieved performance relative to literature benchmarks

Table 2. Comparison of the analytical performance of various immunoassay platforms, including LFIA-based methods, microwell plate assays, wide-field imaging, and our Beads-on-a-Tip system. The table summarizes the detection range, LOD and point-of-care applicability for each method.

Methods	Detection range	LOD (pg/mL)	Point-of-care	Ref
LFIA	10 pg/mL -1 µg/mL	6.53	Yes	Our Work
	1 ng/mL -1 µg/mL	38		[21]
	0.05 ng/mL - 1 µg/mL	33		[22]
Microwell plate	10 pg/mL - 1 µg/mL	6.45	No	Our Work
	1 pg/mL -100 ng/mL	1.3		[23]
	Up to 10 ng/mL	30		[24]

Imaging	500 fg/mL- 10 µg/mL	0.901		Our Work
	100 fg/mL -100 ng/mL	2.7	No	[23]
	200 fg/mL - 20 µg/mL	0.00073		[25]
Beads-on-tip	**500 fg/mL - 10 µg/mL**	**0.706**	**Yes**	**Our Work**

Table 2 summaries the analytical performance of LFIA, microwell plate-based, imaging, and Beads-on-a-Tip methods achieved in this study, and compares the representative works reported by other groups in (SARS-CoV-2) antigen detection, in terms of the detection range, LOD and point-of-care applicability.

In LFIA, Oh et al. reported a strategy involving the formation of plasmon color-preserved (PLASCOP) AuNP clusters by assembling streptavidin-coated gold nanoparticle (AuNP) cores with satellite AuNPs functionalized with biotinylated antibodies[21]. This configuration achieved a LOD of 38 pg/mL in detecting N antigen. In another study, Han et al. created a SiO_2@Au/quantum dots hybrid structure, in which quantum dots and AuNPs were co-assembled onto a silica core to enable dual-mode colorimetric and fluorescent signal readout, resulting in a LOD of 33 pg/mL in detecting S antigen[22]. By using UCNPs as the reporter, we have recently advanced the design of a geometric paper strip that minimizes the immunoreaction area for antigen detection achieving a LOD of 10 pg/mL[26] and a LOD of 6.53 pg/mL in detecting N and S antigen analytes, respectively.

Microwell plate-based setup offers longer incubation times for sandwich immunoreactions and suitable for washing steps. Huang et al. reported a one-step assay using nanoplasmonic sensors integrated into standard 96-well microplates, achieving a LOD of approximately 370 virus particles/mL, corresponding to about 30 pg/mL of N antigen[24]. Gorris et al. developed a ULISA system that combined UCNPs with biotinylated antibody pairs in a conventional sandwich immunoassay format, achieving a LOD of 1.3 pg/mL and a broad dynamic range from 1 pg/mL to 100 ng/mL in detecting N antigen[23]. Similarly, our ULISA setup has achieved a comparable LOD of about 6.45 pg/mL in this work.

Fluorescence imaging can achieve exceptional sensitivity towards a single-molecule sensitivity. Gorris et al. examined a microscopic imaging approach based on the same immunocomplexes formed in the above mentioned microplate wells, achieving a LOD of 2.7 pg/mL[23]. Compared to the upconversion microplate reader used in their ULISA format, the imaging-based readout yielded approximately two-fold higher signal intensity, along with an extended detection range that reached down to a level of 100 fg/mL. Li et al. reported a novel fluorescence-linked immunosorbent assay (FLISA) based on streptavidin-modified transparent 96-well microplates and carboxylated fluorescent microsphere-conjugated monoclonal antibodies by wide-field fluorescence microscopy, resulting in an exceptionally low LOD of 0.00073 pg/mL for SAS-Cov-2 N antigen detection and a broad detection range of 0.02 pg/mL - 20 µg/mL, with the saturation point at 200 ng/mL[25]. According to the report, the high sensitivity was attributed to the use of biotinylated antibodies and the surface treatment of the microplates by the plasma and subsequent streptavidin modification that increases the binding efficiency of biotinylated capture antibodies while maintaining immunoreactivity.

In our work here, magnetic beads can enrich analytes and the immunofluorescence assays conducted in the suspension facilitates the long-term stability of conjugates. By replacing the nitrocellulose membrane with beads in a tip, the active washing overcomes the limitation of the passive capillary fluidics in nitrocellulose membranes that are often associated with non-specific bindings and high background noise, as well as reporting nanoparticles' aggregation and their loss in the binding efficiency. Despite a LOD of 0.901 pg/mL achieved by the following fluorescence imaging, the system requires a bulky microscope, hard for POCT applications.

4.9 Conclusion

The Beads-on-a-Tip system developed in this work achieved a broad dynamic range (500 fg/mL to 10 µg/mL) and a low LOD of 0.706 pg/mL, representing a substantial sensitivity improvement over conventional LFIAs and microwell-based methods. Notably, this platform technology takes advantage of the high sensitivity and low non-specific binging of imaging approaches and the applicability of LFIAs towards more

accurate and quantitative POCT. Future work will improve the conjugate stability through optimized surface chemistry and storage strategies, as well as incorporating automated fluid handling with active washing to enhance robustness and reproducibility in the assay. Moreover, the successful clinical performance previously achieved with our UCNP-LFIA in real saliva samples further supports the strong clinical potential of the Beads-on-a-Tip system, given its markedly broader detection range and substantially lower LOD.

4.10 Perspective

The successful integration of magnetic bead-based immunoassays with the Beads-on-a-Tip platform and UCNP-based detection offers a promising foundation for the development of next-generation point-of-care diagnostic technologies. In the future, this system could be further enhanced by incorporating smartphone-based reader for portable, low-cost, and user-friendly signal readout, facilitating broader deployment in resource-limited settings. Additionally, the tip platform may be engineered into a multi-channel microfluidic system, enabling all assay steps, including target capture, washing, and signal generation, to be conducted entirely within the pipette tip, without the need for separate microtubes. This tip-integrated microfluidics would not only simplify the workflow but also significantly reduce reagent volume, thereby lowering operational costs. In addition, it minimizes sample loss, reduces contamination risk, and facilitates automation and multiplexing.

Reference

(1) Udugama, B.; Kadhiresan, P.; Kozlowski, H. N.; Malekjahani, A.; Osborne, M.; Li, V. Y. C.; Chen, H.; Mubareka, S.; Gubbay, J. B.; Chan, W. C. W. Diagnosing COVID-19: The Disease and Tools for Detection. *ACS Nano* **2020**, *14* (4), 3822–3835. DOI: 10.1021/acsnano.0c02624.
(2) Garzarelli, V.; Chiriacò, M. S.; Cereda, M.; Autuori, I.; Ferrara, F. Miniaturized Real-Time PCR systems for SARS-CoV-2 detection at the Point-of-Care. *Clin Chim Acta* **2022**, *536*, 104–111. DOI: 10.1016/j.cca.2022.09.014 From NLM.
(3) Organization, W. H. *Use of SARS-CoV-2 antigen-detection rapid diagnostic tests for COVID-19 self-testing.* 2022. https://www.who.int/publications-detail-redirect/WHO-2019-nCoV-Ag-RDTs-Self_testing-2022.1 (accessed).
(4) Bahadır, E. B.; Sezgintürk, M. K. Lateral flow assays: Principles, designs and labels. *TrAC Trends in Analytical Chemistry* **2016**, *82*, 286–306. DOI: https://doi.org/10.1016/j.trac.2016.06.006.

(5) Bezinge, L.; Shih, C.-J.; Richards, D. A.; deMello, A. J. Electrochemical Paper-Based Microfluidics: Harnessing Capillary Flow for Advanced Diagnostics. *Small* **2024**, *20* (38), 2401148. DOI: https://doi.org/10.1002/smll.202401148.
(6) Cheng, H. P.; Yang, T. H.; Wang, J. C.; Chuang, H. S. Recent Trends and Innovations in Bead-Based Biosensors for Cancer Detection. *Sensors (Basel)* **2024**, *24* (9). DOI: 10.3390/s24092904 From NLM.
(7) Chen, J.; Wang, M.; Li, S.; Ye, J.; Li, L.; Wu, Y.; Cai, D.; Liu, T.; Zhu, L.; Shao, Y.; et al. Well-oriented immobilized immunoaffinity magnetic beads for detection of fumonisins in grains and feeds via pre-column automatic derivatization of high-performance liquid chromatography. *Food Chemistry* **2023**, *422*, 136226. DOI: https://doi.org/10.1016/j.foodchem.2023.136226.
(8) Wang, L.; Lin, J. Recent advances on magnetic nanobead based biosensors: From separation to detection. *TrAC Trends in Analytical Chemistry* **2020**, *128*, 115915. DOI: https://doi.org/10.1016/j.trac.2020.115915.
(9) Paleček, E.; Fojta, M. Magnetic beads as versatile tools for electrochemical DNA and protein biosensing. *Talanta* **2007**, *74* (3), 276–290. DOI: https://doi.org/10.1016/j.talanta.2007.08.020.
(10) You, M.; Li, Z.; Zhang, P.; Bai, D.; Lin, M.; Xu, F. Chapter 11 - Nanomaterial- and Micromaterial-Based Immunoassays. In *Handbook of Immunoassay Technologies*, Vashist, S. K., Luong, J. H. T. Eds.; Academic Press, 2018; pp 273–304.
(11) Sklenárová, D.; Hlaváček, A.; Křivánková, J.; Brandmeier, J. C.; Weisová, J.; Řiháček, M.; Gorris, H. H.; Skládal, P.; Farka, Z. Single-molecule microfluidic assay for prostate-specific antigen based on magnetic beads and upconversion nanoparticles. *Lab on a Chip* **2024**, *24* (14), 3536–3545, 10.1039/D4LC00346B. DOI: 10.1039/D4LC00346B.
(12) Otieno, B. A.; Krause, C. E.; Latus, A.; Chikkaveeraiah, B. V.; Faria, R. C.; Rusling, J. F. On-line protein capture on magnetic beads for ultrasensitive microfluidic immunoassays of cancer biomarkers. *Biosens Bioelectron* **2014**, *53*, 268–274. DOI: 10.1016/j.bios.2013.09.054 From NLM.
(13) Ogata, A. F.; Maley, A. M.; Wu, C.; Gilboa, T.; Norman, M.; Lazarovits, R.; Mao, C.-P.; Newton, G.; Chang, M.; Nguyen, K.; et al. Ultra-Sensitive Serial Profiling of SARS-CoV-2 Antigens and Antibodies in Plasma to Understand Disease Progression in COVID-19 Patients with Severe Disease. *Clinical Chemistry* **2020**, *66* (12), 1562–1572. DOI: 10.1093/clinchem/hvaa213 (accessed 7/12/2025).
(14) Li, M.; Sun, Y.; Chen, L.; Li, L.; Zou, G.; Zhang, X.; Jin, W. Ultrasensitive Eletrogenerated Chemiluminescence Immunoassay by Magnetic Nanobead Amplification. *Electroanalysis* **2010**, *22* (3), 333–337. DOI: https://doi.org/10.1002/elan.200900351.
(15) Teramura, Y.; Arima, Y.; Iwata, H. Surface plasmon resonance-based highly sensitive immunosensing for brain natriuretic peptide using nanobeads for signal amplification. *Analytical Biochemistry* **2006**, *357* (2), 208–215. DOI: https://doi.org/10.1016/j.ab.2006.07.032.
(16) Roy, S.; Kang, S.; Choi, K. Y.; Lee, K. H.; Shin, K.-S.; Kang, J. Y. Implementation of an ultra-sensitive microwell-based electrochemical sensor for the detection of Alzheimer's disease. *Biosensors and Bioelectronics* **2024**, *247*, 115898. DOI: https://doi.org/10.1016/j.bios.2023.115898.
(17) Huang, A.; Li, W.; Shi, S.; Yao, T. Quantitative Fluorescence Quenching on Antibody-conjugated Graphene Oxide as a Platform for Protein Sensing. *Scientific Reports* **2017**, *7* (1), 40772. DOI: 10.1038/srep40772.

(18) Himmelstoß, S. F.; Hirsch, T. Long-Term Colloidal and Chemical Stability in Aqueous Media of NaYF4-Type Upconversion Nanoparticles Modified by Ligand-Exchange. *Particle & Particle Systems Characterization* **2019**, *36* (10), 1900235. DOI: https://doi.org/10.1002/ppsc.201900235.
(19) Mendez-Gonzalez, D.; Silva-Ibáñez, P. P.; Valiente-Dies, F.; Calderón, O. G.; Mendez-Gonzalez, J. L.; Laurenti, M.; Egatz-Gómez, A.; Díaz, E.; Rubio-Retama, J.; Melle, S. Oligonucleotide sensor based on magnetic capture and photoligation of upconverting nanoparticles in solid surfaces. *J Colloid Interface Sci* **2021**, *596*, 64–74. DOI: 10.1016/j.jcis.2021.02.093 From NLM.
(20) Mendez-Gonzalez, D.; Lahtinen, S.; Laurenti, M.; López-Cabarcos, E.; Rubio-Retama, J.; Soukka, T. Photochemical Ligation to Ultrasensitive DNA Detection with Upconverting Nanoparticles. *Analytical Chemistry* **2018**, *90* (22), 13385–13392. DOI: 10.1021/acs.analchem.8b03106.
(21) Oh, H.-K.; Kim, K.; Park, J.; Im, H.; Maher, S.; Kim, M.-G. Plasmon color-preserved gold nanoparticle clusters for high sensitivity detection of SARS-CoV-2 based on lateral flow immunoassay. *Biosensors and Bioelectronics* **2022**, *205*, 114094. DOI: https://doi.org/10.1016/j.bios.2022.114094.
(22) Han, H.; Wang, C.; Yang, X.; Zheng, S.; Cheng, X.; Liu, Z.; Zhao, B.; Xiao, R. Rapid field determination of SARS-CoV-2 by a colorimetric and fluorescent dual-functional lateral flow immunoassay biosensor. *Sensors and Actuators B: Chemical* **2022**, *351*, 130897. DOI: https://doi.org/10.1016/j.snb.2021.130897.
(23) Brandmeier, J. C.; Jurga, N.; Grzyb, T.; Hlaváček, A.; Obořilová, R.; Skládal, P.; Farka, Z.; Gorris, H. H. Digital and Analog Detection of SARS-CoV-2 Nucleocapsid Protein via an Upconversion-Linked Immunosorbent Assay. *Analytical Chemistry* **2023**, *95* (10), 4753–4759. DOI: 10.1021/acs.analchem.2c05670.
(24) Huang, L.; Ding, L.; Zhou, J.; Chen, S.; Chen, F.; Zhao, C.; Xu, J.; Hu, W.; Ji, J.; Xu, H.; et al. One-step rapid quantification of SARS-CoV-2 virus particles via low-cost nanoplasmonic sensors in generic microplate reader and point-of-care device. *Biosens Bioelectron* **2021**, *171*, 112685. DOI: 10.1016/j.bios.2020.112685 From NLM.
(25) Dou, X.; Zhang, Z.; Liu, B.; Li, C.; Du, Y.; Tian, F. Highly sensitive digital detection of SARS-CoV-2 nucleocapsid protein through single-molecule counting. *Anal Bioanal Chem* **2023**, *415* (25), 6155–6164. DOI: 10.1007/s00216-023-04886-2 From NLM.
(26) Zhang, L.; Wen, S.; Khan, J. U.; Liu, Y.; Maddahfar, M.; Zhou, J.; Jin, D. Ultrasensitive Rapid Antigen Test by Geometric Lateral Flow Assays and Highly Doped Upconversion Nanoparticles. *Analytical Chemistry* **2024**, *96* (42), 16581–16589. DOI: 10.1021/acs.analchem.4c02379.

Chapter 5 Pipette-tip-based Platform for Multiple Protein Detection

Simultaneous detection of multiple biomarkers from a single sample has emerged as a crucial approach to improve diagnostic efficiency, reduce sample volume, and enable high-throughput analysis. This capability is particularly important in clinical diagnostics, infectious disease monitoring, and biomarker profiling, where complex physiological responses often involve multiple proteins. While immunoassay technologies offer unmatched specificity and versatility compared to other analytical techniques, the advancement toward multiplex analysis introduces new challenges, most notably, cross-reactivity as wells as the non-specific binding, which can compromise both sensitivity and specificity.

In Chapter 5, we aim to extend our previously established Beads-on-a-tip platform in Chapter 4 to explore its applicability in multiplex protein detection. By simultaneously targeting three SARS-CoV-2 antigens, namely the spike (S) protein from the Omicron variant, the spike protein from the Delta variant, and the nucleocapsid (N) protein, three distinct antibody pairs were employed to assess the platform's capability to accurately discriminate multiple analytes within a single assay run. This study not only provides the detection fidelity of our Beads-on-a-Tip-based method under multiplexing conditions, but also demonstrates its potential for streamlined, point-of-care diagnostics where multi-target analysis is increasingly essential.

5.1 The introduction of multiplexed detection

Over the past few decades, immunoassays such as ELISA and Western blotting have become standard tools for protein quantification in complex biological samples. These conventional sandwich immunoassays typically target a single analyte using a pair of specific antibodies, offering reliable information on the presence and relative abundance of the target protein. While highly effective in many contexts, single-analyte detection approaches face significant limitations when applied to multifactorial diseases where multiple biomarkers are involved. For example, Alzheimer's disease, a complex neurodegenerative disorder in which no single biomarker can reliably distinguish affected individuals from other forms of dementia. Multiple proteins, such

as amyloid-beta (Aβ42), total tau (t-tau), and phosphorylated tau (p-tau), contribute to disease pathology.[1, 2] Another example is the widely studied SARS-CoV-2 virus in recent years, which contains multiple structural proteins, including the S protein and N protein. Many diagnostic assays are designed to detect either S or N protein individually.[3, 4] However, the S protein itself exhibits extensive variation across viral strains, such as Alpha, Beta, Gamma, Delta, and Omicron, with mutations that may alter epitope recognition.[5] Consequently, relying on a single antigen for diagnosis may result in reduced sensitivity or false-negative outcomes. Simultaneous detection of both S and N proteins, or even multiple S variants, can greatly enhance diagnostic accuracy.

Multiplex technologies, originally developed for nucleic acid detection, have since expanded into protein detection and enable simultaneous identification and quantification of multiple disease-related biomarkers.[6] This capability is particularly important for early and accurate diagnosis, especially in time-sensitive clinical settings where prompt decision-making is critical. Multiplex sandwich immunoassays operate on similar principles as conventional ELISA but utilize multiple antibody pairs, each of which each specific to a different analyte and assign distinct readout channels. This enables the concurrent measurement of two or more proteins within a single assay run. One of the key advantages of multiplex immunoassays is their efficient use of sample volume. Instead of requiring separate aliquots for each ELISA, a single sample can be used to analyze multiple targets simultaneously. This consolidation not only conserves precious biological material but also reduces sample processing steps and reagent usage, thereby improving laboratory efficiency. In addition, multiplex assays minimize inter-assay variability, such as differences in incubation time, temperature, and reagent composition, that often affect the consistency of results across separate single-analyte tests. Multiplex assays are increasingly replacing traditional ELISA techniques due to their advantages in saving time, reagents, and labor, while also enabling the efficient processing of large sample volumes to enhance overall throughput.

`

5.2 The recent research of multiplexed detection

To meet the increasing demand for comprehensive biomarker profiling, a variety of multiplex immunoassay platforms have emerged, enabling the simultaneous quantification of multiple analytes within a single assay run. In this section, we summarize the recent advances in representative multiplex immunoassay formats, including microwell-plate based, paper based and imaging-based assay. Each of these technologies offers distinct advantages and trade-offs in terms of detection performance, scalability, and point-of-care applicability.

Table 1 shows some representative studies that employ antibody-antigen-based strategies for the multiplex detection of disease-relevant protein biomarkers.

Platform	Method	Targets	Sensitivity	Point-of-care	Ref
Microwell-plate based	Digital Elisa (Simoa)	PSA	LOD with 1.5 fg/mL	No	[7]
		TNF-α	LOD with 2.5 fg/mL		
	Open-Source Multiplex-ELISA Platform	SAS-Cov-2 antigens from real sera sample	Sensitivity of 97.8% with S protein, N with 81.7%, RBD with 96.8%		[8]
Microscopy-based	Quantum Dots-based Microfluidics	HBV	Detection range from 10^{-10} -10^{-12} M		[9]
		HIV			
		HCV	Detection range from 10^{-9} -10^{-10} M		
	Dropcast Single Molecule Array (dSimoa)	IL-10	LOD with 2 pg/mL		[10]
		IL-1β	LOD with 384 fg/mL		

	MBs-based Digital Immunoassay	Fetoprotein	LOD with 21 pg/mL		11
		Human interleukin-6	LOD with 0.19 pg/mL		
Paper-based	Quantum Dots-based Microarray Gold NPs-based Microarray	Ofloxacin	LOD with 0.3 ng/mL	Yes	12
		Chloramphenicol	LOD with 0.12 ng/mL		
		Streptomycin	LOD with 0.2 ng/mL		
		15 allergens from clinical serum samples	ImmunoCAP at ≥1 kU		13
	UCNP-based LFIA	10 pathogens	LOD with 10^4 CFU mL^{-1} or 10^5 CFU mL^{-1} for each pathogen		14

5.2.1 Multiplex microwell-plate based assay

Microwell-plate-based immunoassays are among the most established and widely used platforms for multiplex protein detection. These assays typically utilize 96-well or higher-density plate formats, where each well acts as an independent reaction chamber. By spatially separating different capture antibodies into distinct wells or different regions within a single well, it is possible to simultaneously detect multiple analytes from the same sample. This platform is compatible with conventional ELISA workflows and can use various signal readouts, such as colorimetric, chemiluminescent, or fluorescent methods.

Walt et al. group introduced the digital ELISA technology (SiMoA), which significantly enhanced sensitivity by confining single enzyme-labeled immunocomplexes into

femtoliter-volume microwells [7]. In this method, proteins are first captured on antibody-coated microbeads and labeled with enzymes so that each bead contains either zero or one target molecule. These beads are then isolated into arrays of 50 fL reaction wells. Using fluorescence imaging, individual enzyme events can be detected, enabling ultrasensitive quantification. Using PSA and TNF-α as model analytes, they achieved LODs of 1.5 fg/mL and 2.5 fg/mL, respectively. PSA was detectable in all 30 patient samples, ranging from 14 fg/mL to 9.4 pg/mL, with an average concentration of 1.5 pg/mL.

Byrum et al. developed an open-source multiplex ELISA platform to assess antibody responses against SARS-CoV-2 using a 96-well protein microarray format [8]. Each well was imaged automatically by an open-source plate reader, and data was processed using open-source software to quantify optical density signals. Their system showed strong diagnostic performance in 217 human serum samples, with classification sensitivity for anti-RBD at 96.8%, anti-Spike at 97.8%, and anti-Nucleocapsid at 81.7%.

5.2.2 Multiplex microscopy-based immunoassay

Among imaging-based immunoassays, microbead-based platforms are the most widely used for multiplexed protein detection. These systems typically immobilize specific capture molecules on microbeads, enabling simultaneous detection of multiple analytes through spatial or spectral encoding.

Klostranec et al. developed quantum dot-encoded microbeads (QdotBs), embedding distinct ratios of red, yellow, and green-emitting QDs to generate spectrally unique signatures[9]. Using a microfluidic platform, they conducted an indirect immunoassay for hepatitis B surface antigen (HBsAg), hepatitis C virus NSP4 protein, and HIV gp41. Target proteins were coated onto QdotBs, followed by detection with specific antibodies. Emission signals were captured via a solid-state photodetector. The LODs for HBsAg and gp41 were in the low picomolar range (~10^{-10} to 10^{-12} M), with slightly higher values for NSP4. Compared with FDA-approved kits using the same antibodies and antigens, their sensitivity improved by tens of times.

Wu et al. group introduced dSiMoA (dropcast single molecule array), a simplified digital ELISA format building upon conventional SiMoA[10]. In this method, capture antibodies are immobilized on paramagnetic beads, which are incubated with the target antigen and a biotinylated detection antibody to form a sandwich

immunocomplex. Instead of enzymatic labeling, streptavidin–DNA conjugates bind to pre-annealed primer-template pairs to trigger rolling circle amplification (RCA). Following amplification, beads are dropcast onto microscope slides, dried into monolayers, and imaged for digital signal readout. This simplified approach reduces background noise and allows for attomolar-level sensitivity. Detection of IL-1β and IL-10 yielded LODs of 99.6 aM (~2 pg/mL) and 19.2 aM (~384 fg/mL), respectively.

Gong et al. proposed a fluorescence-based digital immunoassay using color-coded microbeads to simultaneously detect alpha-fetoprotein (AFP) and interleukin-6 (IL-6) [11]. Biotin-labeled sandwich immunocomplexes were formed on two types of fluorescent beads, followed by capture using streptavidin-coated magnetic beads (SA-MBs). The proportion of different colored beads was quantified using wide-field fluorescence microscopy. This platform achieved LODs of 21 pg/mL (0.30 pM) for AFP and 0.19 pg/mL (7.3 fM) for IL-6.

5.2.3 Multiplex paper-based immunoassay

Among POCT-compatible platforms, paper-based immunoassays, particularly lateral flow assays (LFIAs), remain the most widely adopted for multiplex analysis. The conventional approach employs multiple test lines or dot arrays on a single strip using different probes, such as gold nanoparticles (GNPs), quantum dots (QDs), or colored/fluorescent microspheres.

Taranova et al. demonstrated a multicolor QD-based LFIA for detecting three antibiotics (ofloxacin, chloramphenicol, and streptomycin) in milk[12], using QDs with red, yellow, and green emission. Their system achieved LODs of 0.3, 0.12, and 0.2 ng/mL, respectively. However, placing multiple lines on a single strip is space-limited. Extending the strip increases both assay time and sample volume requirements and may affect membrane flow reproducibility. To overcome this, Svahn et al. developed a dot-array LFIA incorporating 15 allergens, each spotted in ~300 pL volumes to form ~120 μm dots[13]. Each allergen was represented by four identical dots arranged in rows, and the signal was quantified by a custom reader. Another approach involves parallel strip integration. Zhao et al. presented a ten-channel upconversion nanoparticle based-LFIA disk to simultaneously detect antibodies against 10 Yersinia pestis antigens[14]. Each test strip was optimized individually and integrated into a unified

circular cartridge. LODs ranged from 10^4 to 10^5 CFU/mL. A similar configuration enabled detection of 10 foodborne pathogens with comparable sensitivity. However, as each strip required 50–100 µL of sample, this significantly increased the total volume of sample needed for analysis.

Multiplex immunoassays rely heavily on probe encoding strategies, such as color-coding or spectral barcoding, which require either microscopy or microwell-based platforms for readout. While imaging- and microwell-based approaches offer extremely low LODs, they involve complex procedures and longer assay times. In contrast, paper-based LFIAs provide ease of use and portability, but their sensitivity remains relatively limited. Therefore, future development in POCT will benefit from materials innovation that bridges these strengths, enabling simple, yet sensitive and robust multiplex detection.

Based on the above discussion, we find that these multiplex detection methods heavily rely on advances in material synthesis, particularly the development of color-coded probes for the simultaneous detection of multiple analytes. These color-coded probes often require microscopy or microwell-based platforms to distinguish signals from different targets. Among existing approaches, paper-based LFIA is currently the most suitable for POCT due to its simplicity and portability. However, it suffers from limited sensitivity. In contrast, imaging-and microwell-based platforms offer much lower detection limits but are more complex to operate and require longer assay times. Therefore, there is a pressing need to leverage material innovation to develop new POCT-compatible multiplex methods that combine high sensitivity with operational simplicity.

5.3 The advantages of UCNPs in the multiplex detection and MBs

One of the key advantages of using UCNPs in multiplexed immunoassays is their ability to emit distinct fluorescence signals under a single near-infrared excitation, achieved by doping different lanthanide ions into the host lattice. For example, Tm^{3+} and Er^{3+}-doped UCNPs emit characteristic blue and green emissions, respectively, allowing spectral differentiation of multiple analytes without spectral overlap. This intrinsic optical coding eliminates the need for multiple excitation sources or complex filters and enables highly multiplexed analysis with minimal background interference.

Additionally, MBs with different sizes (e.g., 2.8 μm and 1 μm) can be used as solid supports for target-specific antibody conjugation, allowing physical differentiation of multiple immunocomplexes.

In this study, we further leveraged the previously developed Beads-on-a-Tip platform to evaluate its capacity for multiplexed detection. By incorporating both different doping UCNPs and size-differentiated MBs, the platform enables simultaneous detection of multiple target proteins in a single pipette-tip assay.

5.4 Experimental Design

To demonstrate the multiplexing capability of the Beads-on-a-Tip platform, we extended the assay configuration and methodology described in Chapter 2 to design a model system capable of simultaneously detecting three SARS-CoV-2 antigens: the spike protein of the Omicron variant (AgS_O), the spike protein of the Delta variant (AgS_D), and the nucleocapsid protein (AgN). Two distinct populations of magnetic beads (2.8 μm and 1 μm in diameter) were employed as capture substrates, enabling physical differentiation during imaging based on their size.

To achieve optical separation of the signals from different targets, UCNPs doped with either Tm^{3+} or Er^{3+} were conjugated to detection antibodies specific for each antigen. Under a single 980 nm excitation wavelength, these dopants generate well-separated emission peaks (Tm^{3+}: 800 nm; Er^{3+}: 650 nm), allowing clear spectral discrimination from the detector of the resulting immunocomplexes. By integrating both size-based and emission-based encoding strategies, this platform offers enhanced multiplexing resolution and enables accurate identification of individual analytes within a single assay format.

5.4.1 Materials

AgS_O: A pair of SARS-CoV-2 Omicron (XBB.1) Spike RBD Specific Antibody (40589-D008) and SARS-CoV-2 Omicron (XBB.1) spike specific Antibody (40589-D007) for SARS-CoV-2 omicron (XBB.1.16) spike S1+S2 trimer protein (40589-V08H48) detection.

AgS_D: a pair of SARS-CoV-2 Delta spike RBD specific antibody (40589-D006) and SARS-CoV-2 spike antibody (40592-R190) for SARS-CoV-2 Delta (B.1.617.2) spike S1+S2 trimer protein (40589-V08H10) detection.

AgN: a pair of SARS-CoV-2 (2019-nCoV) nucleocapsid antibody (40588-MM124) and SARS-CoV/SARS-CoV-2 nucleocapsid antibody (40143-R040) for SARS-CoV-2 Delta (B.1.617.3) nucleocapsid protein (40588-V07E30). All antibodies and ant

Two sizes of magnetic beads were used, Dynabeads® M-270 Carboxylic Acid (2.8 μm), and Dynabeads® MyOne™ Carboxylic Acid (1μm) from Thermofisher.

5.4.2 Characterization of UCNPs (Er, Tm)

In this study, two types of core shell upconversion nanoparticles (UCNPs) were synthesized with distinct energy transfer pathways: $NaYF_4$ doped with 40% Yb^{3+}, 4% Tm^{3+}, and 40% Yb^{3+}, 4% Er^{3+}. Yb^{3+} ions act as sensitizers, efficiently absorbing 980 nm near-infrared excitation light and transferring the energy to the activator ions (Tm^{3+} or Er^{3+}), thereby initiating the upconversion emission process. To ensure consistency in experimental conditions, the particle sizes of both types of UCNPs were matched to remain nearly identical. The same polymer and polymer-based ligand exchange strategy described in Section 2.2. The as-synthesized Er^{3+}-doped UCNPs had an average diameter of 37 nm, increasing to 42 nm after surface modification. The Tm^{3+}-doped UCNPs were initially 38 nm in diameter and reached 43 nm after modification (Figure 1). The detailed synthesis procedures, structural tuning strategies, and size control methods are provided in Section 2.1 of Chapter 2. These doping were chosen for their distinct upconversion emission profiles under 980 nm excitation, which enable spectral multiplexing. As shown in Figure 1, Tm^{3+}-doped UCNPs exhibited a sharp emission pea at 800 nm, corresponding to the $^3H_4 \rightarrow {}^3H_6$ transition. In contrast, Er^{3+}-doped UCNPs displayed strong emission at 650 nm (Figure 1b), attributed to the $^4F_{9/2} \rightarrow {}^4I_{15/2}$ transition. These spectrally distinct emissions permit simultaneous, dual-channel optical detection with minimal signal overlap, making them highly suitable for multiplexed immunoassays. The unique emission wavelengths of each UCNP formulation serve as optical signatures to distinguish different analytes or detection zones in complex biosensing environments.

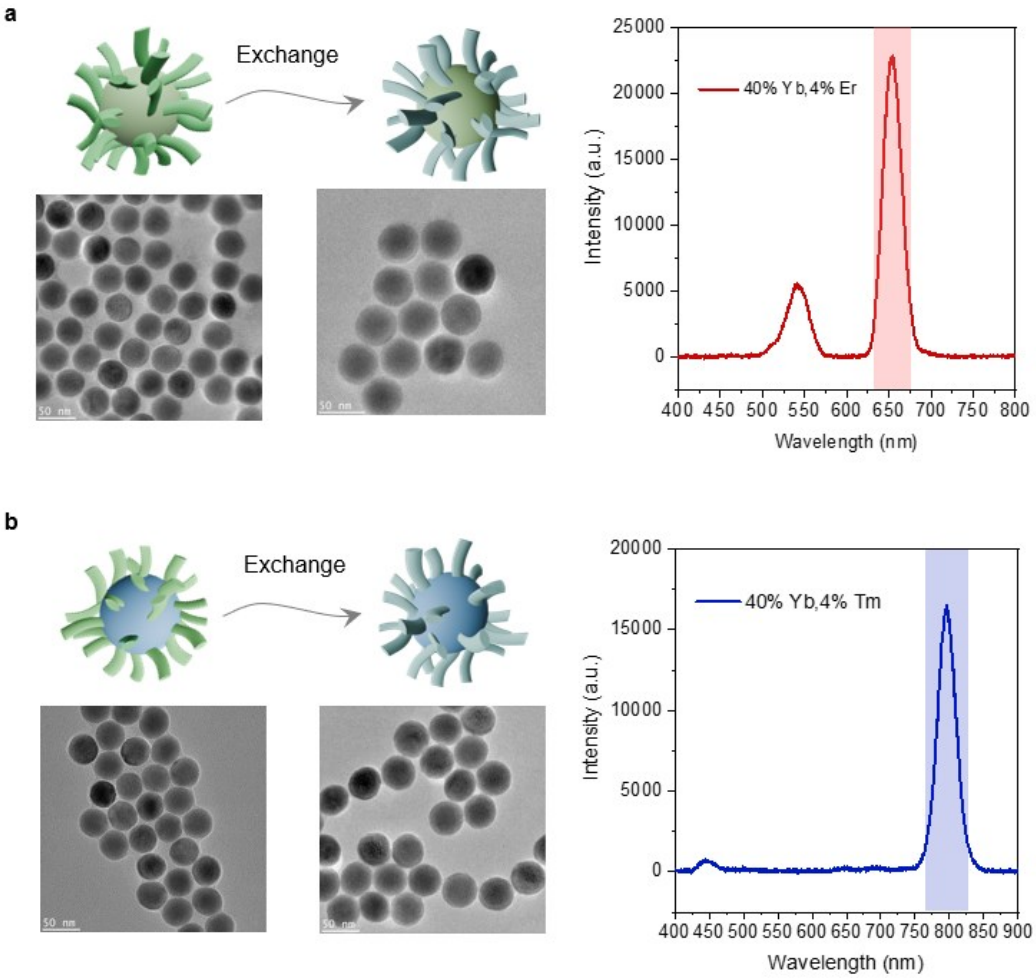

Figure 1. Characterization of Er^{3+}- and Tm^{3+}-doped UCNPs. a, Schematic illustration of surface ligand exchange of Er^{3+}-doped UCNPs (40% Yb^{3+}, 4% Er^{3+}), with TEM images before (left) and after (right) modification. The emission spectrum under 980 nm excitation at 650 nm; b, Schematic illustration of surface ligand exchange of Tm^{3+}-doped UCNPs (40% Yb^{3+}, 4% Tm^{3+}), with TEM images before (left) and after (right) modification. The emission spectrum under 980 nm excitation at 800 nm.

5.4.3 Probes design

Table 2. Multiplexed probe configuration combining magnetic beads of distinct sizes with UCNPs doped with Tm^{3+} or Er^{3+} for dual-channel detection of SARS-CoV-2 antigens (S_o, S_D, and N).

Ag	MB-Abs	UCNP-Abs

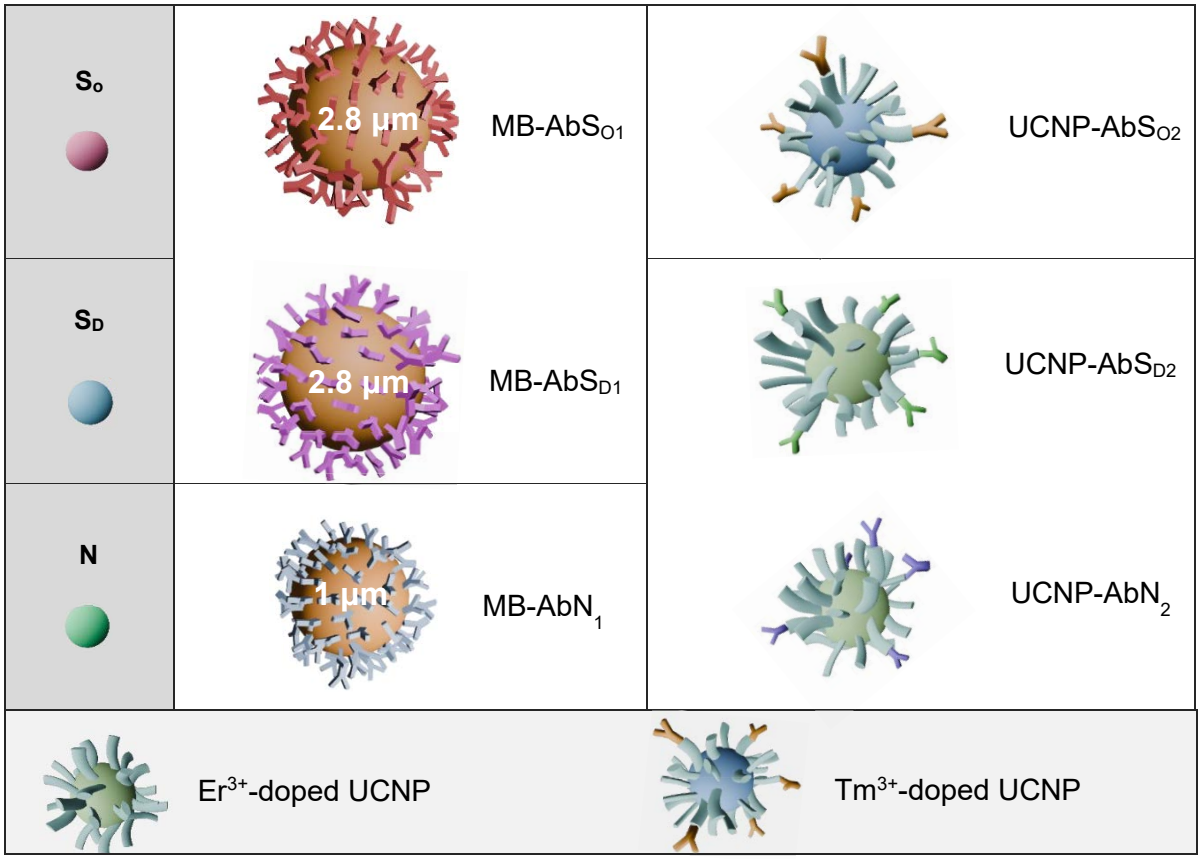

We systematically evaluated both 'one-to-one' (single antigen detection for specificity validation) and 'many-to-many' (multiplexed) assay configurations to simulate real-world diagnostic conditions. Table 2 summarizes the probe design, in which each group is configured to form a complete sandwich immunocomplex for its target antigen. MBs-AbS_{O1} and MBs-AbS_{D1}, both immobilized on 2.8 μm magnetic beads, were employed to capture the Omicron (AgS_O) and Delta spike proteins (AgS_D), respectively. While MBs-AbN_1, conjugated to 1 μm beads, was used to bind the nucleocapsid protein (AgN). For signal generation, the corresponding detection antibodies were conjugated to UCNPs doped with either Tm^{3+} or Er^{3+} to ensure spectral resolution. Specifically, UCNP-AbS_{O2} (Tm^{3+} doped) was paired with MBs- AbS_{O1}, while UCNP-AbS_{D2} and UCNP-AbN_2 (both Er^{3+} doped) were paired with MBs-AbS_{D1} and MBs-AbN_1, respectively.

5.4.4 Beads-Abs efficiency optimization

In this experiment, the antibody conjugation onto 1 μm magnetic beads was carried out using the EDC/NHS-mediated coupling method described in Section 2.3.3 of Chapter 2. Given that these beads differ in both size and working concentration from

the 2.8 μm beads employed in Chapter 4, it was necessary to re-evaluate the antibody coupling efficiency under the current experimental conditions, specifically, to determine the optimal ratio between antibody input and bead quantity. To assess the effectiveness of antibody immobilization on the bead surface, Alexa Fluor 488-labeled secondary antibodies were introduced. Their binding to the surface-bound primary antibodies produced a fluorescence signal, which served as an indirect measure of the conjugation efficiency.

As shown in the Figure 2, increasing the primary antibody amount from 0.05 μg to 2 μg resulted in a progressive enhancement in fluorescence intensity, with corresponding SNR values showing a clear upward trend. This indicates that the antibodies were effectively immobilized on the surface of the 1 μm magnetic beads. Notably, a slight decline in SNR was observed when the antibody input exceeded 2 μg, a trend consistent with previous observations using 2.8 μm beads in Chapter 4. This decrease is also likely attributed to concentration quenching caused by the close packing of fluorescent dyes near the bead surface at high antibody densities, rather than an actual saturation of binding sites.

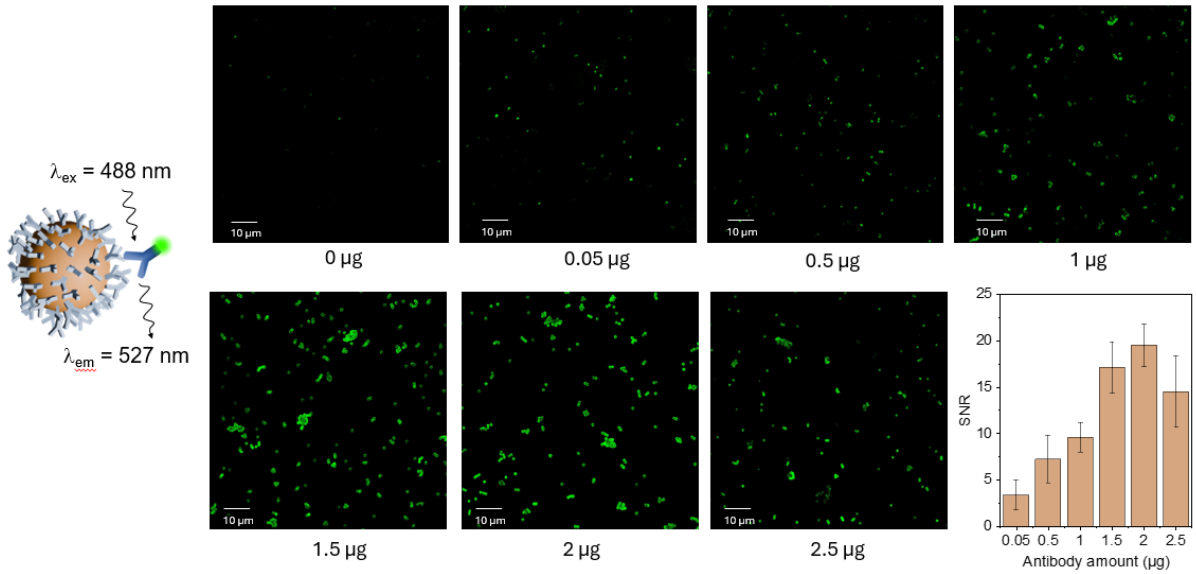

Figure 2. Fluorescence microscopy images and quantitative analysis of antibody loading on 1 μm MBs with varying amounts of antibody (0–2.5 μg). Statistical analysis was performed by quantifying the fluorescence intensity of at least 50 beads per group

5.5 Specificity test

5.5.1 Single antigen detection

Prior to implementing multiplex detection, it is critical to validate the specificity of each antibody pair for its corresponding antigen to ensure selective recognition and avoid cross-reactivity. This specificity test not only confirms that each antibody binds exclusively to its target antigen but also enables a direct comparison between the signals obtained in single-antigen assays and those observed in multiplex formats. Such comparisons are essential for evaluating potential cross-reactivity and assessing its impact on assay performance. In multiplex immunoassays, non-specific binding or unintended interactions between mismatched antibody–antigen pairs can significantly compromise detection fidelity and lead to false-positive results. Therefore, establishing the independent specificity of each antigen–antibody pair is a fundamental prerequisite for accurate and reliable multiplex detection.

To evaluate antibody specificity prior to multiplex detection, three individual sandwich-format immunocomplexes were constructed and tested separately, as illustrated in Figure 3. Each immunocomplex consisted of a single target antigen, a magnetic bead–antibody conjugate (MBs-Ab), and a corresponding UCNP–antibody conjugate (UCNP-Ab), following the assay procedure described in Section 2.3.2.1 of Chapter 2. Specifically, the three immunocomplex were formed: Immunocomplex 1 (MB-AbS_{O1}+ AgS_O + UCNP-AbS_{O2}), Immunocomplex 2 (MB-AbS_{D1} + AgS_D + UCNP-AbS_{D2}) and Immunocomplex 3 (MB-AbN_1 + AgN + UCNP-AbN_2).

Each immunocomplex was evaluated independently using stringent controls to assess both target-specific binding and potential off-target interactions. Each antibody pair was validated for use in subsequent multiplex assays only after demonstrating high specificity toward its corresponding antigen and showing negligible non-specific binding; otherwise, optimization of the reaction buffer and incubation time would be necessary. This step is essential to ensure analytical accuracy and reliable signal discrimination in the presence of multiple antigens within a single sample.

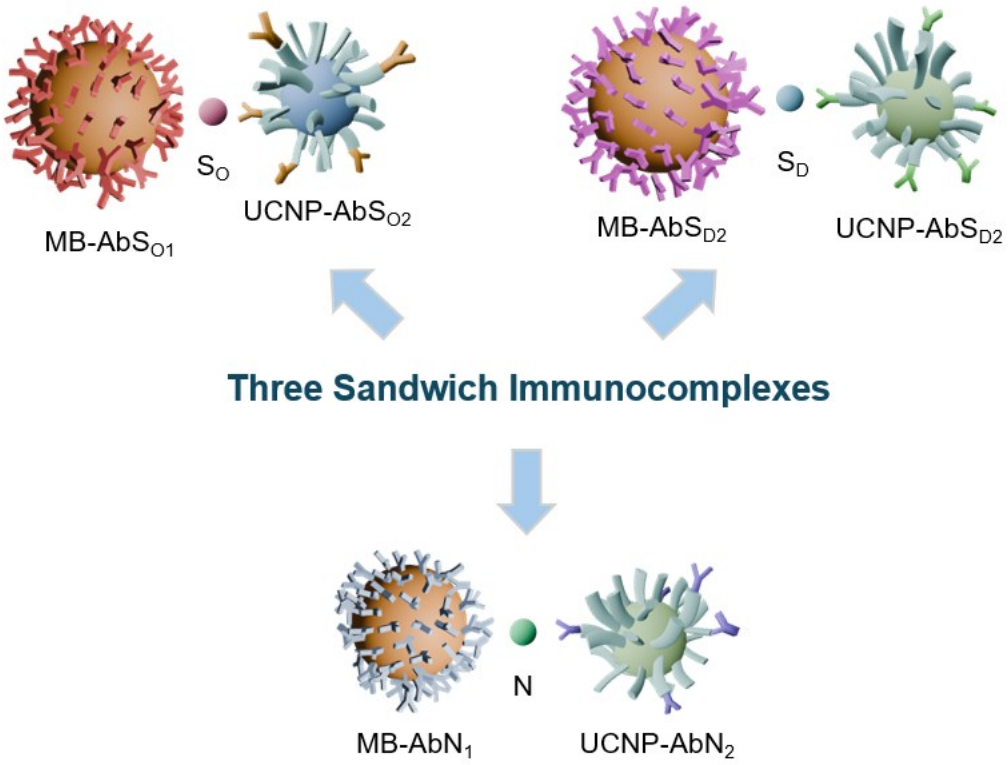

Figure 3. Schematic illustration of the three sandwich-format immunocomplexes designed for multiplex detection of SARS-CoV-2 antigens. Each target antigen was captured by a specific magnetic bead–antibody conjugate (MB-Abs) and subsequently recognized by a corresponding UCNP–antibody conjugate (UCNP-Abs)

5.5.2 Result

Here, we first evaluated the specificity of each antibody pair toward its corresponding antigen. The SNR was assessed over a concentration range of 500 fg/mL to 10,000 μg/mL for Omicron spike protein (AgS$_O$), Delta spike protein (AgS$_D$), and nucleocapsid protein (AgN) to validate the performance of antigen detection (Figure 4). Each assay procedure was individually optimized for the corresponding target.

Among the three antigen targets, S$_D$ protein detection achieved the best analytical performance, achieving the lowest LOD at 0.109 pg/mL (Figure 4b). This superior sensitivity is primarily attributed to the high binding affinity between the selected antibody pair for the S$_D$ antigen, as supported by ELISA evaluation (Figure 5). In contrast, the S$_O$ and N protein assays, which utilized antibody pairs with comparable binding affinities, demonstrated similar LOD values of 0.565 pg/mL and 0.774 pg/mL,

respectively. The relatively higher LOD observed for the N protein assay is not only associated with antibody binding but also influenced by the use of smaller magnetic beads (1 μm). Although the Beads-on-a-Tip platform facilitates efficient immunocomplex collection and localized detection, the reduced magnetic responsiveness of the smaller beads results in less effective washing. The elevated background noise raises the baseline level, thereby limiting the assay's sensitivity and increasing the calculated LOD. Despite these differences, all immunocomplex systems exhibited a distinct, concentration-dependent signal increase in the presence of their specific antigen, indicating effective antigen recognition and target-specific signal generation under the tested conditions.

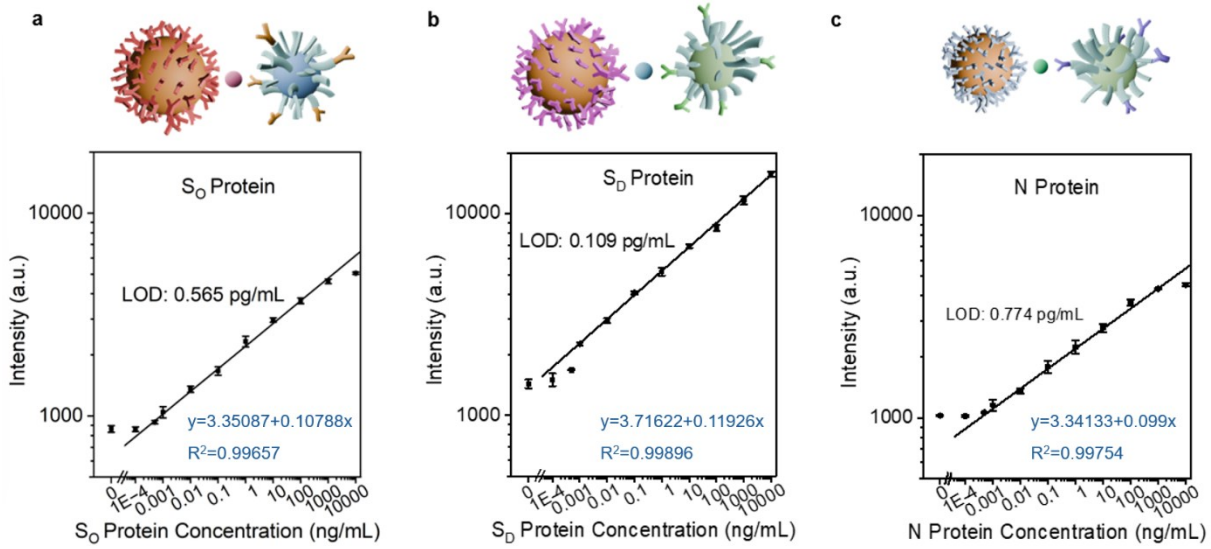

Figure 4. Calibration curves for the detection of three SARS-CoV-2 antigens using the Beads-on-a-Tip platform. a, Omicron variant spike protein (S_O) (n=10); b, Delta variant spike protein (S_D) (n=10); c, Nucleocapsid protein (N) (n=10). Black lines represent linear regression fits within the indicated concentration ranges, with the corresponding fitting equations and coefficients of determination (R^2) shown in each condition

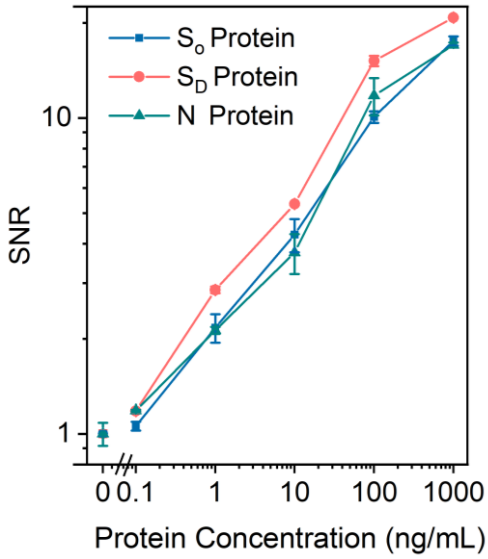

Figure 5. ELISA evaluation of the binding affinities for three sandwich-format antibody pairs corresponding to the S_O, S_D, and N protein (n=3 in each variant)

5.6 Cross reactivity test

5.6.1 Simultaneous detection of three antigens using one MB-Ab conjugate and two mismatched UCNP-Ab conjugates

5.6.1.1 Design

Table 3. Cross-reactivity test design using mismatched MB-Abs and UCNP-Abs pairs. Each MB-Abs was incubated with a 1:1:1 mixture of S_O, S_D, and N protein, along with two non-paired UCNP-Abs conjugates.

Group	MBs-Abs	Ag	UCNP-Abs
1	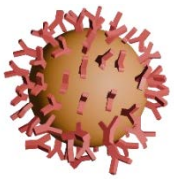 MB-AbS_{O1}	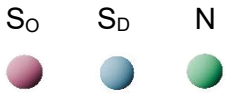 S_O S_D N (1:1:1)	 UCNP-AbS_{D2} 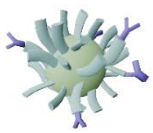 UCNP-AbN_2
2	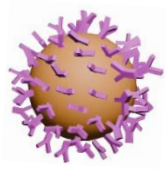 MB-AbS_{D1}		 UCNP-AbS_{O2} 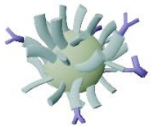 UCNP-AbN_2

3	 MB-AbN$_1$		 UCNP-AbS$_{O2}$  UCNP-AbS$_{D2}$

To evaluate the potential cross-reactivity among antibody–antigen pairs in the multiplexed immunoassay, a series of control groups were systematically designed (Table 3). In each configuration, the specific MBs-Abs were used as the capture probe and exposed to a mixed solution containing three SARS-CoV-2 protein equal concentrations of the S_O, S_D, and N protein in a 1:1:1 ratio. However, the corresponding UCNP-conjugated detection probes used in these experiments were intentionally selected to be non-paired with the capture antibody, thereby preventing the formation of a sandwich immunocomplex.

In each configuration, the specific MBs-Abs were used as the capture probe and exposed to a mixed solution containing three SARS-CoV-2 antigens (S_O, S_D, and N) at equal molar ratios (1:1:1), but with two non-paired UCNP-conjugates (Table 3). Although the classical sandwich immunoassay format was maintained, these test setups intentionally disrupted the pairing between capture and detection antibodies, ensuring that both antibodies could not bind to the same antigen. As a result, the formation of complete sandwich immunocomplexes was not expected. While the overall assay format maintained the classical sandwich architecture, the deliberate mismatch between capture and detection antibodies ensured that simultaneous binding to the same antigen could not occur. Under these conditions, the generation of a measurable signal would indicate the presence of non-specific interactions, potentially arising from unintended binding between the antibodies and non-target antigens.

The absence of detectable signal in these tests would confirm the high selectivity of the antibody pairs and validate the minimal cross-reactivity of the multiplexed platform. Conversely, any observable signal would highlight potential non-specific binding and indicate the need for further assay refinement, including antibody screening, buffer optimization, or more stringent washing protocols.

5.6.1.2 Result

The experimental results are shown in Figure 6. All three groups employed intentionally mismatched sandwich immunoassay configurations, in which the MBs-Abs and the UCNPs-Abs were not specific to the any antigen. Across the tested concentration range (0.001, 0.1, 10 and 1000 ng/mL), all three groups showed consistently low signal intensities, indicating negligible cross-reactivity. These findings confirm that the selected antibody pairs possess excellent specificity within the multiplexed assay platform. Although all three antigens were present in each reaction, the absence of matched capture and detection antibodies effectively prevented the formation of complete sandwich immunocomplexes, as designed. The lack of measurable signal under these conditions further indicates minimal cross-reactivity, thereby validating the robustness, selectivity, and reliability of the MBs and UCNPs based assay system for accurate multiplexed protein detection.

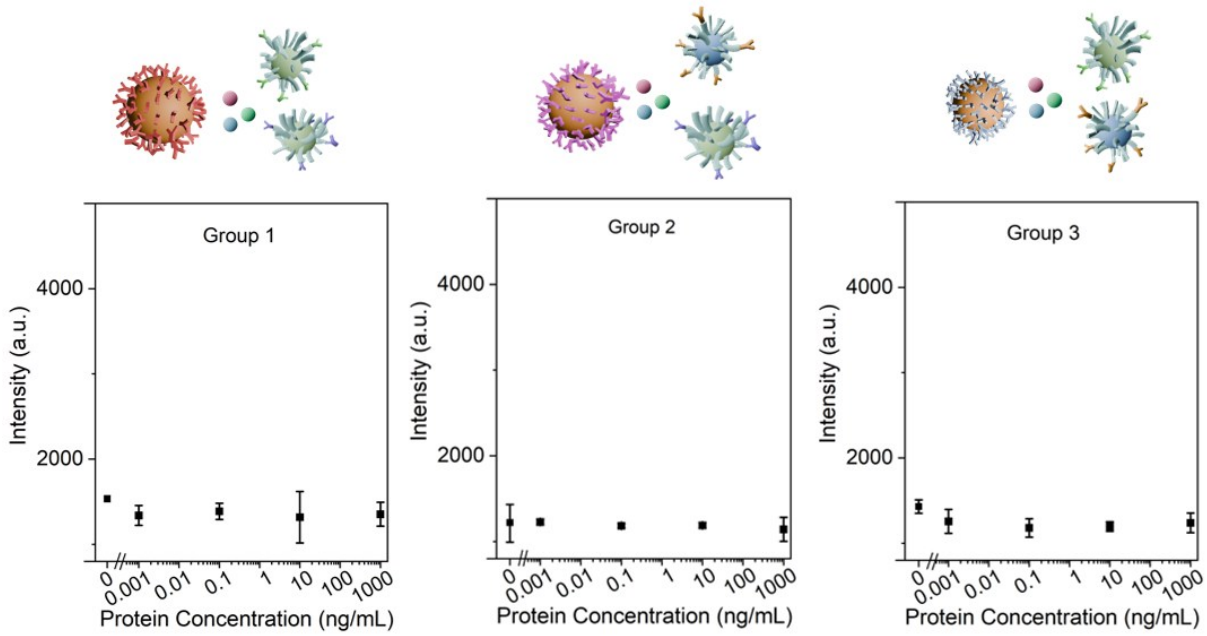

Figure 6. Cross-reactivity assessment using mismatched MB-Abs and UCNP-Abs pairs. The assays were conducted at antigen concentrations of 0.001, 0.1, 10, and 1000 ng/mL (n=3 in each variant)

5.6.2 Simultaneous detection of three antigens using one MB-Abs and three UCNP-Abs conjugates

5.6.2.1 Design

Table 4. Cross-reactivity test design using one MB-Abs and three UCNP-Abs pairs. Each MB-Abs was incubated with a 1:1:1 mixture of S_O, S_D, and N protein, along with three types of UCNP-Abs.

Group	MBs-Abs	Ag	UCNP-Abs
4	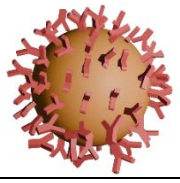 MB-AbS_{O1}	 S_O S_D N (1:1:1)	 UCNP-AbS_{O2} 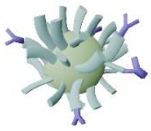 UCNP-AbN_2  UCNP-AbS_{D2}
5	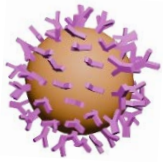 MB-AbS_{D1}		
6	 MB-AbN_1		

The primary objective of this experiment was to evaluate whether the recognition performance of a single antibody–antigen pair would be affected by the presence of other antigens and UCNP–antibody conjugates in a multiplexed detection system. In contrast to the previously described one-to-one specificity validation experiments in 5.5.1, this test adopted a one-to-mix configuration, in which only one type of MB-Abs was used per group, while all three proteins and three UCNP-Abs were simultaneously present in the reaction (Table 4). By comparing the SNR obtained in this setup with that from the single-target assay, the potential impact of multiplexing on assay performance was assessed.

5.6.2.2 Result

As shown in Figure 7, all three MBs-based systems exhibited clear linear response trends over the concentration range of 0.001-1000 ng/mL, indicating that the target antigens could still be successfully recognized even in a complex mixture of antigens and antibodies. Although the previous cross-reactivity validation demonstrated negligible non-specific binding within the system, a noticeable reduction in signal intensity was observed in this multiplexed assay configuration. Further analysis based on linear curve fitting revealed that the LOD for all assays increased under multiplexed conditions. Specifically, the LOD for S_O detection increased from 565 fg/mL to 1.89 pg/mL, S_D from 109 fg/mL to 211 fg/mL, and N from 774 fg/mL to 2.89 pg/mL, representing 3.3-fold, 1.93-fold, and 3.7-fold increases, respectively, compared to the single-target format. These results suggest the presence of mild signal suppression, potentially arising from competition among antigens or antibodies for binding sites or from steric hindrance in the multiplexed environment. However, it is worth emphasizing that despite the observed reduction in SNR under multiplexed conditions, the effective dynamic range of each detection system remained largely unchanged. These results indicate that the MB-UCNP-based platform maintains stable detection capability and reliable target recognition performance even in the presence of multiple coexisting analytes.

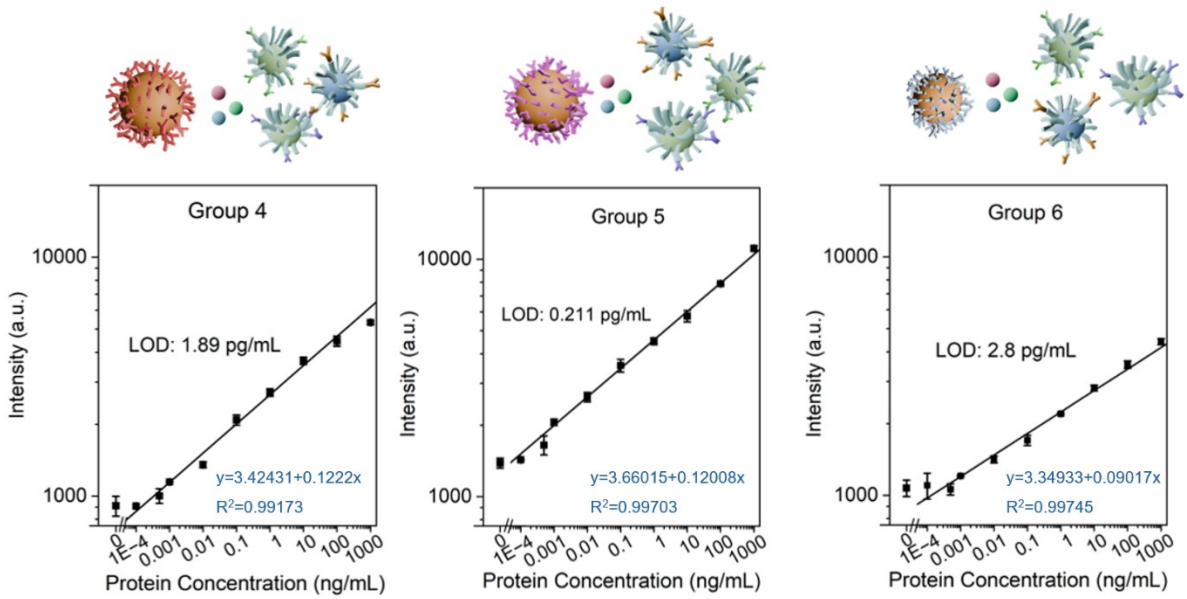

Figure 7. Simultaneous detection of three SARS-CoV-2 antigens using one MB-Ab conjugate and three types of UCNP-Ab conjugates. Calibration curves for Group 4,

Group 5, and Group 6 correspond to the detection of three mixed antigen solution with the ratio of 1:1:1 (n=10 in each variant). Black lines represent linear regression fits within the indicated concentration ranges, with the corresponding fitting equations and coefficients of determination (R^2) shown in each condition

5.6.3 Simultaneous detection of two antigens using two MB-Abs and two UCNP-Abs conjugates pairs

5.6.3.1 Design

Table 5. Experimental design for evaluating the detection performance of the multiplexed immunoassay system under unequal antigen concentrations.

Group	MBs-Abs	Ag	UCNP-Abs
4	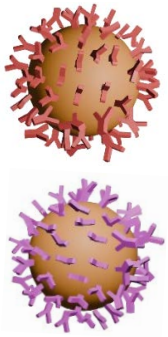 MB-AbS$_{O1}$ MB-AbS$_{D1}$	 S$_O$ S$_D$ (1:10)	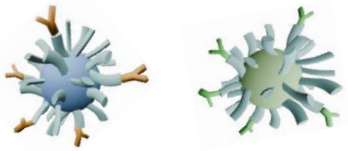 UCNP-AbS$_{O2}$ UCNP-AbS$_{D2}$
5	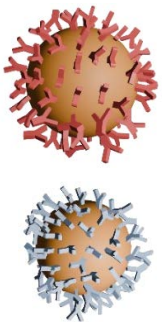 MB-AbS$_{O1}$ MB-AbN$_1$	 N S$_O$ (1:10)	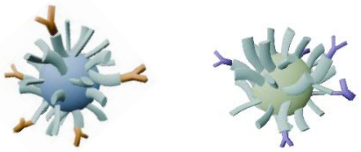 UCNP-AbS$_{O2}$ UCNP-AbN$_2$
6	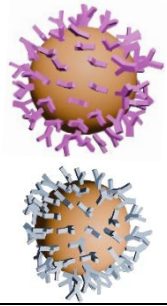 MB-AbS$_{D1}$ MB-AbN$_1$	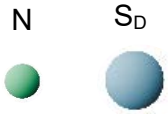 N S$_D$ (1:10)	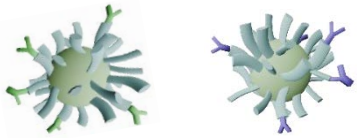 UCNP-AbS$_{D2}$ UCNP-AbN$_2$

This set of experiments was designed to evaluate the detection performance of the UCNP-MB multiplexed immunoassay system under non-equimolar antigen conditions. In each group, two distinct sandwich-format immunocomplexes were formed. Unlike the previous assays using equimolar antigen mixtures (1:1:1), this study introduced two antigens per reaction with deliberately skewed concentration ratios (1:10) to mimic clinically relevant scenarios (as shown in Table 5), where a low-abundance biomarker must be accurately detected in the presence of a high-concentration interfering antigen. Another objective of this experiment was to assess the system's signal resolution capacity under asymmetric UCNP labelling conditions, particularly in Group 6, where both UCNP probes were doped with the same Er^{3+} ion, challenging the platform's spectral discrimination capability.

In Groups 4 and 5, two types of UCNP fluorescent probes doped with Er^{3+} and Tm^{3+}, respectively, were employed to simultaneously detect two different antigen targets within the same reaction system. Group 6 used the same Er^{3+}-doped UCNPs. The antigens were introduced at a concentration ratio of 1:10, corresponding to 1000:100, 10:1, 0.1:0.01, and 0.005:0.0005 ng/mL. This setup was designed to simulate the detection of a low-abundance biomarker in the presence of a high-concentration background antigen.

5.6.3.2 Result

In group 4 and 6, the results demonstrated that both emission channels (Er and Tm) showed an independent linear response trends across their respective concentration ranges, indicating successful recognition of both targets. However, when compared with single-antigen detection assays, the signal intensities in this dual-target format were consistently lower at each concentration level. This suggests the presence of mild competitive binding that may reduce immunocomplex formation efficiency and subsequently lower signal output.

In Group 6, two UCNP probes both doped with Er^{3+} were used to simultaneously detect two antigens. Although the overall signal still followed a linear trend, the emission intensities from the two immunocomplexes overlapped due to the same emission wavelength, resulting in cumulative signals that could not be spectrally separated. This overlap prevented independent quantification of the two targets and highlights a critical

limitation: without proper spectral encoding, multiplexed detection suffers from signal convolution, which compromises quantitative resolution.

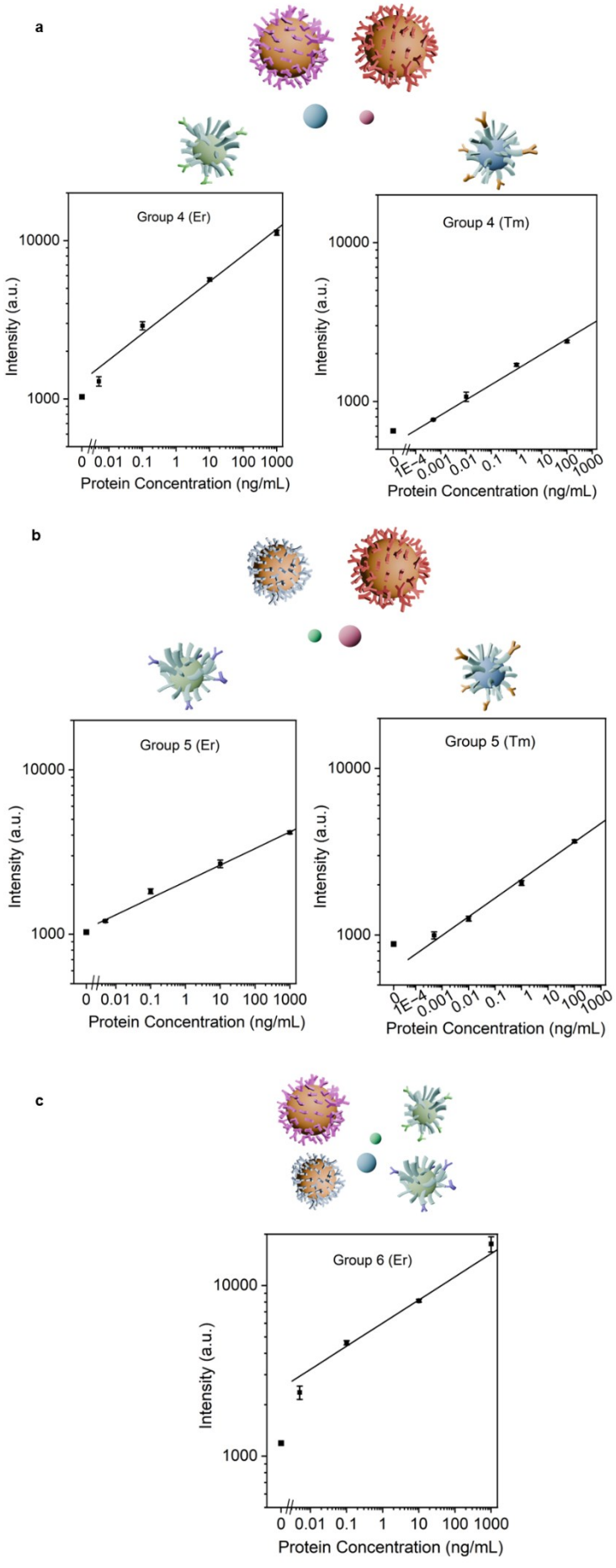
a
Group 4 (Er)
Intensity (a.u.)
10000
1000
0 0.01 0.1 1 10 100 1000
Protein Concentration (ng/mL)
Group 4 (Tm)
Intensity (a.u.)
10000
1000
0 1E-4 0.001 0.01 0.1 1 10 100 1000
Protein Concentration (ng/mL)
b
Group 5 (Er)
Intensity (a.u.)
10000
1000
0 0.01 0.1 1 10 100 1000
Protein Concentration (ng/mL)
Group 5 (Tm)
Intensity (a.u.)
10000
1000
0 1E-4 0.001 0.01 0.1 1 10 100 1000
Protein Concentration (ng/mL)
c
Group 6 (Er)
Intensity (a.u.)
10000
1000
0 0.01 0.1 1 10 100 1000
Protein Concentration (ng/mL)

Figure 8. Simultaneous detection of two antigens at a 1:10 ratio using dual sandwich formats between MB-Abs and UCNP-Abs conjugates.

5.6.4 Simultaneous detection of three antigens using three pairs of MB-Abs and UCNP-Abs conjugates

5.6.4.1 Design

Table 6. Simultaneous detection of three antigens at a concentration ratio of 1:100:10 using three sandwich pairs of MB-Abs and UCNP-Abs conjugate

MB-Abs	**Ag (1:100:10)**			**UCNP-Abs**
	S_O (ng/mL)	**S_O (ng/mL)**	**N (ng/mL)**	
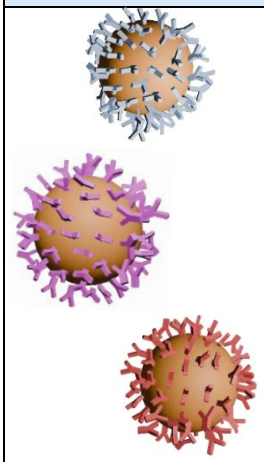	0.001	0.1	0.01	
	0.01	1	0.1	
	0.1	10	1	
	1	100	10	
	10	1000	100	

This set of experiments was designed to systematically evaluate the detection performance and stability of the UCNP–MBs multiplexed immunoassay platform under conditions of extremely imbalanced antigen co-existence. Compared to previous setups using equal (1:1:1) or concentration with ratio of 1:10, a more stringent antigen distribution model was implemented here: three SARS-CoV-2 antigens (S_O, S_D, and N) were simultaneously introduced into the reaction system at a mass concentration ratio of 1:100:10 (Table 6). This configuration more closely mimics the complexity of clinical or real biological samples, where highly abundant background antigens may suppress or interfere with the detection of target low-abundance analytes. In such multiplexed settings, avoiding signal interference becomes a key challenge for accurate target identification.

Although earlier experiments revealed that when two antigens were simultaneously labeled with UCNPs doped with the same Er^{3+}-doped, their emission signals overlapped at the same wavelength, making it impossible to distinguish the source of each signal and thus limiting quantitative analysis in multiplexed detection. However, subsequent results demonstrated that by employing UCNPs doped with different emitters (e.g., Tm^{3+} and Er^{3+}), the system was still able to spectrally resolve individual antigen signals even under imbalanced antigen loading conditions. To further investigate whether Er^{3+}-doped fluorescent probes introduce concentration-dependent interference or signal coupling when detecting different antigens, we systematically examined the response curves across a range of concentration gradients (S_O from 0.001 to 10 ng/mL, S_D from 0.1 to 1000 ng/mL, and N from 0.01 to 100 ng/mL), under conditions where two Er^{3+}-doped UCNPs were simultaneously involved in the detection.

5.6.4.2 Result

When both target antigens (S_D and N) were detected simultaneously using Er^{3+} -doped UCNPs, their relatively high concentrations led to cumulative fluorescence signals (Figure 9a). As a result, the overall signal intensity and background fluorescence were both higher than those observed in the single-analyte detection format. Since both antigens were labeled with UCNPs emitting at the same Er^{3+} wavelength, the measured fluorescence represented the combined signal from both targets. Consequently, it became impossible to distinguish the individual contributions from each antigen, and only the total signal intensity could be quantified, rather than the concentration of each analyte separately. However, in the case of S_o detection (Figure 9b), only one protein was labeled with the Tm-doped UCNP, meaning that the signal observed at the Tm emission peak originated exclusively from the N antigen. Compared to the single-analyte detection of the N antigen, a noticeable decrease in fluorescence intensity still could be observed under multiplexed conditions, likely attributable to competitive binding effects within the same reaction system.

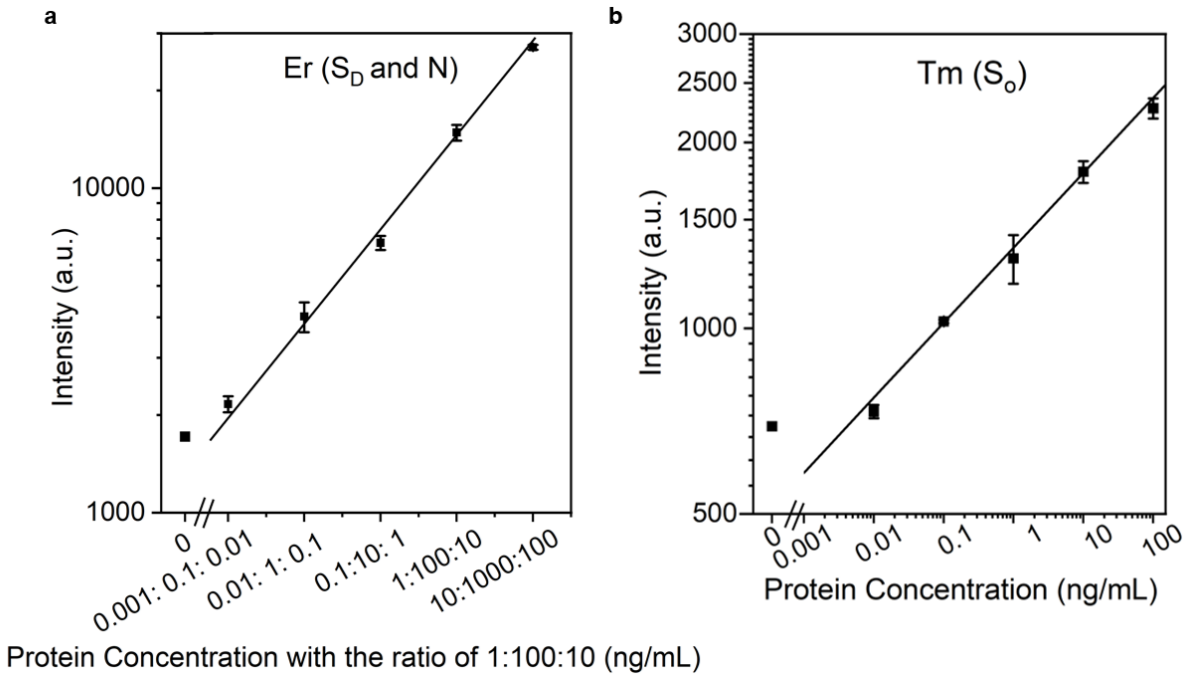

Figure 9. Simultaneous detection of three SARS-CoV-2 antigens using one MB-Ab conjugate and three types of UCNP-Ab conjugates. Calibration curves for Group 4, Group 5, and Group 6 correspond to the detection of three mixed antigen solution with the ratio of 1:100:10.

5.7 Conclusion

Multiplex detection plays a critical role in clinical diagnostics and pathogen surveillance, as it enables the simultaneous identification of multiple biomarkers or antigens within a single assay, thereby improving diagnostic efficiency, reducing sample consumption, and shortening turnaround time. Motivated by these advantages, we verified the multiplexed platform capable of detecting three SARS-CoV-2-related antigens using distinct MB-Abs and UCNP-Abs conjugates pairs.

Specificity tests demonstrated that each of the three antibody pairs exhibited high specificity toward their corresponding targets, with LODs reaching the hundreds of femtograms per milliliter (fg/mL) range. Nevertheless, the N protein showed a slightly elevated background signal compared to the two S proteins, which may be due to the use of smaller magnetic beads for its capture.

In cross-reactivity evaluations, Tm-doped UCNPs enabled clear and reliable detection of the N protein without interference. However, as both S_o and S_D antigens were

labeled with Er-doped UCNPs, their emission peaks overlapped at 650 nm, preventing discrimination between the two S proteins regardless of their concentration ratio. These findings highlight both the potential and the current limitations of our multiplexed detection strategy and underscore the need for further optimization of fluorophore selection and spectral separation to enable fully resolved, multi-analyte quantification.

5.8 Perspective

Through literature review, we found that material synthesis and innovation constitute a crucial aspect of multiplexed biosensing development. In current configurations, spectral overlap between UCNPs, especially those doped with the same lanthanide ions, has become a major limiting factor in simultaneous multi-analyte quantification. To address this, future iterations of the Beads-on-a-Tip platform will focus on the synthesis and integration of UCNPs with distinct and non-overlapping emission profiles. By engineering nanoparticles doped with alternative lanthanide ion combinations, such as other doping in different host matrices, which it is possible to achieve sharper and more spectrally separated emission peaks. This would enable more accurate signal deconvolution and facilitate the expansion of the multiplexing capability from two or three targets to four or more, without sacrificing specificity or sensitivity. Furthermore, with improved spectral separation, it would be feasible to use a single bead size for all targets, thereby simplifying assay design, enhancing consistency, and reducing variability introduced by heterogeneous bead populations.

An alternative strategy that does not require changes to the nanoparticle materials involves the integration of microfluidic channel design to physically separate bead populations. By engineering flow paths with tunable hydrodynamic or magnetic forces, it is possible to direct different sizes of MBs into distinct channels. This approach enables differential handling or signal readout of MB-antibody complexes, thereby resolving detection outputs even when spectral overlap exists. Such spatial separation complements the multiplexed detection strategy and provides a flexible solution for improving specificity and minimizing crosstalk without the need for synthesizing new UCNP materials.

Beyond advances in material design and assay architecture, future development of the Beads-on-a-Tip platform should focus more on applications using real and

clinically relevant samples. While the current work demonstrates sensitive and multiplexed detection under controlled laboratory conditions, practical applications will require robust performance in complex biological matrices such as whole blood, serum, saliva, and food samples. These matrices introduce additional challenges, including nonspecific adsorption, matrix-induced signal attenuation, and sample-to-sample variability, which may impact assay accuracy and reproducibility.

To address these challenges, future studies could incorporate optimized sample pretreatment strategies, such as dilution, filtration, or on-bead washing steps, to mitigate matrix effects while preserving assay simplicity. In addition, systematic evaluation of assay performance using real samples from clinical or industrial sources will be essential to assess robustness, diagnostic relevance, and regulatory feasibility. Demonstrating reliable multiplexed detection in real-world samples will be a critical step toward translating the Beads-on-a-Tip platform from a proof-of-concept system into a practical point-of-care diagnostic tool.

Reference

(1) Blennow, K.; Vanmechelen, E.; Hampel, H. CSF total tau, Aβ42 and phosphorylated tau protein as biomarkers for Alzheimer's disease. *Molecular Neurobiology* 2001, *24* (1), 87–97. DOI: 10.1385/MN:24:1-3:087.

(2) Paterson, R. W.; Slattery, C. F.; Poole, T.; Nicholas, J. M.; Magdalinou, N. K.; Toombs, J.; Chapman, M. D.; Lunn, M. P.; Heslegrave, A. J.; Foiani, M. S.; et al. Cerebrospinal fluid in the differential diagnosis of Alzheimer's disease: clinical utility of an extended panel of biomarkers in a specialist cognitive clinic. *Alzheimer's Research & Therapy* 2018, *10* (1), 32. DOI: 10.1186/s13195-018-0361-3.

(3) Ding, H.; Zhang, W.; Wang, S.-a.; Li, C.; Li, W.; Liu, J.; Yu, F.; Tao, Y.; Cheng, S.; Xie, H.; et al. A semi-quantitative upconversion nanoparticle-based immunochromatographic assay for SARS-CoV-2 antigen detection. *Frontiers in Microbiology* 2023, *Volume 14 - 2023*, Original Research. DOI: 10.3389/fmicb.2023.1289682.

(4) Li, L.; Song, M.; Lao, X.; Pang, S.-Y.; Liu, Y.; Wong, M.-C.; Ma, Y.; Yang, M.; Hao, J. Rapid and ultrasensitive detection of SARS-CoV-2 spike protein based on upconversion luminescence biosensor for COVID-19 point-of-care diagnostics. *Materials & Design* 2022, *223*, 111263. DOI: https://doi.org/10.1016/j.matdes.2022.111263.

(5) Mittal, A.; Khattri, A.; Verma, V. Structural and antigenic variations in the spike protein of emerging SARS-CoV-2 variants. *PLoS Pathogens* 2022, *18* (2), e1010260.

(6) Ahmad, R.; Ahsan, H. Multiplex Technology for Biomarker Immunoassays. In *Innate Immunity in Health and Disease*, Saxena, S. K., Prakash, H. Eds.; IntechOpen, 2020.

(7) Rissin, D. M.; Kan, C. W.; Campbell, T. G.; Howes, S. C.; Fournier, D. R.; Song, L.; Piech, T.; Patel, P. P.; Chang, L.; Rivnak, A. J.; et al. Single-molecule enzyme-linked immunosorbent assay detects serum proteins at subfemtomolar concentrations. *Nat Biotechnol* 2010, *28* (6), 595–599. DOI: 10.1038/nbt.1641 From NLM.

(8) Byrum, J. R.; Waltari, E.; Janson, O.; Guo, S.-M.; Folkesson, J.; Chhun, B. B.; Vinden, J.; Ivanov, I. E.; Forst, M. L.; Li, H.; et al. MultiSero: An Open-Source Multiplex-ELISA Platform for Measuring Antibody Responses to Infection. *Pathogens* 2023, *12* (5), 671.

(9) Klostranec, J. M.; Xiang, Q.; Farcas, G. A.; Lee, J. A.; Rhee, A.; Lafferty, E. I.; Perrault, S. D.; Kain, K. C.; Chan, W. C. W. Convergence of Quantum Dot Barcodes with Microfluidics and Signal Processing for Multiplexed High-Throughput Infectious Disease Diagnostics. *Nano Letters* 2007, *7* (9), 2812–2818. DOI: 10.1021/nl071415m.

(10) Wu, C.; Garden, P. M.; Walt, D. R. Ultrasensitive Detection of Attomolar Protein Concentrations by Dropcast Single Molecule Assays. *J Am Chem Soc* 2020, *142* (28), 12314–12323. DOI: 10.1021/jacs.0c04331 From NLM.

(11) Gong, F.; Tan, Z.; Shan, X.; Yang, Y.; Tian, S.; Zhou, F.; Ji, X.; He, Z. A Facile Strategy for Multiplex Protein Detection by a Fluorescent Microsphere-Based Digital Immunoassay. *Analytical Chemistry* 2024, *96* (8), 3517–3524. DOI: 10.1021/acs.analchem.3c05336.

(12) Taranova, N. A.; Berlina, A. N.; Zherdev, A. V.; Dzantiev, B. B. 'Traffic light' immunochromatographic test based on multicolor quantum dots for the simultaneous detection of several antibiotics in milk. *Biosensors and Bioelectronics* 2015, *63*, 255–261. DOI: https://doi.org/10.1016/j.bios.2014.07.049.

(13) Anfossi, L.; Di Nardo, F.; Cavalera, S.; Giovannoli, C.; Baggiani, C. Multiplex Lateral Flow Immunoassay: An Overview of Strategies towards High-throughput Point-of-Need Testing. *Biosensors* 2019, *9* (1), 2.

(14) Zhao, Y.; Wang, H.; Zhang, P.; Sun, C.; Wang, X.; Wang, X.; Yang, R.; Wang, C.; Zhou, L. Rapid multiplex detection of 10 foodborne pathogens with an up-converting phosphor technology-based 10-channel lateral flow assay. *Sci Rep* 2016, *6*, 21342. DOI: 10.1038/srep21342 From NLM.

Chapter 6 Conclusion and Perspectives

6.1 Conclusion

This thesis establishes and validates two UCNP enabled POCT platforms that address key sensitivity and robustness limitations of conventional immunoassays. By integrating materials design, surface chemistry optimization, and assay-format engineering, this work demonstrates how UCNP-based signal amplification can be translated into practical analytical systems for both food quality control and infectious disease diagnostics.

A UCNP-based LFIA was first developed for the selective detection of A1 β-casein in milk and infant formula. This platform demonstrates that UCNP reporters, when functionalized with the custom-synthesized polymer developed in this work, can be effectively applied to milk samples without pretreatment. In this research, the polymer coating plays a critical role in minimizing non-specific binding, thereby enabling quantitative discrimination of low-level A1 contamination within an A2 protein background. The achieved sensitivity and specificity confirm the feasibility of UCNP-LFIA as a practical tool for routine dairy quality monitoring.

To overcome the intrinsic sensitivity limitations imposed by capillary-driven LFIA formats, a magnetic bead-based Beads-on-a-Tip sandwich immunoassay was subsequently introduced. By integrating target capture, washing, and signal generation into a single assay workflow, this platform enables active analyte enrichment while effectively reducing background signals. As a result, femtogram-level detection of SARS-CoV-2 antigens was achieved, representing a substantial improvement over conventional membrane-based assay. Importantly, this strategy preserves operational simplicity while offering enhanced analytical performance.

Furthermore, the Beads-on-a-Tip platform was extended to multiplex detection of SARS-CoV-2 variants, demonstrating its adaptability to multi-target diagnostics. While spectral overlap between lanthanide-doped UCNPs currently constrains full discrimination of closely related targets, the results highlight the platform’s strong potential for multiplexed point-of-care applications.

Overall, this thesis demonstrates that combining highly doped UCNPs with rational assay design enables substantial gains in sensitivity, specificity, and versatility, providing a robust foundation for next-generation POCT technologies.

6.2 Perspectives

The UCNP-based POCT platforms developed in this thesis show strong potential for translation into real-world diagnostic applications. Their successful implementation in milk and infant formula demonstrates robustness in complex matrices, highlighting suitability for decentralized testing scenarios where minimal sample preparation is required. For A1 β-casein detection, future work should focus on improving antibody specificity and assay robustness in highly processed dairy products. The current reliance on polyclonal antibodies introduces limitations in reproducibility and background suppression. The development of well-matched monoclonal antibody pairs and dual-analyte strategies for simultaneous A1/A2 detection would enable more accurate relative quantification in real samples. In addition, mild pretreatment strategies targeting β-casein micelle dissociation could further improve assay accuracy without compromising field usability.

In the context of infectious disease diagnostics, the Beads-on-a-Tip platform offers remarkable advantages for analyzing low-abundance biomarkers in complex biological samples. Its compatibility with magnetic enrichment and active washing makes it particularly suitable for saliva, nasal swabs, and other minimally processed clinical specimens. Future efforts may focus on validating performance across diverse real sample types and integrating simplified fluid-handling steps to further enhance usability in point-of-care settings.

For multiplex detection, overcoming spectral overlap remains a key challenge. This may be addressed through the development of UCNPs with well-separated emission profiles, as well as through spatial or temporal signal separation strategies. Such advances would expand the applicability of the platform to broader panels of biomarkers relevant to emerging infectious diseases and precision diagnostics.

With continued optimization at both the material and assay-design levels, the UCNP-based platforms presented in this thesis have the potential to contribute meaningfully

to sensitive, reliable, and scalable diagnostic solutions across food safety and clinical testing domains.